A TOUGHENED COMPOSITE FOR IMPROVING THE ANCHORING OF COMPOSITE TENSILE ARMORS OF FLEXIBLE RISERS

Rafael Pereira Mattedi

Thesis presented to *Programa de Pós-graduação em Engenharia Metalúrgica e de Materiais*, COPPE, from *Universidade Federal do Rio de Janeiro*, and to *Ecole Centrale Supélec*, from *Université Paris Saclay*, as part requirements for obtaining the title of Doctor of Science in Materials Engineering and Doctor in Materials Science.

Directors: Prof. Fernando Luiz Bastian PhD
Prof. Marysilvia F., da Costa DSc
Prof. JinBo Bai Dr

Rio de Janeiro

Julho 2019

A TOUGHENED COMPOSITE FOR IMPROVING THE ANCHORING OF COMPOSITE TENSILE ARMORS OF FLEXIBLE RISERS

Rafael Pereira Mattedi

THESIS SUBMITTED TO TEACHING BODY OF *INSTITUTO ALBERTO LUIZ COIMBRA DE PÓS-GRADUAÇÃO E PESQUISA DE ENGENHARIA (COPPE)* FROM *UNIVERSIDADE FEDERAL DO RIO DE JANEIRO* AND TO *ECOLE CENTRALE SUPÉLEC FROM UNIVERSITÉ PARIS SACLAY* AS PART OF REQUIREMENTS FOR OBTAINING THE DEGREE IN DOCTOR OF SCIENCE IN MATERIALS ENGINEERING AND DOCTOR IN MATERIALS SCIENCE.

Approved by:

_____

Prof. Marysilvia Ferreira da Costa D.Sc.

_____

Prof. Jinbo Bai Ph.D.

_____

Prof. Delong He Ph.D.

_____

Prof. Lionel Pichon Ph.D.

_____

Prof. José Roberto D'Almeida D.Sc.

_____

Prof. Hector Kotic Ph.D.

RIO DE JANEIRO – BRAZIL

JULHO 2019

Mattedi, Rafael Pereira

A toughened composite for improving the anchoring of composite tensile armors of flexible risers / Rafael Pereira Mattedi. – Rio de Janeiro: UFRJ/COPPE, 2019.

XXII, 140 p.: il.; 29,7 cm.

Director(s): Fernando Luiz Bastian PhD

Marysilvia Ferreira da Costa DSc

Jinbo Bai PhD

Thesis (Doctor of Science) – UFRJ/ COPPE/ Programa de Engenharia Metalúrgica e de Materiais, 2018.

References: p. 123-131.

1. Nanocomposite. 2. Anchoring. 3. CFA. 4. Tensile armors. 5. Flexible risers. 6. Pull-out. I. Da Costa, Marysilvia Ferreira et al. II. Universidade Federal do Rio de Janeiro, COPPE, Programa de Engenharia Metalúrgica e de Materiais. III. A toughened composite for improving the anchoring of composite tensile armors of flexible risers.

Acknowledgements

This work would not be possible without the financial and professional support of *TechnipFMC*® and respective colleagues and leaders. I would like to particularly thank M. Anh-Tuan Do, M. Dominique Perreau-Saussine, M. Laurent Decoret, Ms Daniela Riva, M. Fernando Toste, M. Felipe Reis and Ms. Roberta Pires. Also, from legal department, thank you Ms Isabela Seraphico, Ms Melindy Mathews and Ms Chloé Blackwell.

I am grateful to prof. Dr. Jinbo Bai, my thesis director from *Ecole CentraleSupélec*, responsible for Nano materials laboratory at MASSMAT establishment. His knowledge, mentoring and support was crucial for reaching the conclusion of this work. Prof. Dr. Marysilvia Ferreira da Costa, my thesis director from *Universidade Federal do Rio de Janeiro* and head of *Programa de Engenharia Metalúrgica e de Materiais*, who adopted me in the end of the research and helped with a lot of patience to conclude the thesis and the *cotutelle* process between Universities. I am grateful to all administrative colleagues from both Universities of those that also worked hard for making this *cotutelle* become feasible. Furthermore, thank my friends from both Universities with whom I have had the pleasure to work during this project. And finally, I would especially like to thank prof. Dr. Fernando Luiz Bastian, first director of this thesis from *Universidade Federal do Rio de Janeiro*, who sadly passed away in August 2017. As my professor and mentor, he has taught me more than I could ever give him credit for here. He has shown me, by his example, how a good scientist and person must be.

I would like to thank my friends for accepting nothing less than excellence from me. Last but not the least, I would like to thank my family: my parents Derlino and Marilza Mattedi, brother Flavio Mattedi, sister in law Alessandra Marques and my wife Bruna Gama for supporting me spiritually throughout writing this thesis.

To my amazing, lovely and patient wife, Bruna Gama;

My parents, Derlino Mattedi and & Marilza Mattedi;

My brother, Flavio Mattedi, my sister in law Alessandra Matos and my beautiful niece and goddaughter, Alice Mattedi

And, especially to my deceased professor and director, Fernando Luiz Bastian PhD.

Abstract of the Thesis presented to COPPE/UFRJ and *UNIVERSITÉ PARIS SACLAY* as a partial fulfillment of the requirements for the degree of Doctor of Science in Materials Engineering and Doctor in Materials Science.

A TOUGHENED COMPOSITE FOR IMPROVING THE ANCHORING OF COMPOSITE TENSILE ARMORS OF FLEXIBLE RISERS

Rafael Pereira Mattedi

July/2019

Directors: Fernando Luiz Bastian PhD, Marysilvia Ferreira da Costa DSc, JinBo Bai Dr

Department: *Engenharia Metalúrgica e de Materiais*

The use of composite and nanocomposites is a growing trend in many industries such as aerospace, automotive and energy. For many applications, the adhesion between structures for efficiently transferring loads is a difficult problem to solve. In oil and gas segment, for instance, a common technique used for anchoring the tensile armors of flexible riser within the end fitting is through an embedded epoxy since it provides good mechanical and chemical resistance. Even though, cracks and defects can arise in the epoxy block during operations or mounting at epoxy curing step, and such cracks could affect the anchoring performance, in particular for carbon fiber composite armors (CFA). In this context, this work proposes the improvement of the epoxy for anchoring the CFA, with a focus on the mechanical and adhesion properties. An analytical model is developed for CFA anchoring mechanism and verified by numerical analysis to evaluate the sensitivity of the system to the epoxy characteristics. Thus, the increase of these properties is proposed by adding multi-walled Carbon Nanotubes (MWCNTs) and some experiments are carried out with neat and toughened epoxies to characterize the gain of mechanical and adhesive properties. Then, nanotubes morphology and the matrix homogeneity are expertized to correlate with mechanical results. The research confirmed an improvement of anchoring resistance by toughening the epoxy matrix with MWCNTs.

Résume de la thèse présentée à COPPE/UFRJ et UNIVERSITÉ PARIS SACLAY dans le cadre des exigences pour l'obtention d'un Doctorat en Ingénierie des Matériaux et un Doctorat en Sciences des Matériaux.

UN COMPOSITE RENFORCÉ POUR AMELIORER L'ANCRAGE DES ARMURES DE TRACTION EN COMPOSITE DES RISERS FLEXIBLES

Rafael Pereira Mattedi

Juillet 2019

Directeurs : Fernando L. Bastian PhD, Marysilvia F. da Costa DSc, JinBo Bai Dr
Programme : *Engenharia Metalúrgica e de Materiais*

L'utilisation de composites et nano composites est une tendance croissante dans des industries telles que l'aérospatiale, l'automobile et l'énergie. Pour de nombreuses applications, l'adhésion entre des structures pour bien transférer les efforts est un problème difficile à résoudre. Dans l'industrie pétrolière, par exemple, une technique utilisée pour ancrer les armures de traction d'une conduite flexible est à travers un époxy intégré car elle fournit une bonne résistance mécanique et chimique. Cependant, des fissures et des défauts peuvent apparaître dans le bloc époxy pendant les opérations ou le montage lors de l'étape de cuisson de l'époxy, et ces fissures pourraient affecter les performances d'ancrage, en particulier pour les armures composites en fibre de carbone (CFAs). Dans ce contexte, ce travail propose le renforcement de l'époxy pour l'ancrage du CFA, focalisé sur les propriétés mécaniques et d'adhérence. Un modèle analytique est développé pour le mécanisme d'ancrage du CFA et vérifié par analyse numérique pour évaluer la sensibilité du système aux caractéristiques de l'époxy. Ainsi, l'augmentation de ces propriétés est proposée par l'ajout de nanotubes de carbone multi-feuilles (MWCNTs) et des essaies sont réalisées avec le époxy pur et renforcés pour caractériser l'augmentation des propriétés mécaniques et adhésives. Ensuite, la morphologie des nanotubes et l'homogénéité de la matrice sont investiguées pour corréler avec des résultats mécaniques. La recherche a confirmé une amélioration de la résistance à l'ancrage en renforçant la matrice époxy avec des MWCNTs.

Resumo da Tese apresentada à COPPE/UFRJ e *UNIVERSITÉ PARIS SACLAY* como parte dos requisitos necessários para a obtenção do grau de Doutor em Engenharia de Materiais e Doutor em Ciências dos Materiais.

COMPOSITO PARA MELHORIA DA ANCORAGEM DAS ARMADURAS DE TRAÇÃO DE COMPOSITITO DE RISERS FLEXIVEIS

Rafael Pereira Mattedi

Julho/2019

Orientadores: Fernando L. Bastian PhD, Marysilvia F. da Costa DSc, JinBo Bai Dr
Programa: Engenharia Metalúrgica e de Materiais

O uso de compósitos e nano compósitos é uma tendência crescente em muitas indústrias, como aeroespacial, automotivo e energia. Para muitas aplicações, a adesão entre estruturas para transferência eficiente dos esforços é um problema de difícil solução. No segmento de óleo e gás, por exemplo, uma técnica comum utilizada para ancorar as armaduras de tração do tubo flexível dentro do conector é através de um epóxi embebido, pois proporciona boa resistência mecânica e química. No entanto, trincas e defeitos podem surgir no bloco de epóxi durante as operações ou montagem, na etapa de cura do epóxi, e tais defeitos podem afetar a performance de ancoragem, em particular para armaduras de compósito de fibra de carbono (CFA). Neste contexto, este trabalho propõe a melhoria do epóxi para ancorar o CFA, com foco nas propriedades mecânicas e adesivas. Um modelo analítico é desenvolvido para o mecanismo de ancoragem do CFA e verificado por análise numérica para avaliar a sensibilidade do sistema às características do epóxi. Assim, o aumento dessas propriedades é proposto pela adição de nanotubos de carbono de múltiplas paredes (MWCNTs) e alguns experimentos são realizados com os epóxis puro e modificado para caracterizar o ganho de propriedades mecânicas e adesivas. Em seguida, a morfologia dos nanotubos e a homogeneidade da matriz são investigadas para correlacionar com os resultados mecânicos. A pesquisa confirmou uma melhoria da resistência à ancoragem ao tenacificar a matriz de epóxi com MWCNTs.

TABLE OF CONTENTS

LIST OF FIGURES

LIST OF TABLES

LIST OF SIMBOLS

AFRL	Air Force Research Laboratory
ASTM	American Society for Testing Materials
CAD	Carbon Arc Discharge
CFA	Carbon Fiber Armor
CFC	Carbon Fiber Composite
CMOD	Crack-mouth Opening Displacement
CNT	Carbon Nanotube
CTBN	Carboxyl-terminated Butadiene Acrylonitrile copolymer
CTOD	Crack Tip Opening Displacement
CVD	Chemical Vapor Deposition
CZM	Cohesive Zone Model
DCB	Double cantilever beam specimen
DWCNT	Double-walled Carbon Nanotube
EDX	Energy-dispersive X-ray spectroscopy
FEM	Finite Element Model
FPSO	Floating Production Storage and Offloading
FRP	Fiber Reinforced Polymer
GNP	Graphene Nano Particle
HAADF	High angle annular dark field
HIC	Hydrogen Induced Cracking

HiPCO	High Pressure Carbon Monoxide
HST	High strength tape
HTPU	Hydroxyl-terminated Polyurethane
IFP	French Institute of Petroleum
LEFM	Linear elastic fracture mechanics
MSSMAT	*Mécanique des Sols, Structures et Matériaux*
MWCNT	Multi-walled Carbon Nanotube
ODE	Ordinary differential equation
PEEK	Polyether-ether-ketone
PEKK	Polyether-ketone-ketone
PI	Polyimide
PLV	Pulsed Laser Vaporization
PPS	Polyphenylene Sulfide
PTFE	Poly-tetrafluoroethylene
PU	Polyurethane
QPE	Quarter Point Element
RVE	Representative volume element
SCC	Stress Corrosion Crack
SEM	Scanning Electron Microscopy
SCC	Stress Corrosion Cracking
SHM	Structure Health Monitoring
SPU	Stationary production unit

SSCC	Sulfide Stress Corrosion Cracking
SWCNT	Single-walled Carbon Nanotube
TEM	Transmission Electron Microscopy
Tg	Glass Transition Temperature
UDW	Ultra-Deep Water
UTS	Ultimate tensile stress
VCCT	Virtual Crack Closure Technique
VCM	Vertical Connection Modulus
XPS	X-ray photoelectron spectroscopy
YS	Yield strength

Chapter 1 – Introduction

Faced with the technological advances of materials, the use of composites has become more frequent in several segments of industry. According to MAZUMDAR [1], today the aerospace and automotive are the sectors that most contribute to the application of this material. Figure 1 shows some statistical numbers regarding the trend of consumption of composites up to 2020 in different sectors in the United States.

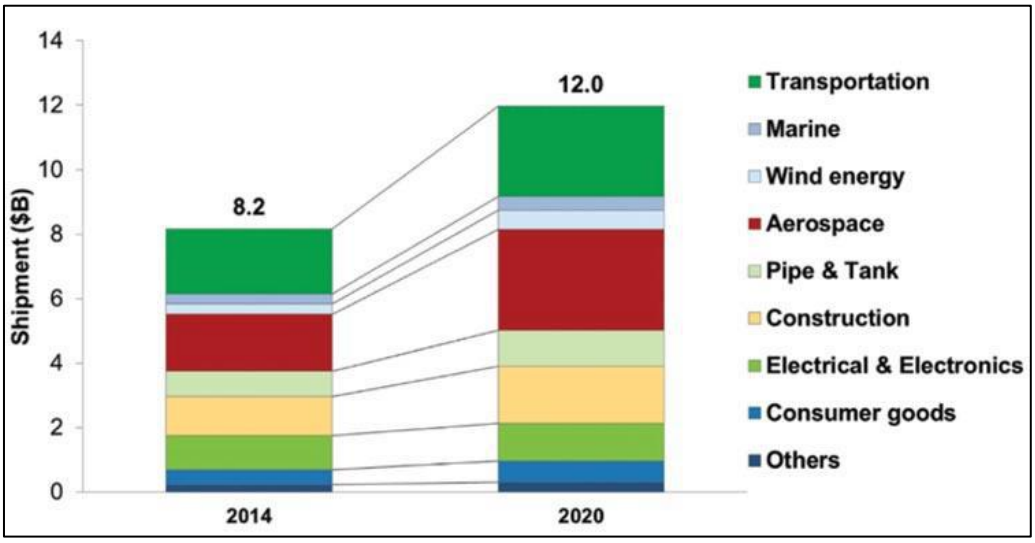

Figure 1 – The increasing use of composites (from MAZUMDAR [1]).

By analyzing the shipment of composites in the graph, the growth in the market is evident. This same information can be confirmed through Figure 2, which shows the relative importance of metallic, polymeric, composite and ceramic materials over the years, also up to 2020.

According to this figure, the importance of composite materials has increased since the post-World War II period, begun in 1945. These materials, mainly with reinforcements of carbon, glass and aramid fibers, have the characteristic of high specific mechanical resistance, that is high mechanical strength and low density. These are qualities sought by the sectors that develop products and components that are submitted to static and dynamic loads directly proportional to their own weights.

In the oil and gas subsea industry, the use of composites has also gained strength due to the increased depth of offshore fields [2]. These are commonly called Ultra-Deep Water (UDW) fields.

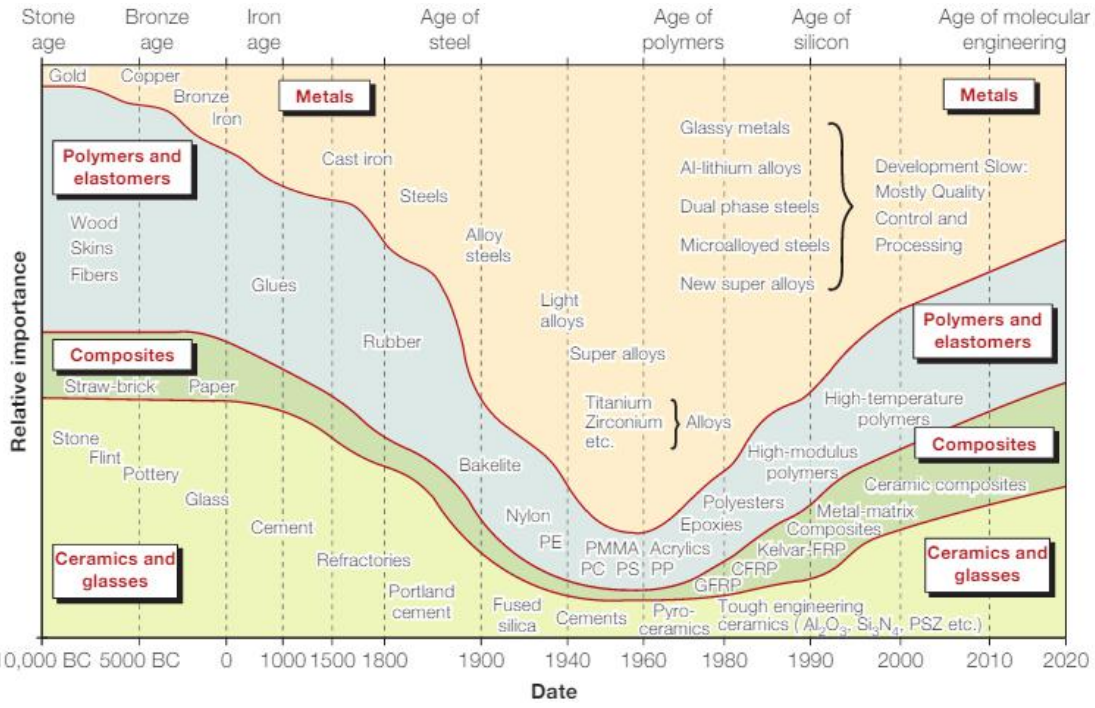

Figure 2 – Relative importance of metals, polymers, composites and ceramics over the years. (from ASHBY [3]).

The flexible risers [4] are pipelines that connect offshore platforms to subsea wells for oil, gas or water transfer as shown in Figure 3. Their tensile armors are usually made of carbon steel, which generates excessive weight and therefore high tensile loads. Thus, the use of composites is attractive because it tends to minimize this issue. The composite that has been studied by DO *et al.* [5, 6] for these armors is based on carbon fiber, so called Carbon Fiber Armor (CFA). The main advantage of this type of armor is precisely the specific mechanical strength when compared to carbon steel wires.

However, CFA solution for risers brings some challenges to the anchoring of armors at their extremities within end fittings (EFs). Normally, the CFA cannot be shaped or plastically deformed to achieve a specific geometry to be anchored in an epoxy resin, for instance, which is usually the case with steel wires through hooks and ripples [7]. In this case, the CFA anchoring must be considered through pure adhesion with the epoxy, and this system must be meticulously studied for a good understanding of its failure modes. With the CFA adhered to an epoxy, it could then be considered that a new composite is formed, where the CFA acts as a reinforcement and the epoxy as a matrix.

In this context, the present work proposes a composite material to optimize CFA anchoring. In the other hand, the CFA is considered a constant parameter throughout the study, with its pre-established mechanical properties. The matrix, on the other hand,

has its mechanical properties and adhesion to the CFA studied, aiming the optimization of the final composite.

Thus, the proposed composite is formed by CFAs as main reinforcement, which have orthotropic properties, and by an epoxy resin matrix with isotropic properties. The matrix is toughened by fillers, which could be polymer particles, short carbon or aramid fibers, or carbon nanotubes.

An analytical method is developed for the anchoring system, based on composite and fracture mechanics, and validated by numerical model using finite element analysis.

Small-scale mechanical tests and some micrographic analysis are performed with the neat and toughened epoxies, and with the CFA-Epoxy system. Therefore, its mechanical properties such as strength, modulus, elongation, toughness and adhesion to the CFA are evaluated.

Finally, a sensitivity study is carried out using the analytical pull-out failure model with the results of the tests to confirm the toughening option and its respective concentration for an improved composite for anchoring the CFAs of the flexible risers.

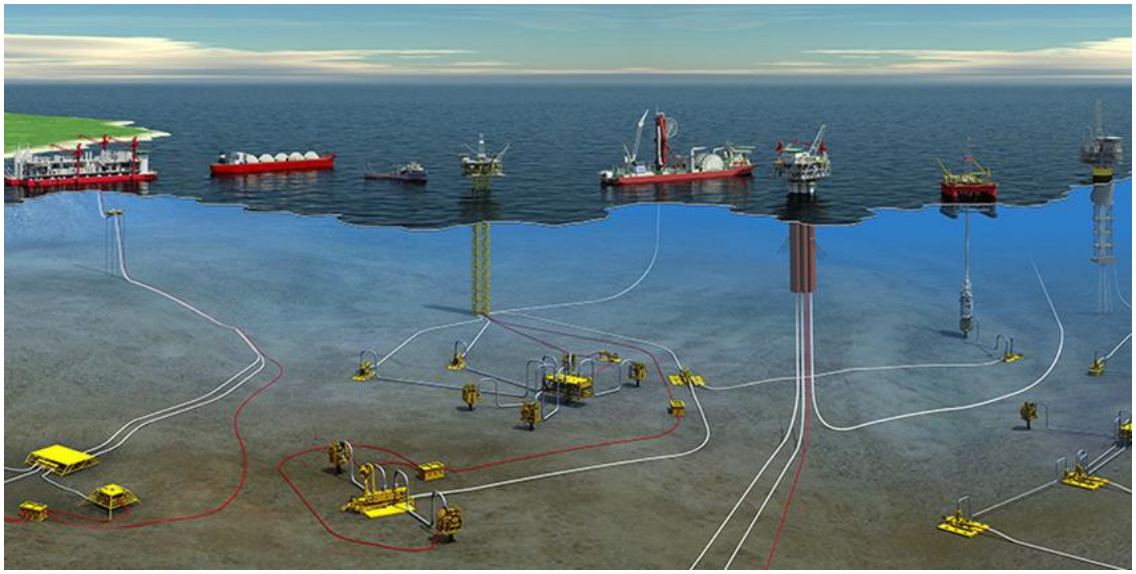

Figure 3 – Subsea architecture of flexible and rigid risers [8].

Chapter 2 – Literature review

2.1. FLEXIBLE RISERS

The growing seek for energy has greatly boosted oil and gas exploration, and many of this fossil fuel wells are located deep in the oceans. According to CAMPELLO [9], in offshore production systems, these fluids are transported between their fields and Stationary Production Unit (SPU), or offshore platforms, through pipelines, which are so called flowlines and risers.

The flowlines are the horizontal pipe sections installed in the seabed and are, basically, subjected to static loads and connect the Vertical Connection Module (VCM) to the riser or other VCM. The risers are vertical or slightly sloped and connect the seabed to the SPU. They are normally subjected to static and dynamic loads [9].

These pipes can be rigid, so called Steel Catenary Risers (SCR) [10], or flexibles [4], also known as unbounded flexible pipes since they have layers not bonded to each other.

Figure 4 presents a SPU type Floating Production Storage and Offloading (FPSO) with risers and flowlines installed up to the connection modules on the seabed. In the image, the risers are installed in Lazy Wave catenary, which predicts buoyancy segments fixed to the outer diameter of the riser, generally in the intermediate section, to reduce the axial loads at the top.

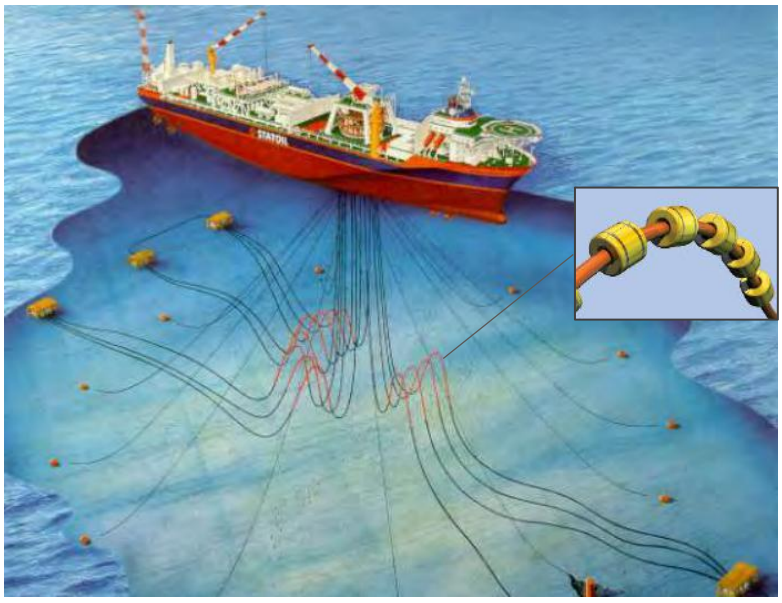

Figure 4 – Illustration of FPSO with risers installed up to seabed [11].

According to LI *et al*. [12], for oil, gas or even water transportation, the flexible pipes are widely used in deep water applications because of their low flexural stiffness and good axial stiffness and strength. Moreover, according to FRASER [13], they can usually offer advantages in the total final cost compared to traditional SCR, because this one normally has welded segments that have to be introduced onboard during installation, which is time consuming and therefore an expensive operation.

The flexible pipes are composed of several layers of different metallic, polymeric or composite materials, and they have their respective functions. Figure 5 presents a flexible riser with typical layers.

Figure 5 – Typical layers of flexible riser.

By analyzing the layers from the bore, the Carcass has the main function of resisting collapse against hydrostatic pressure. The pressure sheath is responsible for the tightness of the transported fluid and, consequently, for the internal pressure. The pressure armor is used as mechanical support of the pressure sheath when subjected to internal pressure. It also helps in collapse resistance. Then, the anti-wear tapes are placed to avoid friction between the metallic layers. Following the sequence, the tensile armors have the function of withstanding the axial loads coming from the own weight of the flexible and the movements of the SPU due to the sea currents. Externally to the tensile armors, the High Strength Tapes, or HSTs, are responsible for keeping them organized and avoid radial and lateral buckling due to the reverse end cap effect. Finally, the external sheath is used to protect the inner layers against eventual impacts during transportation, installation and operation, and against corrosion of the metallic layers. An extra protection sheath can be added above the external sheath.

The space between the pressure sheath and the external sheath is called annulus. Currently, this region is deeply studied due to gases such as CH_4, CO_2 and H_2S that diffuse from the bore through the pressure sheath and remain confined between the metallic layers. These gases, mixed with condensed water and at high temperatures and

pressure of the transported oil, generate a highly corrosive fluid, which is often responsible for the failure of the flexible pipe through HIC, SSCC, SCC, generalized corrosion and fatigue-corrosion of metallic layers, for instance.

The main standards that specifies and give recommended practices for designing, qualification, manufacturing and supplying flexible risers are API 17J – Specification for Unbounded Flexible Pipe [4], API 17B – Recommended Practice for Unbounded Flexible Pipe [14] and API 17L1 – Specification for Flexible Pipe Ancillary Equipment [15]. The last one is addressed to flexible's ancillary equipment.

2.1.1. Historical overview of the Risers

The first application of pipelines in the oceans came in World War II, in 1944, with PLUTO's Operation (Pipe-lines under the ocean) [16]. On that episode, the allied military in partnership with oil companies built secret pipelines linking the United Kingdom to Normandy in France for oil supply to support the invasion of the allies on the European continent. They needed a very large amount of fuel and, therefore the pipelines were necessary to reduce the dependency on oil tanks, which could take long lime to arrive due to poor weather conditions. These pipelines would be the so-called risers and flowlines.

According to [17], the commercial flexible pipes came later that time, in the 70's with *Coflexip*®, which merged with the *Technip*® group in 2003 (today *TechnipFMC*® group), through the development of a patent from the French Institute of Petroleum (IFP).

This flexible pipe was designed at first for drilling systems. Then, with the advancement of the technology, the flexibles could withstand high pressures, therefore they started being developed for exploration of oil and gas, mainly in the oceans. At that time, they passed for denomination risers and flowlines.

There are currently more than ten thousand kilometers of risers installed and operating in the oceans at depths up to two thousand five hundred meters deep, and with internal diameters between two and twenty inches [18]. There is also a tendency of the depths to reach up to three thousand meters. These are called Ultra Deep Water Fields (UDW).

2.1.2. Flexible risers with composite tensile armors

Reaching the UDW fields, the use of composite layers in flexible risers has been widely discussed in subsea oil and gas industry.

At these depths, the risers are subjected to high static and dynamic axial loads originated by the movement of the SPUs due to the sea currents and their own weight. LAMBERT *et al.* [2] ratify that the cyclic stresses in the armors are often combined with corrosion due to the presence of CO_2 and H_2S in the annulus. This fluid condition is characterized as Sour Service. Therefore, depending on the loading levels and severity of the corrosive fluid, a flexible riser using carbon steel armors could be a challenging solution.

One of the materials that has been studied by DO *et al.* [5] to make these cases feasible is the composite based on carbon fiber, or Carbon Fiber Composite (CFC) due to the high specific mechanical strength (ratio between mechanical strength and density). In this case, for tensile armors, it is called Carbon Fiber Armor (CFA). The use of this material as well as other composites for subsea applications is normalized by the DNVGL-OS-C501 - Composite Components [19].

Figure 6 – Flexible pipe with CFA wires, current and future water depth capacity by internal diameter (from DO *et al.* [5]).

Basically, this solution predicts a riser with typical layers, but the tensile armor layers, usually carbon steel, are replaced by CFAs. Figure 6 on the left presents a riser with two pairs of CFA layers for UDW application. The main diameters used in the market are presented on the right side, as well as their respective water depth capacities of current risers with steel armors and future risers, with CFAs solution.

The graph from Figure 7 shows the difference between the specific mechanical strengths of the carbon steels commonly used for armors and CFC. By analyzing the values, it is noticed that the CFC can achieve specific resistance up to fourteen times greater.

Obviously, this resistance depends directly on the materials selected for the composite design. But this subject will be better addressed in section 2.2.

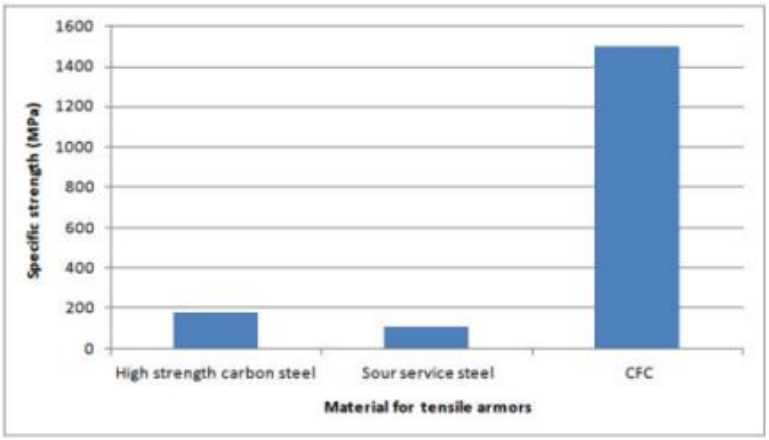

Figure 7 – Specific resistance comparison between typical carbon-steel and CFC (from DO *et al.* [5]).

It is important noting, though, the feasibility of manufacturing, handling and installation of the flexible riser with CFAs, as well as the final cost, are further factors that must be meticulously evaluated for the solution to be marketable.

Due to the lower stiffness and strength in directions different of fiber's, the spiraling of the CFAs around the flexible pipe during manufacturing and the handling during assembling the end fittings involve some difficulties and limitations. The torsion and bending moment generated in these steps are studied by SALIMI *et al.* [20].

Furthermore, according to KULSHRESHTHA and VASILE [21], the cost of a flexible riser with CFA is expected to be higher than with carbon steel armors. However, it is important to highlight that, in cases of high depths and high axial loads, if steel armors are considered, it might be necessary to use buoyancy systems in the intermediary risers to reduce these loads at the top (Lazy Wave configuration from Figure 4). In this case, the final cost of the complete solution with steel armors and buoys can be challenged by the final cost of a solution with CFA armors in Free Hanging configuration. Therefore, proposing flexible risers with CFAs can be considered recommended for applications where axial loading and fluid conditions condition are more severe.

2.1.3. Anchoring of tensile armors

For transferring fluids between subsea fields and SPUs, it normally requires more than one section of risers and flowlines because of the water depth and therefore, their

extremities must be interconnected. A typical complete pipeline has, for instance, a top, intermediate and bottom risers, and a flowline. Then, for connection between them to VCM and SPUs, it is used the called End-fittings (EFs).

This accessory has as main function terminating and anchoring all layers of the flexible pipe, that is, to ensure the leakproof-ness of the pressure, external and protective sheaths, and to anchor the pressure and tensile armors. Thus, the loads are well supported and transferred to another EF, VCM or platform.

According to BUENO [7] and CAMPELLO [9], EFs usually use an epoxy resin for anchoring the tensile armors. Therefore, the resin is responsible for transferring the axial loads from tensile armors to the EF structure. Figure 8 presents a cross section of an EF from patent US20120211975 [22]. It shows an anchoring type of tensile armors, which are shaped in a predefined geometry, and fixed at their extremities to the EF body. Then, all available anchoring chamber is embedded by the epoxy resin.

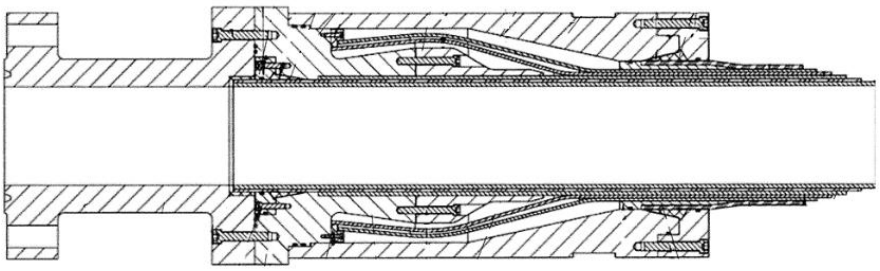

Figure 8 – Typical anchoring of tensile armors of flexible riser (*Patent* US20120211975 [22]).

Two other examples of anchoring are shown in Figure 9 and Figure 10. In the first, BUON and BERTON's patent [23], the armors are also shaped to follow a specific geometry in the EF, and hooks are made at the extremities (item 21 of Figure 9) to ensure the anchor in the epoxy. BELCHER [24] considers shaping ripples at the extremities as another option for the same function as BUON and BERTON's hooks.

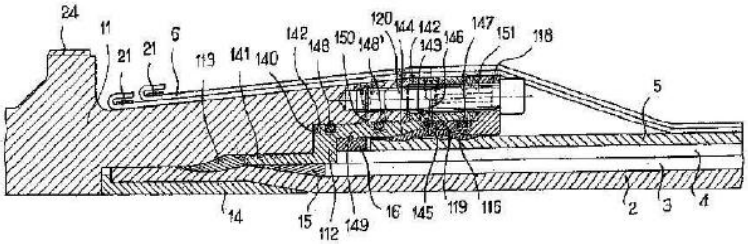

Figure 9 – Simplified section of End fitting (from BUON e BERTON [23]).

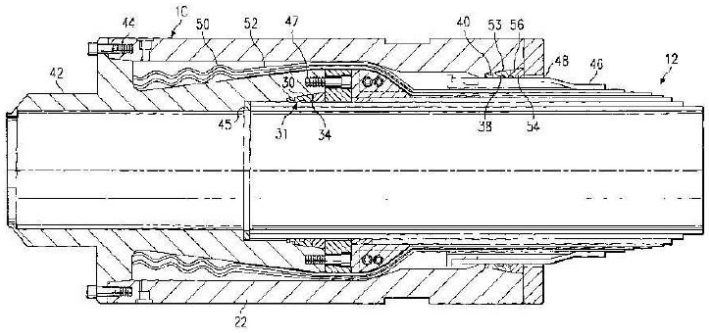

Figure 10 – End fitting with rippled armor extremities (de BELCHER [24]).

The CFA solution for risers brings some challenges for the anchoring inside the EFs. For example, the CFA extremities cannot be shaped as presented in the previous figures with carbon steel armors. In this case, by keep using the epoxy, the anchoring of the CFAs should be carried out by the pure adhesion with the resin. This concept is the basis of this work, which is then considered that a new composite of CFA and epoxy is formed, where the CFA acts as reinforcement and the epoxy as matrix. A more detailed review of composite materials is presented in the following section.

2.2. COMPOSITE MATERIALS

Composite material, according to GIBSON [25] and JONES [26], is basically the combination of two or more materials for reaching another with specific properties. Generally, it contains one or more material acting as reinforcement and other as matrix.

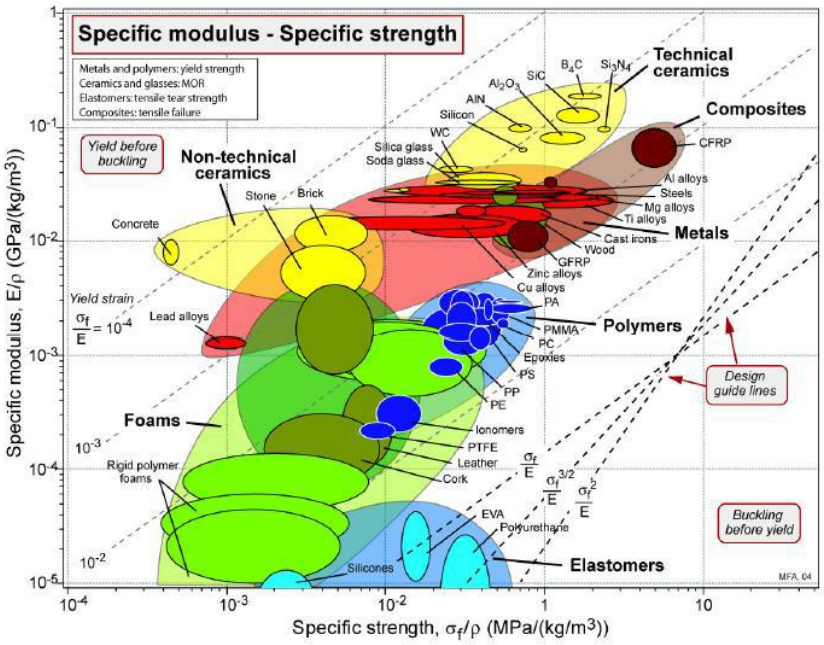

Figure 11 – Materials selection chart of specific strength versus specific modulus [3].

The advantage of composite materials is that, if properly developed, they can combine the best characteristics of their constituents or even create new capabilities [26]. Some properties that could be improved are, for example, mechanical and fatigue strength, stiffness, toughness, weight, thermal or electrical insulation or conductivity, and corrosion resistance. Figure 11 shows the position of some composites in a plot of specific strength versus specific modulus.

High performance composites are generally manmade, but other compounds can also be found directly in nature. Wood, for example, consists of the combination of cellulose fibers impregnated by a lignin matrix, whereas mammalian bones are made from collagen fibrils in a protein-calcium phosphate matrix [25].

Composites are recognized since ten thousand years B.C., as already shown in Figure 2 from ASHBY [3], Chapter 1. However, it is unknown when the human being began to work with composite materials. According to GIBSON, the book of Old Testament Exodus from the Holy Bible records one of the first composites of fibers that were probably made by man, the clay-reinforced straw, used by the Israelites at the time. Years later, composite structures such as reinforced concrete, polymers reinforced with different fibers, among others, were developed by humanity.

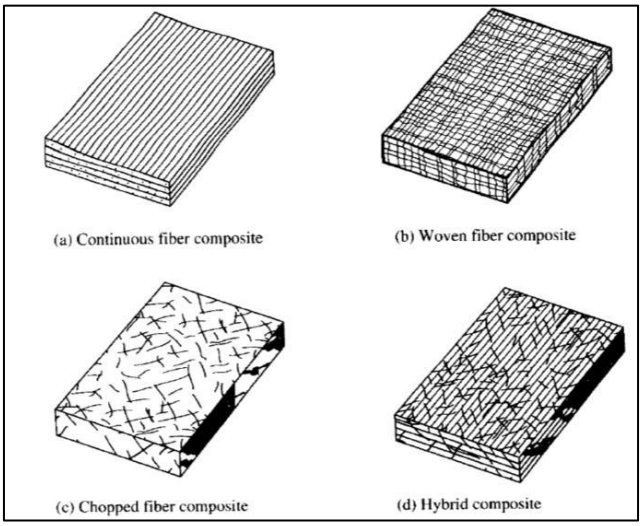

Figure 12 – Arrangement types of composite reinforcements by fibers: a) Continuous or long fibers, b) Woven, c) Randomly oriented short fibers, d) Hybrid (de GIBSON [25]).

Composites can be classified in four main types [26]:

- Fibrous: consist of fibers impregnated by a matrix;
- Laminates: set of several layers of different materials bonded to each other;

- Particulate: Similar to fibrous composite, but with particles instead of fibers;
- Hybrids: Combination of two or all the above types.

Figure 12 presents the four different types of fiber-based composites.

The properties of a composite material depend not only on the initial properties of its constituents, but also on the volume fraction between them, the geometric arrangement of the reinforcement and, finally, the interface adhesion between them.

2.2.1. Composite reinforcements and their properties

From previous section, the composites can have several types of reinforcements like: Long or short fibers, particles and blades.

The fibers have the characteristic of offering high stiffness and mechanical resistance in the direction of its main axis due to the alignment of its crystals [26]. As its diameter usually approximates the size of a crystal, the aspect ratio is very high for long fibers. However, because of their low mechanical properties in the other directions, a composite design usually combines fibers oriented in different direction embedded in a matrix for application in engineering.

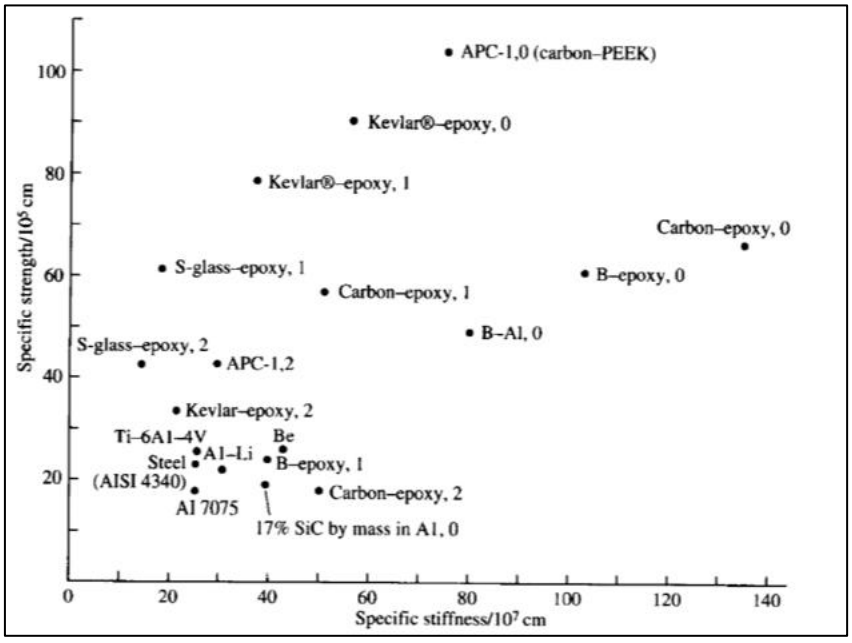

Figure 13 – Specific resistance vs. Specific stiffness of fiber-based composites. Designation “1” represents arrangement with 50% of fibers at 0º, 40% at ± 45º and 10% at 90º from tension direction; “2” represents balanced laminates with 45º, 90º and 135º; “0” predicts aligned fibers in specific matrix (from KELLY [27]).

To select these reinforcements, the specific strength and stiffness, and the relation between them are usually compared, especially for applications which are weight sensitive, such as airplanes, spacecraft or risers. Figure 13 presents a graph of the specific strength in relation to the specific stiffness of the main fiber-based composites used today for systems with fibers in different directions. The most common materials in this family are glass, carbon, aramid, boron and silicon carbide fibers.

Composites reinforced by short or discontinuous fibers, in turn, are not as strong and stiff as those of long fibers and are generally not considered for fabrication of primary structures in critical applications [25]. However, these composites may be attractive for several other applications where complex geometries are required for which, therefore, long fiber composites would not be practical. The short fibers are readily blended to liquid matrices which can be injected or shaped to manufacture various components. These fibers are better addressed in section 2.2.4.

Particle reinforcements tend to offer characteristics and facilities similar to short fibers. An important difference is that the short fibers have well defined length and diameter, generally with a set aspect ratio, while particles have their main dimensions with the same order of magnitude and can either have undefined geometry. A classic example of particle reinforcement is the gravel for concrete [26].

The laminates, in turn, are layers or plies of reinforcements commonly embedded in a matrix. They can be made by different materials, including a composite reinforced with fibers or particles [26].

2.2.2. Matrices and their properties

The matrix of a composite has the function of grouping and bonding the reinforcement to confirm the good transfer of loads between them and therefore providing the new properties of the formed material. In some cases, it can also protect the reinforcement against external damages [25]. Polymers, metals, ceramics or even another composite can perform this role. In many cases, the matrix also contributes to the improvement of some composite properties such as ductility, toughness, and thermal or electrical insulation.

Today, polymers are the most commonly used matrix material, either thermoset or thermoplastic [25, 26, 28]. The thermosets, after curing, have a high density of cross-links (covalent bonds), which generates a stable three-dimensional structure, therefore they do not have a melting point - at high temperatures they degrade rather than melt -

and generally have higher stiffness than thermoplastics. These, in turn, are formed by polymer chains linked to each other basically by secondary bonds. They can melt at high temperatures and harden again once cooled [29].

Epoxies and polyesters are the main examples of thermoset matrices and have been used for decades in the composites because they offer good chemical and thermal stability compared to thermoplastics and good adhesion to fibers [25, 28]. However, some advanced thermoplastics such as PEEK, PEKK and PPS have gained prominence in the market due to their good mechanical properties, low water absorption, ease processing and great thermal stability.

Describing particularly the epoxy resin, it is basically a thermoset polymer, product of the reaction of two components forming generally a tough, thermally and chemically resistant material [30]. First part has commonly at least two compounds, bisphenol A or F and epichlorohydrin, and the second part is the curing agent, which is normally based on amines (both aliphatic/aromatic and primary/secondary), phenols, carboxylic acids, thiols and anhydrides. In first part, Bisphenol A combines one acetone with two phenol groups, while Bisphenol F connect the phenol groups with one methylene. At their extremities, they can react with epichlorohydrin by attaching to its glycidyl groups, which creates either diglycidyl ether bisphenol A (DGEBA) or diglycidyl ether bisphenol F (DGEBF). To facilitate processing or modify properties, other compounds may be included in the solution such as solvents, diluents, plasticizers, accelerators or even fillers.

Thus, a matrix of a composite may have additional components mixed during manufacturing. The fillers, for instance, are generally made of short particles or fibers, and may provide different functions to the matrix and, consequently, to the composite. Weight reduction through glass microspheres, cost reduction by the addition of clay particles, protection against ultraviolet radiation with carbon black [31], and increase of mechanical resistance and toughness through chopped carbon fibers, aramid [32] or carbon nanotubes [33] are examples of materials and improvements for a matrix.

A more detailed description of the addition of particles, short fibers and nanotubes in the matrix is presented in section 2.2.4.

2.2.3. Adhesion between reinforcement and matrix

One of the most important properties for a composite is the adhesion between the reinforcement and the matrix. DILLARD and POCIUS [34] affirm that for a reasonable

understanding of an adhesive joint, as well as its properties and limitations, it is necessary a good knowledge of the substrates and surfaces.

Adhesion may occur by the inter-diffusion of molecules or by chemical or physical bonds between the molecules of the materials in contact; or mechanically, through the contact between peaks and valleys of surface roughness [28, 34], forming a mechanical barrier for the relative displacement between the interfaces (Figure 15e); Therefore, according to SILVA [35], a surface cleaning and treatment is very important to create an optimized adhesive joint.

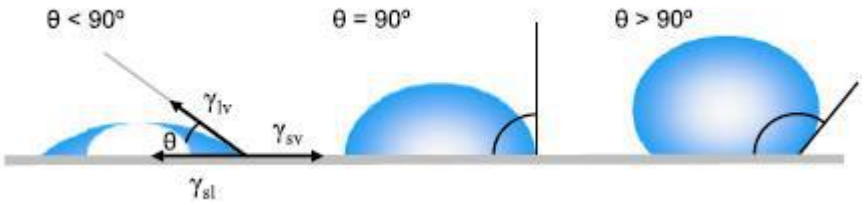

Figure 14 – Illustration of contact angles formed by sessile liquid drops on a smooth homogeneous solid surface (from YUAN and LEE [36]).

The wettability is a property widely used in the study of the interactions between adhesive and adherent [37], which considers, through thermodynamic expressions, the behavior of a liquid drop in contact with a homogeneous solid substrate in a medium with a certain vapor, as shown in Figure 14. The balance of the forces between the drop and the substrate, in equilibrium with the vapor, are expressed by the following relation:

$$\gamma_{sv} = \gamma_{sl} + \gamma_{lv} \cos\theta \qquad (1)$$

where γ represents the surface stresses at the point of contact between the three phases: Solid-vapor (sv), solid-liquid (sl) and liquid-vapor (lv); And θ is the equilibrium contact angle.

Low values of θ ($\ll 90°$) correspond to high wettability [36], and suggest large forces of interfacial attraction between the liquid and the adherent or a tendency to "wet" the substrate and establish an atomic bond with the solid. This wettability can be affected by contaminants present in the adherent, so the importance of preparing the surface before performing the adhesion. Large contact angles ($\gg 90°$) correspond to low wettability.

Figure 15 shows the main forms of adhesion between two surfaces [28]. In Figure 15a) is shown the entanglement between the molecules of the surfaces formed by the inter diffusion between them. The strength of adhesion will depend on the amount of

interlaced chains and their stability. This adhesion is also known as auto adhesion; In Figure 15b), attraction forces occur by the polarity of the surfaces, as in ionic bonds; In Figure 15c), functional groups are used to control pH and polarization for a more effective electrostatic attraction; Chemical bonds such as, covalent and hydrogen bonds are illustrated in Figure 15d); Finally, Figure 15e) shows mechanical adhesion, which can occur basically by interlocking the surfaces by roughness. Depending on the contact pressures between peaks and valleys, micro welds can be formed at some points.

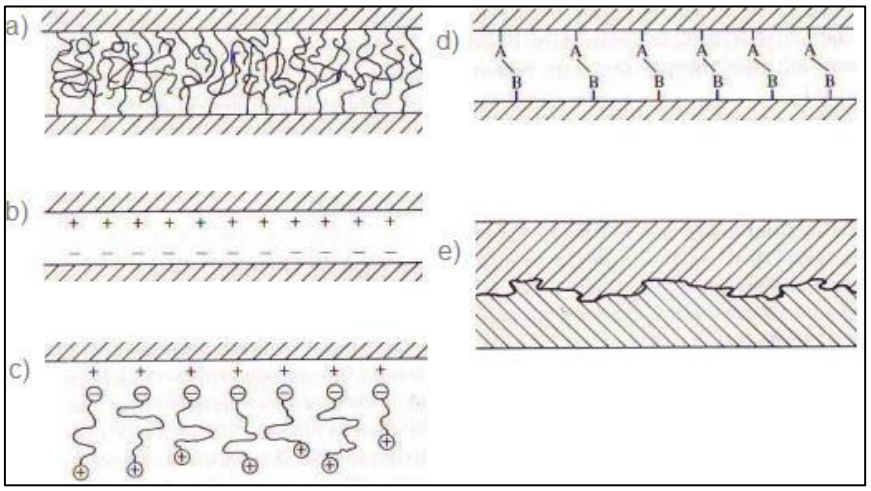

Figure 15 – Adhesion by: a) Molecular tangle and interdiffusion, b) Electrostatic attraction, c) Chemical bond between cathodic groups and anodic surface, d) Chemical bonds of groups A and B, d) Mechanic (from HULL [28]).

It is important to emphasize that one type of adhesion may impact the other. For example, very high roughness with high contact pressures could tend to a good mechanical adhesion, however this roughness can also generate voids between the surfaces due to difference height of peaks and valleys, consequently, water condensation and difficulty to generate chemical bonds [34].

In an epoxy matrix composite with carbon fibers, DRZAL and HERRERA-FRANCO [37] have confirmed that the adhesive system may have large differences in properties depending on surface treatment. Therefore, high scatter may appear not only in the shear strength of the adhesive, but also in the mechanical properties of the composite itself. Figure 16 presents the complexity of a typical interface between a polymer matrix and a fiber reinforcement of a composite.

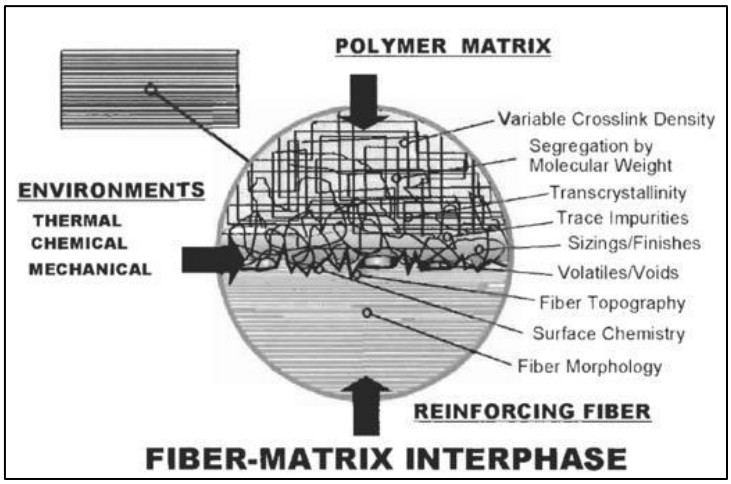

Figure 16 – Example of fiber-matrix interface from a composite (from DILLARD e POCIUS [34]).

The image shows the main adhesion variables of this type of composite. Effects of matrix processing, fiber surface preparation, system moisture, solvent volatility (when used), roughness and possible impurities are examples of parameters that must be properly defined and controlled for the manufacturing of the composite.

Figure 17 shows the most common failure modes in bonded joints. They can be adhesive, which occurs directly at the interface between the adhesive and the substrate; cohesive, the fracture is in the adhesive material; or mixed, when there is a combination of adhesive and cohesive failures. One of composite failures by loss of adhesion between the reinforcement and the matrix is the fiber pull-out, or debonding. Analytical method for this kind of ruin is presented in section 2.3.3.

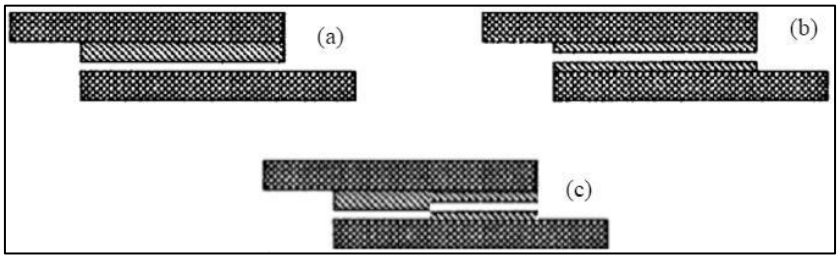

Figure 17 – Typical failures on bonded joints: (a) Adhesive, (b) Cohesive and (c) Mix (from SILVA Figure 17).

2.2.4. Matrix reinforcement as particles and short fibers

As mentioned in section 2.2.1, a composite can have the matrix reinforced by the dispersion of short, or discontinuous, fibers and particles. In this case, they can basically

have orientation aligned with the main axis of the composite, aligned off-axis following a specific angle or randomly oriented. These options are illustrated in Figure 18.

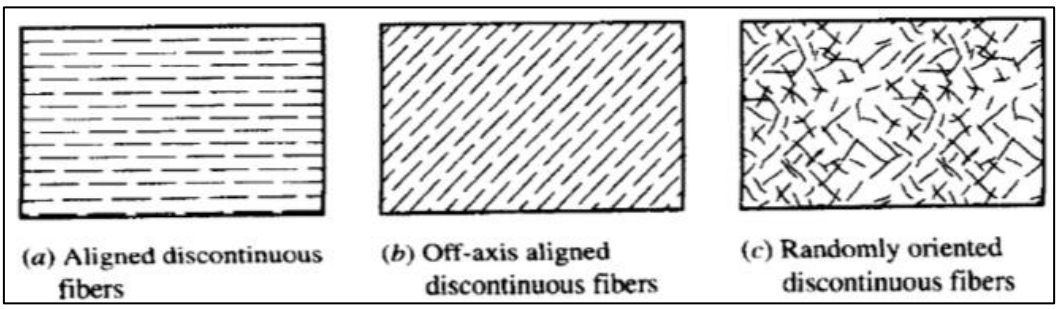

Figure 18 – Composite types reinforced by short or discontinuous: a) Aligned, b) Off-axis aligned, c) Randomly oriented (from GIBSON [25]).

The composites that have randomly oriented short fibers are considered isotropic [25]. However, HULL [28] highlights that, depending on the mixing of the fillers during the processing of the matrix followed by injection of the material into a given chamber, the flow of the fluid may tend the fibers to a preferred orientation. Therefore, it is very important that the protocol for reinforcing the matrix is well studied and consolidated to ensure a homogeneous dispersion, otherwise the properties of the material may have anisotropic characteristics and/or high property dispersion along the material.

Another variable for such phenomenon is the ratio between the fiber length (L) and the composite thickness (t), as presented in Figure 19. Clearly, larger thicknesses and shorter fibers help to have a more homogeneous and isotropic structure. Thus, composites having reinforcement with low aspect ratio (L/d), where d is the fiber diameter, tend to a structure type a) from Figure 19.

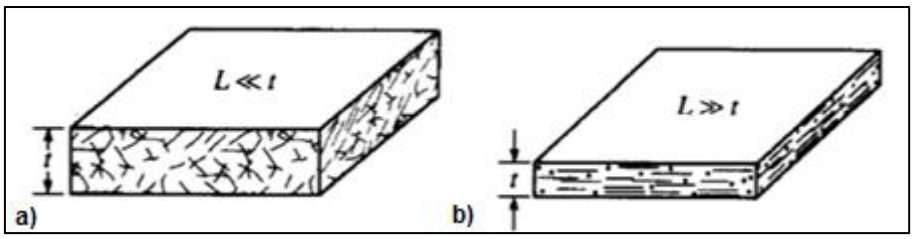

Figure 19 – Randomly orientation of short fibers, a) Fiber length much smaller than thickness part, b) Fiber length much bigger than thickness part (from GIBSON [25]).

COX [38], KHRISTENSEN and WALLS [39] have introduced theoretical concepts for the determination of the elastic constants of an isotropic matrix with short fibers, nevertheless they agreed that mechanical tests are generally the most suitable for the

determination of these properties due to manufacturing variables already mentioned in this section. Therefore, some options of tests are discussed later in section 2.5.

There is a universe of materials, be they short fibers, particles or nanotubes, that can be used as reinforcement of a matrix [40]. The main examples are presented in the following paragraphs referencing works already published. They can be classified by families: Polymeric and ceramic micro particles; Aramid and carbon chopped fibers; and Nano fillers such as Alumina (Al_2O_3), Silicon carbide (SiC), carbon nanotubes (CNTs).

2.2.4.1. Polymeric particles

According to RIEW [41], SOBRINHO *et al.* [42], a method widely used for toughening a composite matrix, especially epoxy resins, is by applying low molar weight liquid rubbers.

Carboxyl-terminated butadiene acrylonitrile copolymer (CTBN) is an example of commonly used elastomer. Figure 20 shows a stress-strain graph comparing a neat and a 10 wt.% CTBN toughened epoxies [42]. Note that the elastomer, in this case, despite having slightly decreased the Young modulus and tensile strength, it has improved the elongation and toughness. Therefore, CTBN is an example of elastomer which could be added in liquid or granulate form to the matrix prior curing.

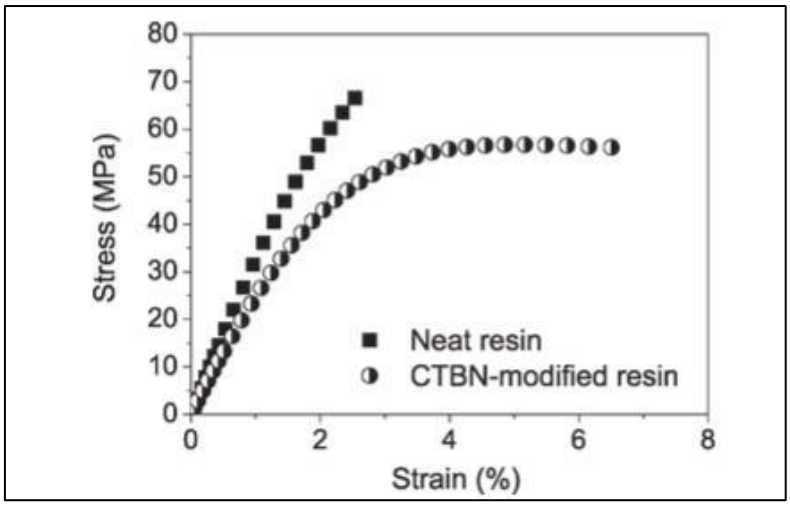

Figure 20 – Stress-strain curve of a neat epoxy resin and 10 wt.% CTBN modified epoxy (from SOBRINHO [42]).

Another elastomer studied by MANDHAKINI *et al.* [31] as reinforcement for epoxies is the carbon black. His work shows that certain concentrations of this material can increase composite toughness by up to 28%.

Polyurethane (PU) is also a reinforcement used by some researchers [43, 44, 45, 46]. Indeed, it confirmed good increase in impact strength. Table 1 presents examples of epoxies with different concentrations of HTPU, and their results in compression and impact.

Table 1 – Impact and compressive properties of HTPU epoxy [46].

	Compression properties				
Weight % of HTPU	Compression strength (MPa)	Increment over matrix (%)	Compression modulus (MPa)	Izod impact strength (J/m)	Increment over matrix (%)
0	48.36	-	2931	30.00	-
1	107.79	122.89	2495	59.81	99.36
2	106.04	119.27	2428	49.72	65.73
3	103.60	114.22	2319	47.32	57.73
4	99.82	106.41	2287	39.00	30.00
5	99.97	106.72	2337	27.19	-9.36

Some thermoplastics can act as fillers for composite matrices as well. Polyamide (PA), Polyimide (PI) [47] and Polytetrafluoroethylene (PTFE) are some examples. KISHORE and KIRAN [48] used PTFE fillers in their research, however they did not reach toughness, but a loss of ductility. The results are shown hereafter in Figure 21.

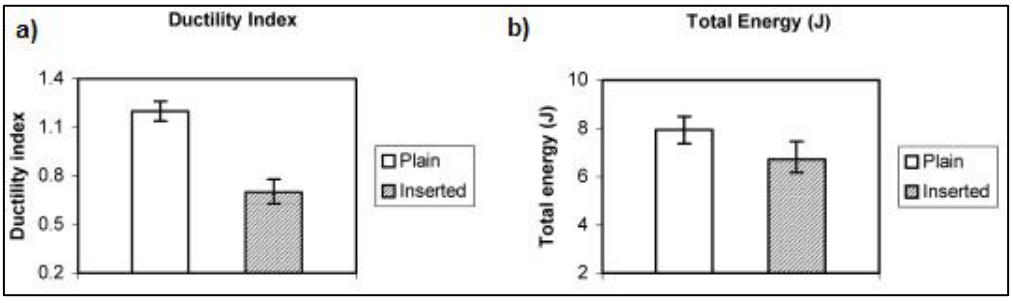

Figure 21 – a) Ductility and b) toughness, analysis of neat and PTFE modified epoxies [48].

The major disadvantage of polymer fillers, especially thermoplastics, is that, although the formed composites may provide good impact resistance, they can also bring new issues such as: reduction of mechanical resistance, reduction of the glass transition temperature (Tg), interfacial wettability problems, thus impacting the adhesion property,

increase of creep and decrease of chemical resistance to solvents and acids [40]. These consequences may be crucial for defining the filler material, especially when it is intended for equipment that will be subjected to corrosive fluids and high loads, such as flexible risers.

2.2.4.2. Aramid short fibers

Aramid is a filler option that has excellent mechanical properties and could be used to reinforce composite matrices. Studies carried out by YASAEE *et al.* [47] compared some methods and proved that Aramid short fibers were one of the most effective for increasing fracture toughness at the interface with the main fibers or reinforcements for the parameters considered. Indeed, by analyzing Figure 13 from section 2.2.1, the Kevlar-epoxy system exhibits high specific strength and stiffness properties, which generally contribute to the toughness of the composite.

SUN *et al.* [32] performed some experiments with different substrates and considered neat and chopped Aramid fibers toughened epoxy adhesives. In the study, it was used fibers with 6 mm length and 12 µm in diameter. Figure 22 shows the surface image of an Aramid short fiber tissue.

Figure 22 – Microscopy of aramid short fiber tissue [32].

Figure 23 illustrates the two adhesive types, with and without short fibers, between metallic and carbon fiber composite substrates, their roughness and their respective mechanisms of crack propagation. The weak adhesive areas of the referenced system shown in Figure 23c) and Figure 23d) confirm the potential gain that could be achieved by adding Aramid short fibers.

SUN *et al.* ratified that the conditions of the substrate surfaces and the density, geometry, volume fraction and dispersed direction of the fibers were very important parameters to achieve good toughness result.

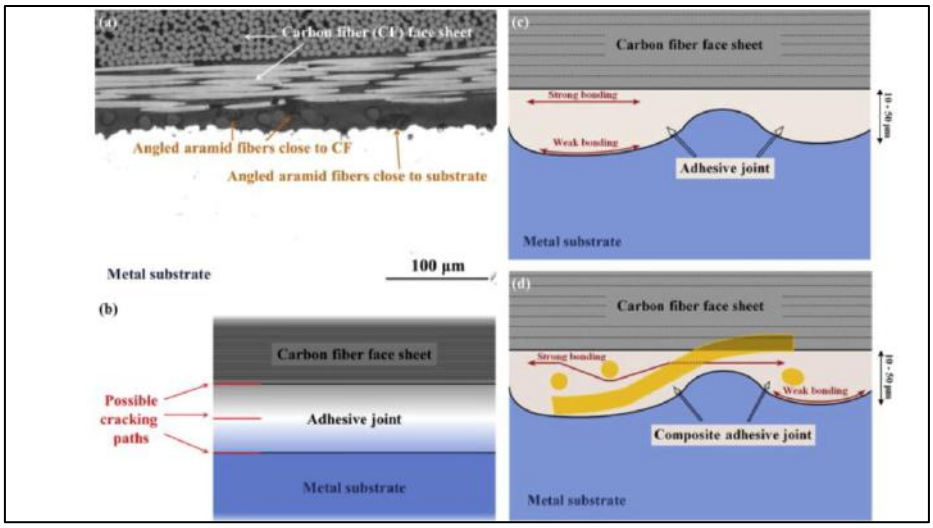

Figure 23 – a) Adhesive toughened with aramid short fibers with approximately 20 μm thick, b) Three potential adhesive crack propagation regions, c) Adhesive without fibers with two potential failure mechanisms, d) Illustration of fibers toughened adhesive with respective failure mechanisms [32].

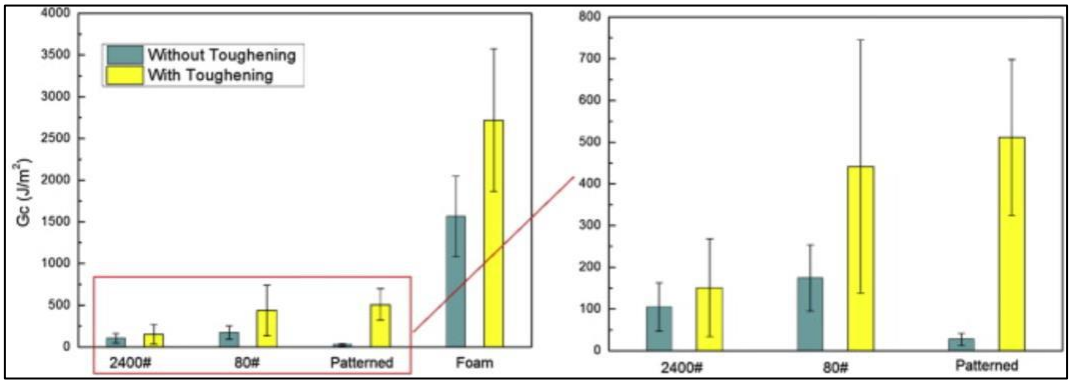

Figure 24 – Comparison of fracture toughness through Griffith energy release between neat and aramid reinforced material [32].

In this study, for all substrates tested, Aramid short fiber reinforced epoxy adhesive demonstrated higher fracture toughness than neat epoxy. The graphs in two scales from Figure 24 demonstrate that the Griffith energy (G), which is directly related with fracture toughness increased by up to 50% for short fiber samples.

Other authors like SOHN and HU [49] and SHI *et al.* [50] also reported improvement in the interlaminar fracture toughness of the composites when using Aramid short fibers as reinforcement of a polymer matrix, particularly for epoxy resins.

2.2.4.3. Mono and multi-walled carbon nanotubes

For the past years, carbon nanotubes (CNTs) have been exhaustive studied as polymer matrix reinforcement, especially for epoxy resin [40, 33, 51]. According to SCHRAND and TOLLE [33], CNTs can be seen as graphene sheets rounded, in tube form, in nanometric scale. They can have one, two or multi-walls, known as single-walled carbon nanotubes (SWCNT), double-walled carbon nanotubes (DWCNT) e multi-walled carbon nanotubes (MWCNT), respectively, as shown in Figure 25. Their geometry provides high ratio surface by weight, thermal and chemical resistance, high electrical and thermal conductivity, and great mechanical properties. Thus, introducing them into an epoxy matrix can give a material with chemical stability, besides high mechanical properties and, therefore, becoming a nanocomposite with high potential for different application. Aerospace agencies like NASA and AFRL, have highly invested in composite developments based on CNTs for satellite and spaceship construction [40].

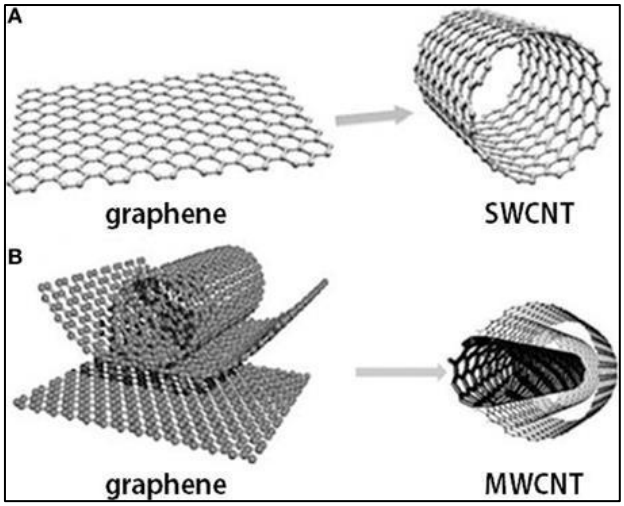

Figure 25 – Correlation between SWCNT, MWCNT and graphene layers [33].

CNTs can be obtained by Pulsed Laser Vaporization (PLV), Chemical Vapour Deposition (CVD), Carbon Arc Discharge (CAD) and High-Pressure Carbon Monoxide (HiPCO) [33, 40].

It is important to highlight, though, that CNTs can bring some drawbacks like raw-material cost and difficulty of processing within matrix. According to THAKRE [40], to ensure the homogeneous dispersion of the CNTs, some mixing techniques and surface treatment

are highly recommended. High shear mixing, ultrasonication and functionalization are some of the most commonly methodologies used.

The improvement of epoxy mechanical properties, such as modulus, tensile strength, elongation and fracture toughness, was already confirmed by many works. ALAMRY *et al.* [52], for instance, reached an increase up to 72% in tensile strength and 124% in fracture toughness with 0,3 wt.% of MWCNT. Results are presented in Table 2.

Table 2 – Properties of tensile samples: Ultimate tensile strength and toughness (from ALAMRY *et al.* [52]).

Specimen	Modulus, (GPa)	Ultimate Tensile Strength, (MPa)	Toughness, (J/mm^2)	Remarks
Pure epoxy	1.52	20.58	1.28	-
0.1 wt.% MWCNT-epoxy	1.92	24.37	1.92	50% increase in toughness
0.3 wt.% MWCNT-epoxy	2.42	35.44	2.87	124.2% increase in toughness

Another study done by LI *et al*. [53] compared mechanical properties of 0.5 wt.% functionalized MWCNT toughened epoxy resin. In Table 3, sample 1 is the neat epoxy; sample 2 had CNTs with no surface treatment; and sample 3 had CNTs with surface treated with 35% of HNO_3 for thirty minutes to create functional groups. From the left, columns from the table are sample number, tensile strength, tensile modulus, elongation, flexion strength, flexion modulus and toughness.

The results show that the functionalized MWCNT composite (sample 3) presented better properties, especially the elongation of 7%, which means an increase of 94% if compared to the neat epoxy (sample 1). It confirms the importance of functionalization of CNTs prior processing within the matrix.

Table 3 – Summary of mechanical properties of epoxy/CNT composite [53].

No.	σ_t (Mpa)	E_t (Gpa)	ε(%)	σ_f (Mpa)	E_f(Gpa)	α_k (N/mm)
1	77	2.7	3.6	199	3.1	1.5
2	88	2.8	4.5	224	3.4	2.6
3	96	2.7	7	244	3.1	2.8

As ratified by BYRNE and GUN'KO [54], CNTs dispersion and surface treatment must be well performed to ensure good stress transfer to polymer chains and then reaching optimized mechanical properties, otherwise it could have interfacial slippage between them or either premature crack in matrix due to the presence of nanotube clusters.

There are two major types of CNT functionalization: Covalent and non-covalent. According to ALAM *et al.* [55], covalent functionalization can be performed by three basic methods: Plasma modification, Mechano-chemistry or Chemical modification. And non-covalent can be done through amine interaction or polymer wrapping. See Figure 26.

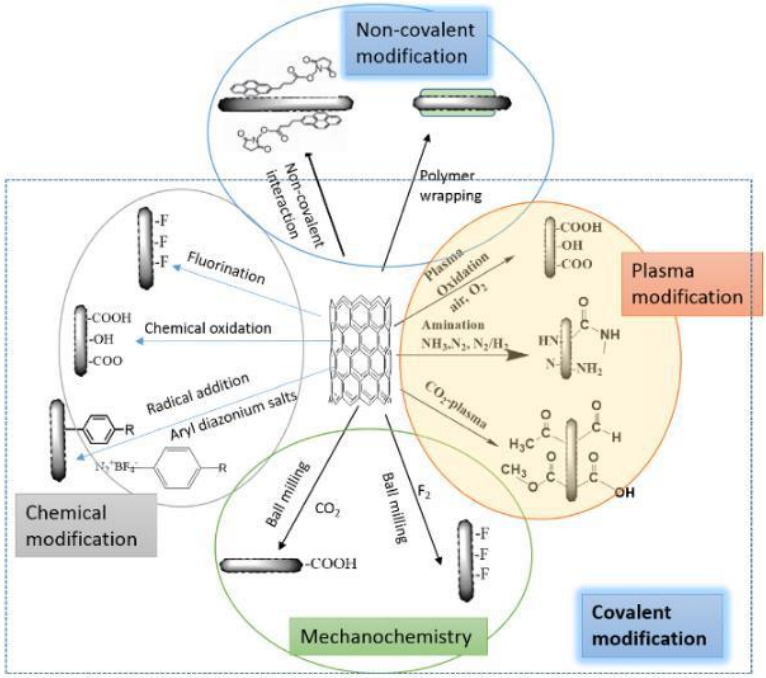

Figure 26 – Surface functionalization methods [55].

The most common functional groups of covalent bonds are COOH- and NH_2-. Although this type of functionalization normally gives better properties, sometimes an issue can arise while treating the nanotubes. The covalent functionalization is done by generating defects on the sidewalls and tube tips, which can serve as anchor groups [56]. Therefore, even respecting meticulously the protocol of treatment, some of CNTs may completely break and the average aspect ratio can be changed, and some properties could be impacted. On the other hand, performing non-covalent π-π interaction with amine groups, for instance, may not brake nanotubes, however it provides weaker bonds. Anyhow, functionalizing carbon nanotubes generally improves the interfacial bonding properties between CNTs and polymer matrix.

KINGSTON *et al.* [57] performed several experiments with SWCNTs, DWCNTs and MWCNTs toughened epoxies with different concentration and NH_2 covalently functionalized. The best results were reached with 0.5 wt.% NH_2-DWCNT epoxy. It presented an increase of 43% in fracture toughness, compared to neat epoxy. CHA *et al.* [58], on the other hand, treated the CNT with non-covalent functionalization with tri-amine π-π bonds and confirmed a gain up to 20% and 40% in tensile strength and fracture toughness, respectively.

CNTs can be combined with other reinforcement material in epoxy matrix, as well. In this case, it is considered a hybrid composite. Silicon Carbide (SiC) and silica (SiO_2), for instance, are particles commonly used as epoxy reinforcement [59], and when combined with MWCNTs, can enhance the materials behavior. JIA *et al.* [60] ratified it on their studies, which confirmed the increase of tensile modulus and tensile strength.

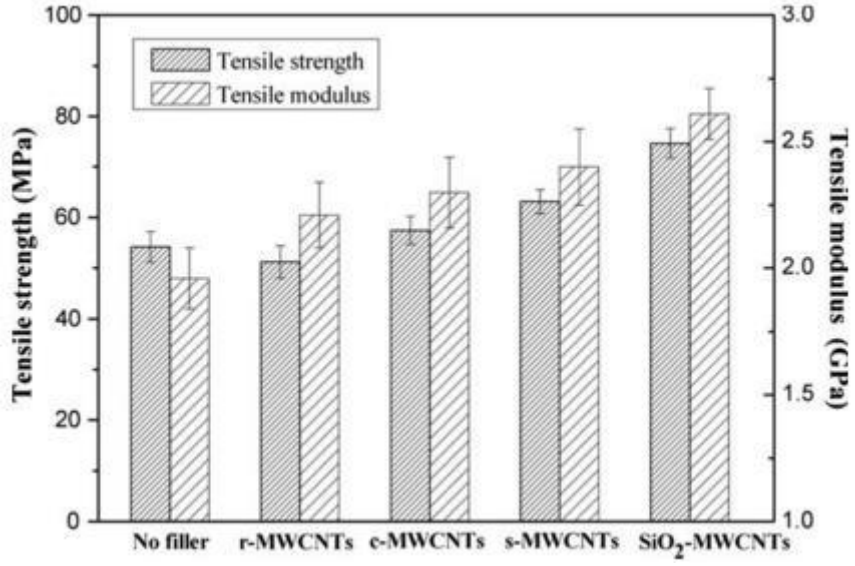

Figure 27 – Tensile strength and modulus of toughened epoxy with 0.5 wt.% functionalized MWCNTs and SiO_2 (JIA *et al.* [60]).

According to all information detailed in section 2.2.4, especially regarding Aramid and CNTs, it can be concluded that a matrix can have one or more types of particles, fibers or nanotubes reinforcement for improving mechanical properties, although their processing and surface treatment should be well studied and defined since they can impact directly on the final performance of the composite.

2.2.5. Hybrid composite

In the beginning of section 2.2, the hybrid composite was defined as a combination of two or more types of reinforcement, either by particles, fibers or laminates from different materials. According to HARRIS [61], the most frequent hybrid composite is obtained by reinforcing with two types of fiber in the matrix. The purpose of designing a hybrid is to optimize its engineering properties, such as mechanical, thermal, chemical and electrical, and manufacturing parameters like processing and cost, for specific applications. Another classic example is the honeycomb, which can be made by paper structure, metal or polymer in a hive-form bonded to thin layers of Fiber Reinforced Plastic (FRP). ARALL [62] also describes an Aramid-Reinforced Aluminum composite, which is made by aluminum plies bonded to Aramid fiber composite ply. Reinforced concrete can be considered a hybrid composite as well, since it is a combination of two different reinforcements, one made of particles, in the case gravel, and the other made of steel rebar.

Therefore, there is countless possibilities for designing a hybrid composite. The mixture of types of reinforcement, whether long fiber with short, particles with blades or other combinations, allows the achievement of an optimized final material, with characteristics specific to a given project. However, it is important to note that defining the properties of a hybrid, as well as its processing, can be complex. Its engineering properties can be defined analytically, for a first approach, considering a combination of micro and macro mechanical methodologies of composites, which are demonstrated in detail by GIBSON [25] e JONES [26], and referenced in the following sections. However, due to the limitations and manufacturing difficulties and to the large number of variables inherent to reinforcement-matrix adhesion already mentioned in section 2.2.3, it is recommended to perform small and real-scale tests for more effective material characterization. Some small-scale tests are cited later in this thesis.

2.2.6. Micromechanics of composites

According to scientists, the term “micromechanics” is the study of mechanical behavior of a material at molecular or crystalline structural level [25]. The discipline is basically based on theory of elasticity and classical mechanics of materials. In this way, the properties of the composite are determined through the volume and weight fractions of constituents and then, according to the geometric organization of the reinforcement, its properties are combined to those of the matrix to define the characteristics of the composite.

At first, for any number of constituent (n), the sum of the volume fractions shall be equal to one:

$$\sum_{i=1}^{n} v_i = 1 \tag{2}$$

where,

$v_i = V_i/V_c$ = volume fraction of the constituent i;

V_i = volume of constituent i;

V_c = Total volume of composite.

That is, for a composite with a matrix and a reinforcement, this equation can be simplified to:

$$v_f + v_m + v_v = 1 \tag{3}$$

where v_f, v_m e v_v are the volume fraction of the fiber, matrix and internal voids, respectively.

Analogously, for the weight fraction w_f of fiber and w_m of matrix, we have the relation:

$$w_f + w_m = 1 \tag{4}$$

Thus, replacing the weights with the product of density and volume in Equation (4), we get the "rule of mixtures" for the density of a composite:

$$\rho_c = \rho_f v_f + \rho_m v_m \tag{5}$$

where ρ_f, ρ_m e ρ_c are the fiber density, matrix and composite, respectively.

It is important to note that Equations (4) and (5) do not consider internal voids. If it is necessary to evaluate the volume fraction of voids v_v, Equation (3) can be rearranged according to the weights and densities:

$$v_v = 1 - \frac{(W_f/\rho_f) + (W_c - W_f)/\rho_m}{W_c/\rho_c} \tag{6}$$

where W_f e W_c are the total weights of fiber and composite, respectively.

According to GIBSON [25], JONES [26] and HULL [28], other properties such as the longitudinal modulus E_1 and the Poisson's coefficient (ν) are also determined by the "rule of mixtures" using elementary mechanics in a representative volume element (RVE) subjected to a simple state of stress, as shown in Figure 28.

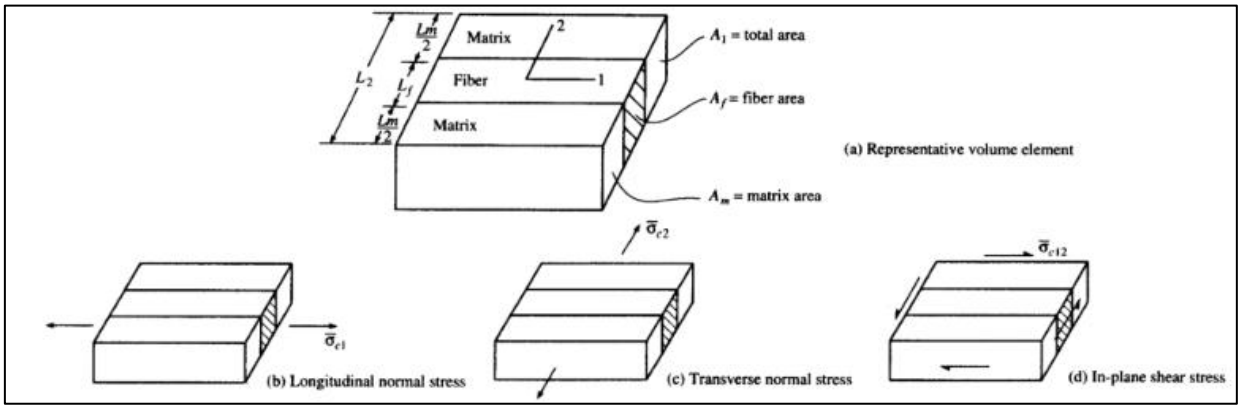

Figure 28 – RVE and stress state of material elementary mechanical model (de GIBSON [25]).

Then, in a composite subjected to a mean longitudinal normal stress ($\bar{\sigma}_{c1}$), its response is governed by the longitudinal modulus (E_1). By the equilibrium and compatibility equations, for an RVE, we have the following relations of tension, deformation and displacement:

$$\bar{\sigma} = \frac{1}{V}\int \sigma \, dV = \frac{1}{A}\int \sigma \, dA \tag{7}$$

$$\bar{\epsilon} = \frac{1}{V}\int \epsilon \, dV = \frac{1}{A}\int \epsilon \, dA \tag{8}$$

$$\bar{\delta} = \frac{1}{V}\int \delta \, dV = \frac{1}{A}\int \delta \, dA \tag{9}$$

where σ, ϵ, δ, *V* and *A* are stress, strain, displacement, volume and stressed face area, respectively.

By the combination of Equation (7) and the equilibrium condition, we have:

$$\bar{\sigma}_{c1}A_1 = \bar{\sigma}_{f1}A_f + \bar{\sigma}_{m1}A_m \tag{10}$$

where the subscript letters c, f and m represent the composite, fiber and matrix, respectively. Since the fractions of area are equal to the corresponding volume fractions, Equation (10) can be rearranged by the rule of the mixtures:

$$\bar{\sigma}_{c1} = \bar{\sigma}_{f1} v_f + \bar{\sigma}_{m1} v_m \tag{11}$$

But, from Hooke's Law, it is known that:

$$\bar{\sigma}_{c1} = E_1 \bar{\epsilon}_{c1}; \quad \bar{\sigma}_{f1} = E_{f1} \bar{\epsilon}_{f1}; \quad \bar{\sigma}_{m1} = E_m \bar{\epsilon}_{m1}; \tag{12}$$

Replacing in (11):

$$E_1 \bar{\epsilon}_{c1} = E_{f1} \bar{\epsilon}_{f1} v_f + E_m \bar{\epsilon}_{m1} v_m \tag{13}$$

where E_{f1} is the fiber longitudinal modulus and E_m is the matrix modulus, considered isotropic.

Finally, assuming that the mean strain of the composite, fiber and matrix are equal at longitudinal direction:

$$\bar{\epsilon}_{c1} = \bar{\epsilon}_{f1} = \bar{\epsilon}_{m1} \tag{14}$$

Replacing (14) in (13) we reach the longitudinal elastic modulus:

$$E_1 = E_{f1} v_f + E_m v_m \tag{15}$$

From the same “rule of mixtures”, the Poisson's coefficient is given by:

$$\nu_{12} = \nu_{f12} v_f + \nu_m v_m \tag{16}$$

From the above demonstration, the elementary mechanics models for E_1 and ν_{12} are effective. However, for the elastic modulus E_2 and shear G_{12}, GIBSON [25] and JONES [26] showed that these models do not present results with a good representability of reality.

Therefore, HOPKINS *et al*. [63] developed a specific refined model for these moduli. Basically, the model starts from a RVE which is divided into three sub-regions considering fiber with square section with the same volume fraction of rounded fiber as shown in Figure 29.

The relationship between the cross-sectional areas of the round and square fibers is given by:

$$s_f = \sqrt{\frac{\pi}{4}} d \tag{17}$$

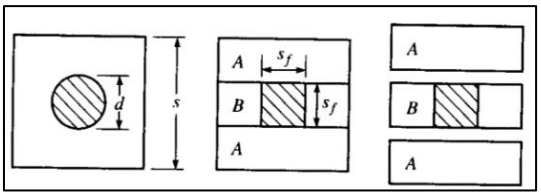

Figure 29 – Division of RVE based in square fiber with equivalent volume fraction (from GIBSON [25]).

It is known that the RVE area, according to GIBSON [25], is:

$$s = \sqrt{\frac{\pi}{4v_f}}d \tag{18}$$

Following the relation of the inverse “rule of mixtures", also presented by GIBSON [25] and JONES [26], we obtain the effective transverse modulus of sub region B, E_{B2}:

$$\frac{1}{E_{B2}} = \frac{1}{E_{f2}}\frac{s_f}{s} + \frac{1}{E_m}\frac{s_m}{s} \tag{19}$$

where the matrix area is $s_m = s - s_f$. Then, considering

$$\sqrt{v_f} = \frac{s_f}{s} \tag{20}$$

and

$$1 - \sqrt{v_f} = \frac{s_m}{s} \tag{21}$$

Therefore, Equation (19) becomes:

$$E_{B2} = \frac{E_m}{1 - \sqrt{v_f}\left(1 - E_m/E_{f2}\right)} \tag{22}$$

Thus, by combining the sub regions A and B of the RVE subjected to a transverse normal stress, we can use the direct "rule of mixtures":

$$E_2 = E_{B2}\frac{s_f}{s} + E_m\frac{s_m}{s} \tag{23}$$

Finally, substituting Equations (20), (21) and (22), we reach the most effective formula of the transverse elastic modulus E_2:

$$E_2 = E_m \left[\left(1 - \sqrt{v_f}\right) + \frac{\sqrt{v_f}}{1 - \sqrt{v_f}\left(1 - E_m/E_{f2}\right)} \right] \tag{24}$$

Similarly, for the shear modulus G_{12}:

$$G_{12} = G_m \left[\left(1 - \sqrt{v_f}\right) + \frac{\sqrt{v_f}}{1 - \sqrt{v_f}\left(1 - G_m/G_f\right)} \right] \tag{25}$$

The “rule of mixtures” can also be applied to micromechanical models for longitudinal stress analysis. Figure 30 presents the typical stress-strain graphs of the fiber, matrix and the respective composite for two cases: Composite whose failure occurs in the fiber (Figure 30(a)) and in the matrix (Figure 30(b)).

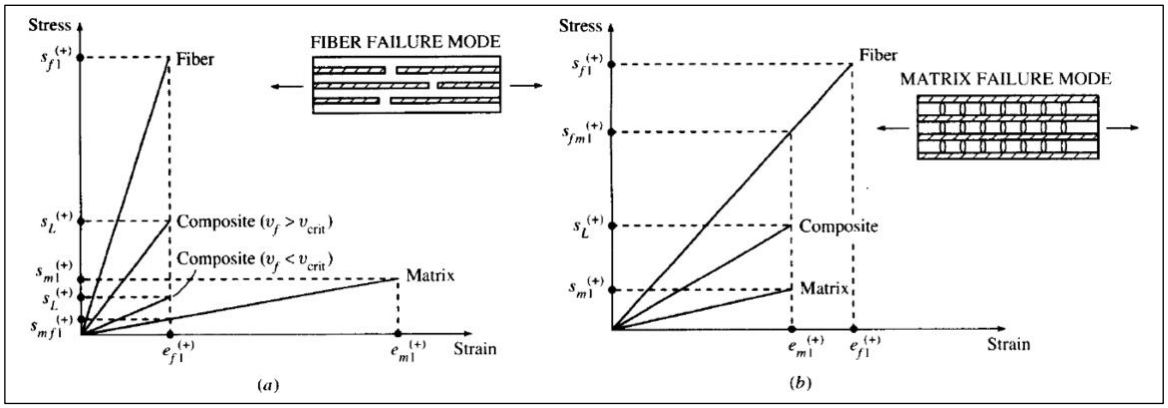

Figure 30 – Typical stress-strain graph representative of fiber, matrix and composite, a) Matrix maximum deformation greater than fiber’s, b) Fiber maximum deformation greater than matrix’s (from GIBSON [25]).

where,

$S_{f1}^{(+)}$ = Fiber ultimate tensile strength;

$S_L^{(+)}$ = Composite ultimate tensile strength;

$S_{m1}^{(+)}$ = Matrix ultimate tensile strength;

$S_{mf1}^{(+)}$ = Matrix ultimate stress limited by fiber maximum strain;

$\epsilon_{f1}^{(+)}$ = Fiber maximum strain;

$\epsilon_{m1}^{(+)}$ = Matrix maximum strain.

The model (a) is typical of composites of polymeric matrix, while the model (b) of ceramic matrix. For both cases, the assumptions adopted are that the stress is homogeneously distributed in all the composite fibers, the behavior until failure is elastic and the longitudinal deformation of the composite, fiber and matrix are equal. Thus, for case (a), where the failure occurs in the matrix, the stresses in the fibers reach the value $S_{f1}^{(+)}$, the stress in the matrix reaches $S_{mf1}^{(+)} = E_m \epsilon_{f1}^{(+)}$ and the stress in the composite reaches $S_L^{(+)}$. Therefore, by the "rule of mixtures", Equation (11) is updated:

$$S_L^{(+)} = S_{f1}^{(+)} v_f + S_{mf1}^{(+)} v_m = S_{f1}^{(+)} v_f + S_{mf1}^{(+)} (1 - v_f) \tag{26}$$

It is important to remember that this relation is valid for cases where the volume fraction of fibers *(v_f)* is sufficiently large. That is, in case $v_f < v_{crit}$, the stress $S_L^{(+)}$ will be smaller than the matrix ultimate tensile stress $S_{m1}^{(+)}$, where:

$$v_{crit} = \frac{S_{m1}^{(+)} - S_{mf1}}{S_{f1}^{(+)} - S_{mf1}} \tag{27}$$

as shown in Figure 30(a) and Figure 31(a).

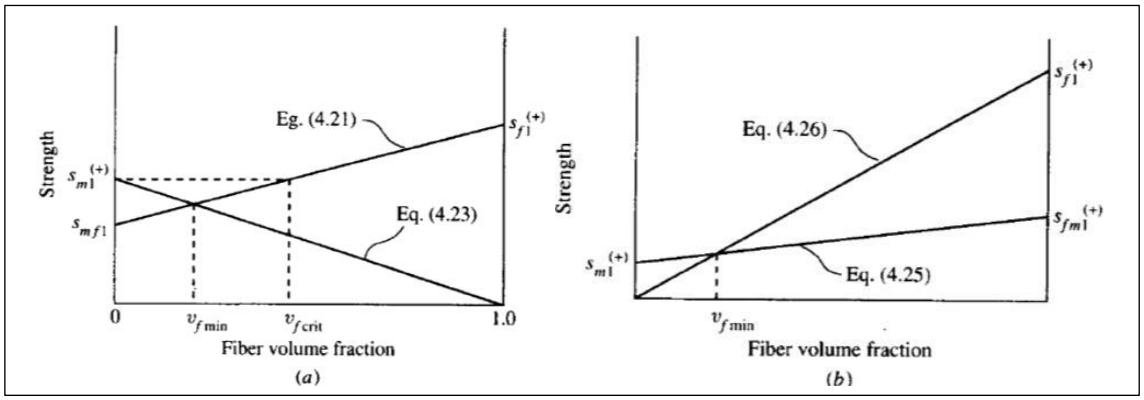

Figure 31 – Relation of composite ultimate tensile strength to fiber volume fraction *(v_f)*, a) Matrix maximum deformation greater than fiber's, b) Fiber maximum deformation greater than matrix's (from GIBSON [25]).

Therefore, it is important noting that the equations defined for longitudinal stress, and longitudinal, transverse and shear modulus and Poisson's coefficient are applicable only for long, or continuous, fiber composites. That is why there is a relationship proposed by KELLY-TYSON [64] between the dimension of fiber and its properties, and the interface shear strength with the matrix (τ_y), as presented in Equation (28). It defines the non-

effective length of fiber (L_i) from which the transfer of loads between matrix and fiber begins to occur [25].

$$L_i = \frac{dE_{f1}\sigma_{c1}}{2\tau_y E_1} \tag{28}$$

where d is the fiber diameter and σ_{c1} is the composite stress.

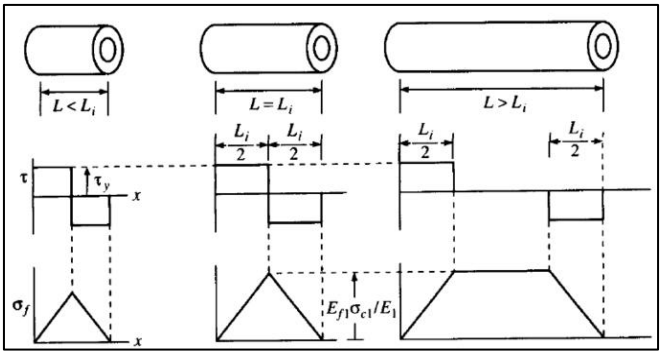

Figure 32 – Fiber length effect on stress distribution along fiber (KELLY-TYSON [64]).

Through Equation (28), another relation with fiber length can be obtained, which defines the critical length (L_c) from which the fiber maximum stress $s_{f1}^{(+)}$ is reached in the composite. It is assumed, then, that $s_{f1}^{(+)} \geq E_{f1}\sigma_{c1}/E_1$, resulting in Equation (29) as following:

$$L_c = \frac{ds_{f1}^{(+)}}{2\tau_y} \tag{29}$$

2.2.7. Macro-mechanics of laminates

In the previous section, some micromechanics topics were presented, which deal basically with essential orthotropic composite properties. However, composite structures have been lately designed as laminates, made by the assembly of several laminas (or plies), in straight, bent or tube shape, for instance, oriented in specific directions and bonded together [25]. In this way, the final design of the composite structure can provide optimized mechanical properties for each application.

Figure 33 shows a laminate antisymmetric with four plies with their fibers aligned at -45°, +45°, -45°, +45°.

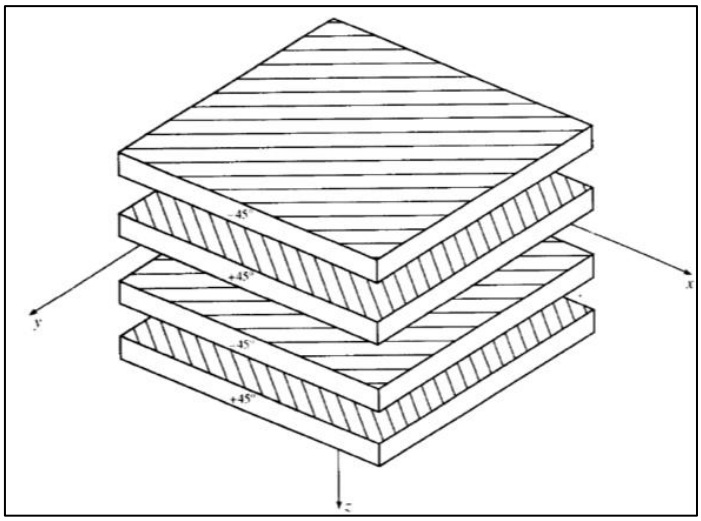

Figure 33 – Exploded view of antisymmetric laminate [-45°/+45°/-45°/+45°] (from GIBSON [25]).

Classical Lamination Theory was developed in the 50's by scientists like SMITH [65] and PISTER *et al.* [66]. The macro-mechanics theory allowed designing and evaluating composites with complex configuration, with several plies and different fiber directions to enable withstanding external loads, even if combined, such as axial forces, bending and torsional moments [25, 26]. An important limitation of this theory is that interlaminar and fiber-matrix interface stresses are neglected. In this work, this second phenomenon is addressed in section 2.3 through fracture mechanics theory.

For the development of macro-mechanics of laminates, classical equilibrium equations are used, and some basic premises are adopted [67], such as:

- Plies are orthotropic, with unidirectional fibers, and bonded to each other, with main axis oriented in arbitrary directions with respect to *x*-*y* axis (Figure 33);
- Ply thickness (t_L) is constant and much smaller than ply's length and width;
- Displacements (u, v and w) are small, if compared to ply thickness;
- The in-plane strains (ϵ_x, ϵ_y and γ_{xy}) are small, if compared with unit;
- Transverse shear strains (γ_{xz} and γ_{yz}) are neglected;
- Tangential displacements (u and v) are linear functions of *z* coordinate;
- Transverse normal strain (ϵ_z) is neglected;

- Each ply follows Hooke's law;
- Transverse shear stresses (τ_{xz} and τ_{yz}) disappear on the laminate surfaces.

From these premises, GIBSON [25] and JONES [26] developed the correlation between strains, displacements and external loads to reach the following stresses σ_x, σ_y and τ_{xy} from ply *k*:

$$\begin{Bmatrix} \sigma_x \\ \sigma_y \\ \tau_{xy} \end{Bmatrix}_k = \begin{bmatrix} \bar{Q}_{11} & \bar{Q}_{12} & \bar{Q}_{16} \\ \bar{Q}_{21} & \bar{Q}_{22} & \bar{Q}_{26} \\ \bar{Q}_{61} & \bar{Q}_{62} & \bar{Q}_{66} \end{bmatrix}_k \begin{Bmatrix} \epsilon_x^0 + zK_x \\ \epsilon_y^0 + zK_y \\ \gamma_{xy}^0 + zK_{xy} \end{Bmatrix} \tag{30}$$

where K_x, K_y and K_{xy}, are curvatures associated with moments at the middle of surface at planes xz, yz and xy, respectively, and $\bar{Q}_{ij}$ are the components of the stiffness transformed matrix of the ply.

$\bar{Q}_{ij}$ is given by the linear transformation of components from the main fiber axis to the main laminate axis [25]:

$$\begin{aligned} \bar{Q}_{11} &= Q_{11}\cos^4\theta + Q_{22}\sin^4\theta + 2(Q_{12} + 2Q_{66})\sin^2\theta\cos^2\theta \\ \bar{Q}_{12} &= (Q_{11} + Q_{22} - 4Q_{66})\sin^2\theta\cos^2\theta + Q_{12}(\cos^4\theta + \sin^4\theta) \\ \bar{Q}_{22} &= Q_{11}\sin^4\theta + Q_{22}\cos^4\theta + 2(Q_{12} + 2Q_{66})\sin^2\theta\cos^2\theta \\ \bar{Q}_{16} &= (Q_{11} - Q_{12} - 2Q_{66})\cos^3\theta\sin\theta - (Q_{22} - Q_{12} - 2Q_{66})\cos\theta\sin^3\theta \\ \bar{Q}_{26} &= (Q_{11} - Q_{12} - 2Q_{66})\cos\theta\sin^3\theta - (Q_{22} - Q_{12} - 2Q_{66})\cos^3\theta\sin\theta \\ \bar{Q}_{66} &= (Q_{11} + Q_{22} - 2Q_{12} - 2Q_{66})\sin^2\theta\cos^2\theta + Q_{66}(\sin^4\theta + \cos^4\theta) \end{aligned} \tag{31}$$

Figure 34 presents the convention adopted for orientation θ of ply fibers.

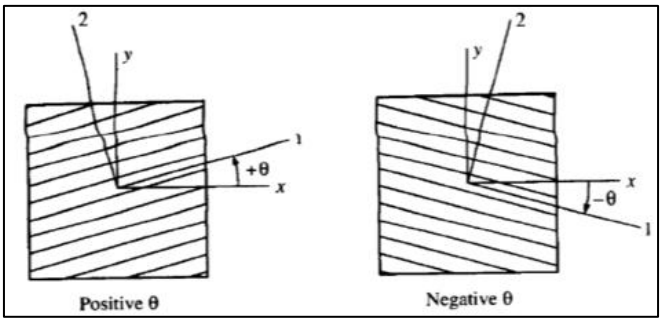

Figure 34 – Convention of ply fibers orientation (from GIBSON [25]).

And, the components Q_{ij} of the ply stiffness matrix at fiber direction prior transformation are given by [25, 26]:

$$Q_{11} = \frac{E_1}{1 - \nu_{12}\nu_{21}}$$

$$Q_{12} = Q_{21} = \frac{\nu_{12}E_2}{1 - \nu_{12}\nu_{21}} \tag{32}$$

$$Q_{22} = \frac{E_2}{1 - \nu_{12}\nu_{21}}$$

$$Q_{66} = G_{12}$$

where E_1, E_2, ν_{12}, ν_{21} e G_{12} are the constants of the composite already mentioned in section 2.2.6. Therefore, the ply stiffness matrix *[Q]* at fiber direction, considering $\tau_{xz} = \tau_{yz} = \sigma_z = 0$, is:

$$[Q] = \begin{bmatrix} Q_{11} & Q_{12} & 0 \\ Q_{21} & Q_{22} & 0 \\ 0 & 0 & Q_{66} \end{bmatrix} \tag{33}$$

In Equation (30), the analysis of the strains and curvatures are related to the forces and moments applied by the equilibrium equations. However, for laminates, it is more convenient to use forces and moments per unit length. The forces and moments per unit of measurement may also be relative to the resulting stresses shown in Figure 35.

Therefore, the force N_x and the moment M_x per unit length are given by:

$$N_x = \int_{-t_L/2}^{t_L/2} \sigma_x \, dz = \sum_{k=1}^{N} \left\{ \int_{z_k - 1}^{z_k} (\sigma_x)_k dz \right\} \tag{34}$$

$$M_x = \int_{-t_L/2}^{t_L/2} \sigma_x z \, dz = \sum_{k=1}^{N} \left\{ \int_{z_k - 1}^{z_k} (\sigma_x)_k z dz \right\} \tag{35}$$

where,

$z_k - 1$ = Distance from middle surface to inner surface of the *k^th^* ply*;*

z_k = Distance from middle surface to outer surface of the *k^th^* ply (Figure 36);

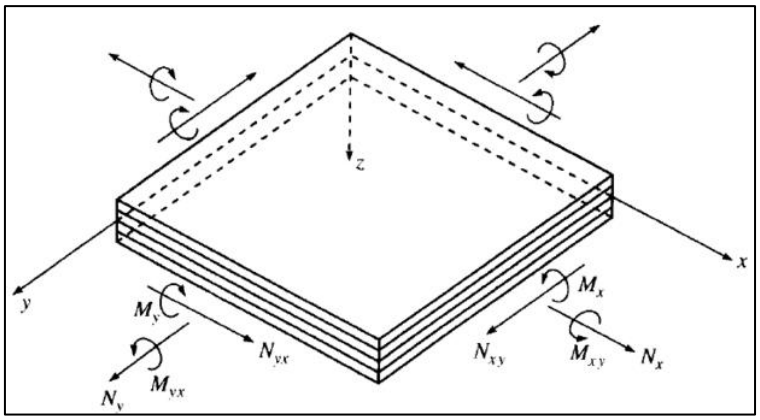

Figure 35 – Coordinate system of stress state on laminate (from GIBSON [25]).

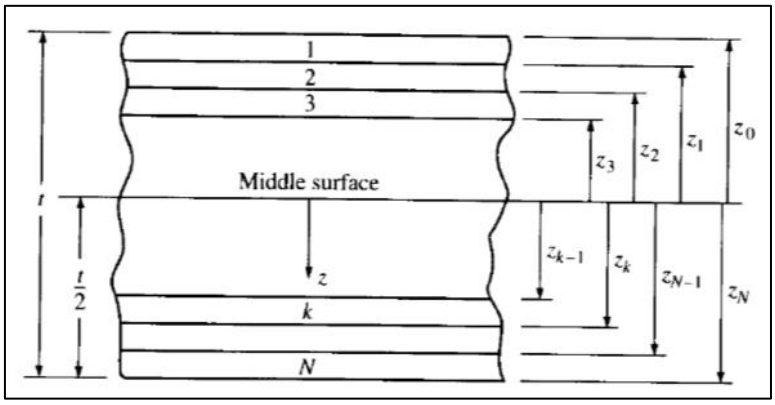

Figure 36 – Laminate geometry and plies numbering (from GIBSON [25]).

Substituting the stress-strain relationship of Equation (30) in Equations (34) and (35):

$$N_x = \sum_{k=1}^{N} \int_{z_k-1}^{z_k} \{(\bar{Q}_{11})_k(\epsilon_x^0 + zk_x) + (\bar{Q}_{12})_k(\epsilon_y^0 + zk_y) + (\bar{Q}_{16})_k(\gamma_{xy}^0 + zk_{xy})\}dz \quad (36)$$

$$M_x = \sum_{k=1}^{N} \int_{z_k-1}^{z_k} \{(\bar{Q}_{11})_k(\epsilon_x^0 + zk_x) + (\bar{Q}_{12})_k(\epsilon_y^0 + zk_y) + (\bar{Q}_{16})_k(\gamma_{xy}^0 + zk_{xy})\}zdz \quad (37)$$

Rearranging and renaming the terms of Equations (36) and (37):

$$N_x = A_{11}\epsilon_x^0 + A_{12}\epsilon_y^0 + A_{16}\gamma_{xy}^0 + B_{11}k_x + B_{12}k_y + B_{16}k_{xy} \quad (38)$$

$$M_x = B_{11}\epsilon_x^0 + B_{12}\epsilon_y^0 + B_{16}\gamma_{xy}^0 + D_{11}k_x + D_{12}k_y + D_{16}k_{xy} \quad (39)$$

where the axial stiffness matrices *[A]*, torsional *[B]* and flexional *[D]* are respectively:

$$A_{ij} = \int_{-t_L/2}^{t_L/2} \left(\bar{Q}_{ij}\right)_k dz = \sum_{k=1}^{N} \left(\bar{Q}_{ij}\right)_k (z_k - z_{k-1}) \tag{40}$$

$$B_{ij} = \int_{-t_L/2}^{t_L/2} \left(\bar{Q}_{ij}\right)_k z\, dz = \frac{1}{2}\sum_{k=1}^{N} \left(\bar{Q}_{ij}\right)_k \left(z_k^2 - z_{k-1}^2\right) \tag{41}$$

$$D_{ij} = \int_{-t_L/2}^{t_L/2} \left(\bar{Q}_{ij}\right)_k z^2\, dz = \sum_{k=1}^{N} \left(\bar{Q}_{ij}\right)_k \left(z_k^3 - z_{k-1}^3\right) \tag{42}$$

The indices i and j are $1, 2\ or\ 6$. The other resulting components of stress are expressed analogously. Thus, the complete strain-strain relationship can be written as:

$$\begin{Bmatrix} N_x \\ N_y \\ N_{xy} \\ M_x \\ M_y \\ M_{xy} \end{Bmatrix} = \begin{bmatrix} A_{11} & A_{12} & A_{16} & B_{11} & B_{12} & B_{16} \\ A_{12} & A_{22} & A_{26} & B_{12} & B_{22} & B_{26} \\ A_{16} & A_{26} & A_{66} & B_{16} & B_{26} & B_{66} \\ B_{11} & B_{12} & B_{16} & D_{11} & D_{12} & D_{16} \\ B_{12} & B_{22} & B_{26} & D_{12} & D_{22} & D_{26} \\ B_{16} & B_{26} & B_{66} & D_{16} & D_{26} & D_{66} \end{bmatrix} \begin{Bmatrix} \epsilon_x^0 \\ \epsilon_y^0 \\ \gamma_{xy}^0 \\ k_x \\ k_y \\ k_{xy} \end{Bmatrix} \tag{43}$$

or

$$\begin{Bmatrix} N \\ M \end{Bmatrix} = \begin{bmatrix} A & B \\ B & D \end{bmatrix} \begin{Bmatrix} \epsilon \\ k \end{Bmatrix} \tag{44}$$

Now, if considering a cylindric laminate, that is a tube which has its thickness made of laminate with several plies and their fibers helicoidally organized, the above matrices need to be translated to the cylindrical coordinates using the parallel axis theorem, as proposed by RAO [68].

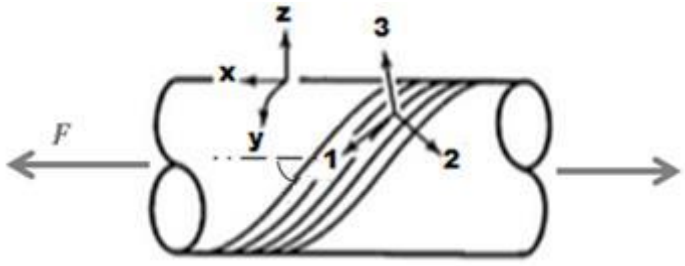

Figure 37 – Laminated composite tube with coordinates at tube and fibers main axis.

Thus, since $z = r\cos\theta$, the new stiffness matrices from equations (40) to (42) are given by:

$$A'_{ij} = A_{ij} \tag{45}$$

$$B'_{ij} = B_{ij} + r\cos\theta\, A_{ij} \tag{46}$$

$$D'_{ij} = D_{ij} + 2r\cos\theta\, B_{ij} + (r\cos\theta)^2 A_{ij} \tag{47}$$

Then, the same relation is respected for stresses and strain:

$$\begin{Bmatrix} N' \\ M' \end{Bmatrix} = \begin{bmatrix} A' & B' \\ B' & D' \end{bmatrix} \begin{Bmatrix} \epsilon \\ k \end{Bmatrix} \tag{48}$$

It is important to note that the macro-mechanical relationships presented in this section consider a composite with its reinforcement perfectly adhered to the matrix, that is, interlaminar stresses or the study of the debonding between reinforcement and matrix are not addressed. Nevertheless, it is known that these phenomena can reduce the failure stress of the material, which is evaluated here in the plane of the ply, since it could become the mechanical fuse of the composite. Therefore, the study of debonding propagation and debonding will be treated in section 2.3 through fracture mechanics theory.

2.3. LINEAR ELASTIC FRACTURE MECHANICS (LEFM)

The previous sections 2.2.6 and 2.2.7 deal with the concepts commonly used in the theory of composite materials for the evaluation of their properties and their stress-strain relationship when subjected to external loads. GIBSON [25] and JONES [26] also present some acceptance criteria to guarantee a reliable composite design. Tsai-Wu failure criterion [69], for example, is a widely-used theory for predicting the rupture of laminate composites and seems to be quite accurate. However, these discussions do not approach analysis of the debonding mechanism of fiber-matrix due to effects of possible indentations, cracks, delamination or discontinuities that may exist. And this work deals with this issue in a specific area of the EF of flexible riser.

Defects may arise in the composites, for example, during the injection and curing of their matrix. Bubbles, microcracks and loss of reinforcement adhesion due to the residual stresses generated by its contraction are some examples that can occur in these materials. Therefore, Fracture Mechanics is a very important theory for helping to define failure criteria of composites.

According to SHUKLA [70], the fracture toughness of a composite is usually measured in terms of the stress levels in the defect region, so called stress intensity factor (K), or

the energy release (G), well known as Griffith energy. Both parameters are fundamental principles of Linear Elastic Fracture Mechanics (LEFM) and will be addressed in the following sections. Then, these factors are related to the debonding between reinforcement and matrix of a composite.

2.3.1. Griffith's Energetic Balance *G*

The work on the stability of cracks in a body when subjected to a load through the energy balance was published by Griffith in 1921 [71]. According to SHUKLA [70], he was the first to take the theory of fracture mechanics further in which a small crack becomes unstable in a stressed body. The analysis is based on the elastic potential energy variation of the component.

Thus, considering a plate subjected to a stress σ and with a defect in the middle with length $2a$, as presented in Figure 38, we have:

$$U = U_0 + U_a + U_\gamma - F \tag{49}$$

where,

U_0 = Energy of the plate and its system without the crack;

U_a = Energy released of the plate with the crack;

U_γ = Surface energy;

F = Work performed by the system with the crack.

For thin plates, that is, in plane stress state [72]:

$$U_a = -\frac{\pi\sigma^2 a^2}{E} \tag{50}$$

And the energy required to create new surfaces is, [71]:

$$U_\gamma = 4a\gamma_e \tag{51}$$

where γ_e is the surface stress.

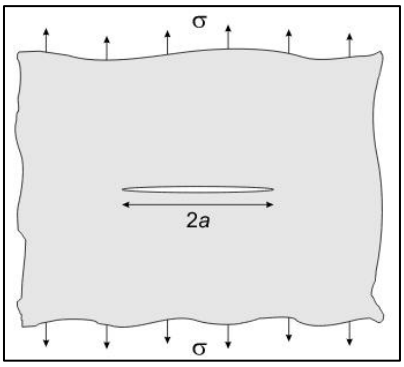

Figure 38 – Illustration of defect (*2a)* throughout thickness in theoretical infinite plate subjected to distributed tensile load (JANSSEN *et al.* [72]).

In a system loaded with constant displacement, that is, $\sum F = 0$:

$$U = U_0 + U_a + U_\gamma = U_0 - \frac{\pi\sigma^2 a^2}{E} + 4a\gamma_e \tag{52}$$

According to Griffith, crack propagates only if the system's energy decreases:

$$\frac{dU}{d(2a)} = \frac{d}{d(2a)}\left(U_a + U_\gamma\right) = \frac{d}{d(2a)}\left(-\frac{\pi\sigma^2 a^2}{E} + 4a\gamma_e\right) < 0 \tag{53}$$

That is, only if:

$$\frac{\pi\sigma^2 a}{E} < 2\gamma_e \tag{54}$$

The graph of Figure 39 shows the variation of the energies in relation to the length of the crack (*2a)*. In this case, a_c is the critical length from which the total energy of the system decreases. According to Griffith, this is the point of instability of the crack, where its propagation may occur.

Therefore, in the plane stress state, Griffith's Equation can be written as:

$$G = \frac{\pi\sigma^2 a}{E} > G_c = 2\gamma_e \tag{55}$$

where G is the rate of release of elastic energy from the system and G_c is the resistance to crack growth, property of the material.

In the plane strain state, G can be written as [70]:

$$G = \frac{\pi\sigma^2 a}{E}(1-\nu^2) \tag{56}$$

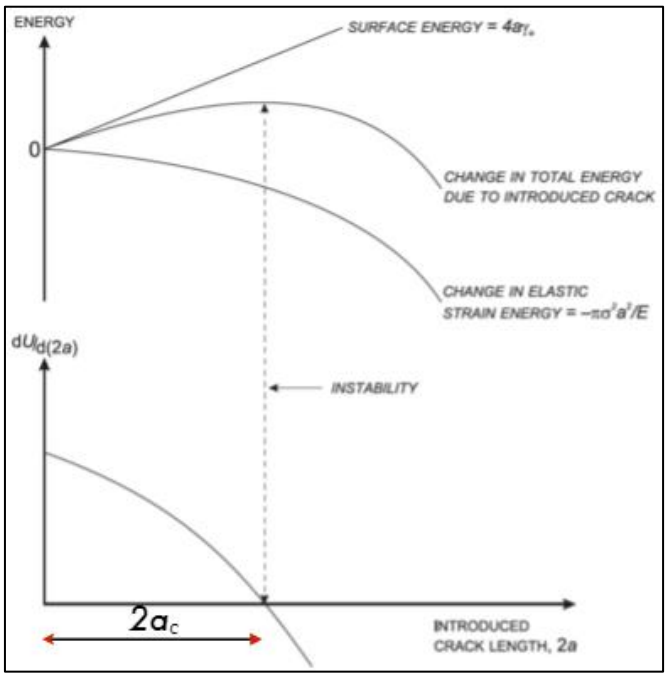

Figure 39 – Relation between energy variation of the system and crack length (*2a)*.

2.3.2. Stress intensity factor *K*

Few years after Griffith's fracture criterion was presented, IRWIN [73] and OROWAN [74] suggested a modification based on the idea that the resistance of a material to the crack propagation is due to the combination of the elastic surface energy effects and the plastic deformation work. Thus, considering the stress distribution around the crack tip, another interpretation of the Griffith analysis could be developed for stress states other than simple uniaxial stress [25].

The three basic modes of crack propagation are illustrated in Figure 40. According to STROHAECKER [75], mode I refers to the opening at the crack tip; Mode II shows the crack propagation by pure shear, that is, displacement of the crack surfaces parallel to each other and perpendicular to the propagation front; And mode III is the crack tearing or, in other words, the displacement of the crack surfaces parallel to each other and to the front of propagation.

Thus, considering a plane stress state near a crack subjected to a uniaxial loading according to Figure 41, the stress analysis at a point *P* in the elastic domain can be expressed by [25]:

$$\sigma_x = \frac{\sigma\sqrt{\pi a}}{\sqrt{2\pi r}} f_1(\theta) \tag{57}$$

$$\sigma_y = \frac{\sigma\sqrt{\pi a}}{\sqrt{2\pi r}} f_2(\theta) \tag{58}$$

$$\tau_{xy} = \frac{\sigma\sqrt{\pi a}}{\sqrt{2\pi r}} f_3(\theta) \tag{59}$$

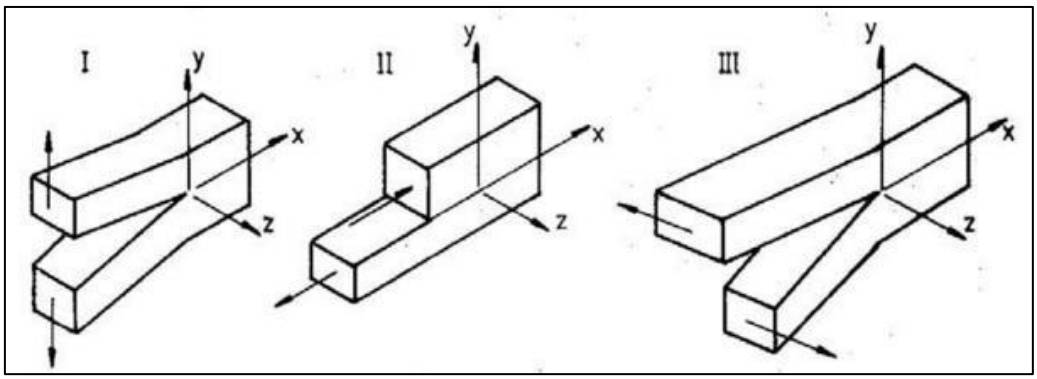

Figure 40 – Three basic modes of crack or delamination propagation (from STROHAECKER [75]).

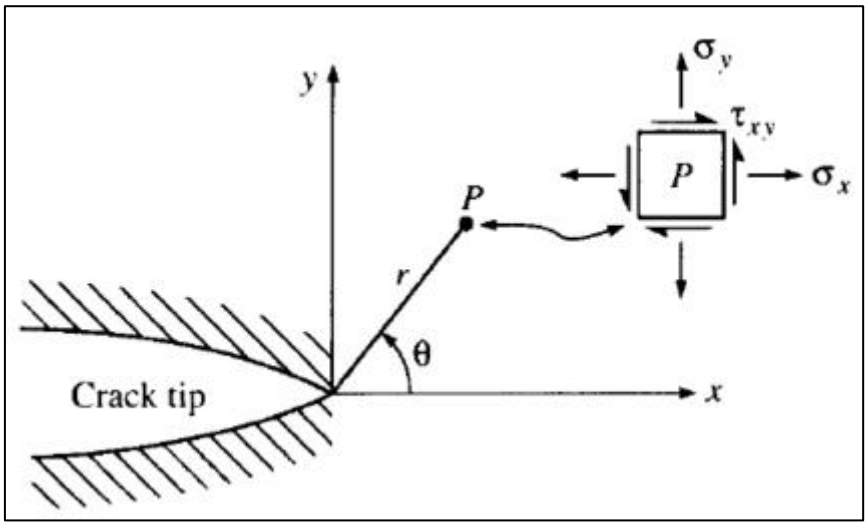

Figure 41 – Stress at crack tip in plane stress state (from GIBSON [25]).

In this way, it can be seen that the stress intensity at Equations (57), (58) and (59) depends on a parameter that is a function of σ and a, which is defined as the Stress Intensity Factor K_I, K_{II} and K_{III} for modes I, II and III, respectively.

In mode I:

$$K_I = \sigma\sqrt{\pi a} \tag{60}$$

Then, considering $f_i(\theta)$ trigonometric functions, in mode I, the stress field can be rewritten:

$$\sigma_x = \frac{K_I}{\sqrt{2\pi r}}\cos\theta\left(1 - \sin\frac{\theta}{2}\,\sin\frac{3\theta}{2}\right) \tag{61}$$

$$\sigma_y = \frac{K_I}{\sqrt{2\pi r}}\cos\theta\left(1 + \sin\frac{\theta}{2}\,\sin\frac{3\theta}{2}\right) \tag{62}$$

$$\tau_{xy} = \frac{K_I}{\sqrt{2\pi r}}\cos\frac{\theta}{2}\,\sin\frac{\theta}{2}\,\cos\frac{\theta}{2} \tag{63}$$

Analogously, in mode II:

$$\sigma_x = -\frac{K_{II}}{\sqrt{2\pi r}}\,\sin\frac{\theta}{2}\left(2 + \cos\frac{\theta}{2}\,\cos\frac{3\theta}{2}\right) \tag{64}$$

$$\sigma_y = \frac{K_{II}}{\sqrt{2\pi r}}\cos\frac{\theta}{2}\,\sin\frac{\theta}{2}\,\cos\frac{3\theta}{2} \tag{65}$$

$$\tau_{xy} = \frac{K_{II}}{\sqrt{2\pi r}}\cos\frac{\theta}{2}\left(1 - \sin\frac{\theta}{2}\,\sin\frac{3\theta}{2}\right) \tag{66}$$

where

$$K_{II} = \tau\sqrt{\pi a}$$
$$K_{III} = \tau\sqrt{\pi a} \tag{67}$$

For the principal stresses ($\sigma_{1,2}$):

$$\sigma_{1,2} = \frac{\sigma_x + \sigma_y}{2} \pm \sqrt{\left(\frac{\sigma_y - \sigma_x}{2}\right)^2 \tau_{xy}^2} \tag{68}$$

Then, for mode I, substituting Equations (61), (62) and (63) in Equation (68):

$$\sigma_1 = \frac{K_I}{\sqrt{2\pi r}}\cos\frac{\theta}{2}\left(1 + \sin\frac{\theta}{2}\right)$$
$$\sigma_2 = \frac{K_I}{\sqrt{2\pi r}}\cos\frac{\theta}{2}\left(1 - \sin\frac{\theta}{2}\right) \tag{69}$$

According to JANSSEN [72], there is a relationship between the Griffith Energy (G) and the Stress Intensity Factor (K), that is Equations (55) and (60), respectively:

$$K_I^2 = G_I E \tag{70}$$

Now, by analyzing the same Equations (55) and (60), it is noticed that there is also a value of K corresponding to a critical stress, σ_c. In this case, this factor is called the fracture toughness K_{Ic} of material. This value is determined experimentally, and has the same relation with σ and a:

$$K_{Ic} = \sigma_c \sqrt{\pi a} \tag{71}$$

Analogously, for Equation (70):

$$K_{Ic}^2 = G_{Ic} E \tag{72}$$

The solution of K_I considers an infinite plate with a through over centralized crack. For other plate and defect geometries, we have the relation:

$$K_I = Y\sigma\sqrt{\pi a}.f(a/W) \tag{73}$$

where W is the plate width, Y and a/W are obtained by stress analysis [73]. Thus, for example, cases with lateral notch or with elliptical surface crack, present different formulas for K_I.

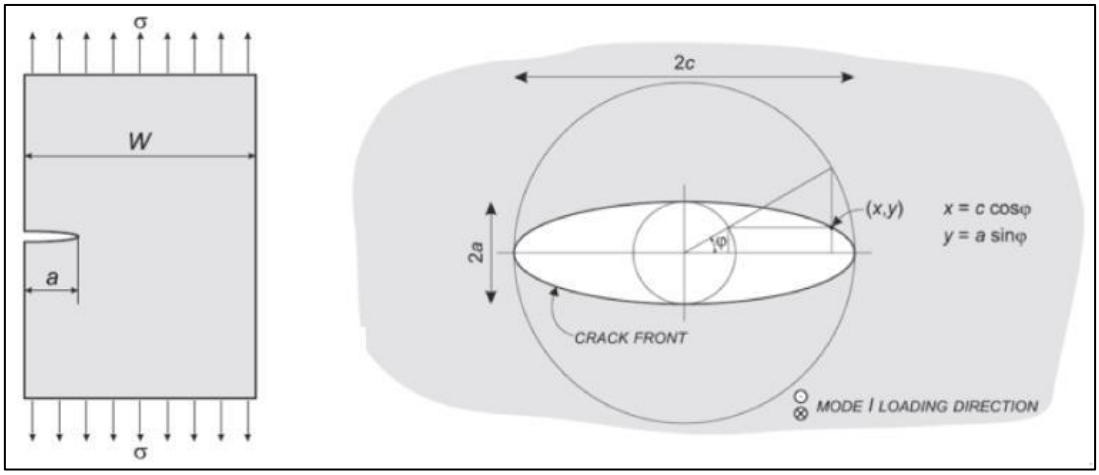

Figure 42 – Plate models with side or elliptical crack.

For plates with through all thickness crack at the corner, we have:

$$K_I = 1.12\sigma\sqrt{\pi a} \tag{74}$$

For surfaced elliptical cracks:

$$K_I = \frac{\sigma\sqrt{\pi a}}{\frac{3\pi}{8} + \frac{\pi}{8}\left(\frac{a}{c}\right)^2}.\left\{\sin^2\varphi + \left(\frac{a}{c}\right)^2\cos^2\varphi\right\}^{1/4} \tag{75}$$

Or, for semi elliptical shallow cracks:

$$K_I = \frac{1.12\sigma\sqrt{\pi a}}{\frac{3\pi}{8} + \frac{\pi}{8}\left(\frac{a}{c}\right)^2}.\left\{\sin^2\varphi + \left(\frac{a}{c}\right)^2\cos^2\varphi\right\}^{1/4} \tag{76}$$

In cases of multiple loadings, for example, in mode I, the stresses in the region near the crack tip are summed:

$$\left(\sigma_{ij}\right)_{Total} = \left(\sigma_{ij}\right)_1 + \left(\sigma_{ij}\right)_2 + \cdots = (K_I)_1.f_{ij}(r,\theta) + (K_I)_2.f_{ij}(r,\theta) + \cdots \tag{77}$$

Since $f(r,\theta)$ will be always the same:

$$\left(\sigma_{ij}\right)_{Total} = \{(K_I)_1 + (K_I)_2 + \cdots\}.f_{ij}(r,\theta) \tag{78}$$

or:

$$\left(\sigma_{ij}\right)_{Total} = (K_I)_{Total}.f_{ij}(r,\theta) \tag{79}$$

where $(K_I)_{Total} = (K_I)_1 + (K_I)_2 + \cdots$.

2.3.3. Debonding / pull-out fiber-matrix

Classical Lamination Theory does not study particularly fiber-matrix stresses, which may cause debonding between them. And, this failure mode, in some cases, is predominant in the composite.

The debonding between fiber and matrix is also known as fiber pull-out [34]. Through this theory, CHUA *et al.* [76] assumed that the fiber and matrix behave elastically, and the transfer of stresses occurs through the fiber-matrix interface considering a perfect adhesion, that is, without material flow or sliding between them.

It was recognized, then, that this type of failure is governed by five different variables: interfacial pressure (p), friction coefficient (μ) along the length of the fiber already

debonded, interface fracture energy (G), the "wet" length of the fiber, that is, the length of interaction with the matrix (L) and the fiber free length (l_f). CHUA *et al.* developed a relation for the tensile stress in the fiber (σ_f) at any point along its "wet" length:

$$\sigma_f = \sigma_{fe} \frac{\sinh \frac{n(L-x)}{r}}{\sinh\left(n\frac{L}{r}\right)} \tag{80}$$

where:

r = Fiber radius;

σ_{fe} = Fiber mean stress externally the matrix;

x = Position along the embedded length with a correlated stress.

The geometric terms are shown in Figure 43.

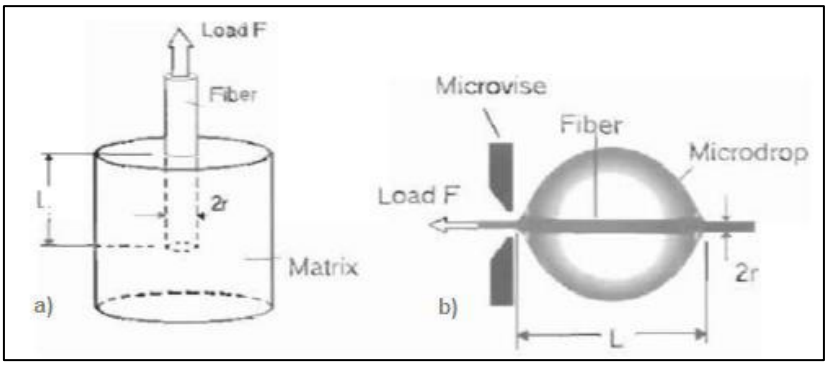

Figure 43 – Fiber pull-out illustration and micro adhesion technique presenting geometric parameters (from DILLARD e POCIUS [34]).

The dimensionless term n is defined by [34]:

$$n^2 = \frac{E_m}{E_f(1+\nu_m) ln\frac{R}{r}} \tag{81}$$

where E_f and E_m are the fiber and matrix tensile modulus, respectively, ν_m is the matrix Poisson's coefficient and R is the matrix external radius from Figure 43a. Then, the shear stress at the interface is calculated by the equilibrium of the forces applied on a fiber differential element of length dx:

$$\tau_i = \frac{r}{2}\frac{d\sigma_f}{dx} \tag{82}$$

In terms of the tensile stress in the fiber, we have:

$$\tau_i = n\sigma_{fe}\frac{\cosh\frac{n(L-x)}{r}}{2\sinh\left(n\frac{L}{r}\right)} \tag{83}$$

During fiber-matrix debonding, there are three possible paths to failure:

a) A Failure can occur when the maximum shear stress reaches the interface shear strength (τ_{iu}), which has its absolute maximum value at $x = 0$, that is, where the fiber leaves the matrix block. At this point, the debonding force (F_d) is:

$$F_d = 2\pi r^2\sigma_{fe} \tag{84}$$

From Equation (83), we have:

$$F_d = \frac{2\pi r^2\tau_{iu}\tanh\left(n\frac{L}{r}\right)}{n} \tag{85}$$

b) The failure at the interface can also occur if the shear strength of the interface (τ_{iu}) is reached by considering a constant distribution of the shear stress along the "wet" fiber if the hardening effects can be neglected. Then:

$$F_d = 2\pi rL\tau_{iu} \tag{86}$$

c) Another type of failure, more easily detected through experimental tests, is addressed to stress concentrators at the interface fiber-matrix. In this case, the rupture occurs catastrophically, that is, the debonding starts and propagates quickly along the interface. For this failure mode, the most recommended is that the analysis should be based on LEFM. Therefore, it can be assumed that the failure occurs when the fracture energy of the material interface (G_c) per unit of area is reached. Thus, considering the stored energy of the longitudinal strain (U_L) at the “wet” fiber and the stored energy of the matrix shear strain (U_m), we have the following relation [34]:

$$U_L + U_m = \frac{\pi r^3{\sigma_{fe}}^2\coth\left(n\frac{L}{r}\right)}{2nE_f} \tag{87}$$

Correlating the total strain energy with $2\pi rLG_c$, the debonding force will be:

$$P_d = 2\pi r \sqrt{E_f G_c r \left(n\frac{L}{r}\right) \tanh\left(n\frac{L}{r}\right)} \tag{88}$$

After the debonding, the pull-out process continues until the total fiber exit from the matrix. This step considers the variables interfacial pressure (p) and friction coefficient (μ) along the length of the debonded fiber. However, it will not be addressed in this work, since here the failure is already considered in the debonding initiation.

2.4. FINITE ELEMENT METHOD APPLIED TO LEFM

During section 2.3, Linear Elastic Fracture Mechanics (LEFM) was addressed analytically. The theory establishes in a consolidated way that the stresses, strains and energy release rate are function of stress intensity factors. However, analytical solutions available in literature are generally limited to problems with simple geometries and, often, with only one direction loading [77]. Therefore, for validating more complex studies, it is important to use additional methods such as numerical modeling and small or real scale tests. Since performing tests is time consuming usually costly, it should be reduced and optimized. Thus, the numerical analysis technique, for example the Finite Element Method (FEM), becomes a good interim option to verify an analytical development. It should be noted, however, that numerical methods also have uncertainties inherent to the modeling, so performing the tests, even optimized, remains highly recommended for final consolidation of the study.

The use of FEM has widely increased in industries for LEFM analysis [77]. Due to the continuous improvement of software tools, many complex geometries and loading problems are now efficiently solved. Furthermore, FEM can provide good interface with users due to direct physical analogy that is established between the real system and the finite element mesh model [78].

The main FEM used for composite fracture mechanics are Cohesive Zone Model (CZM) and Virtual Crack Closure Technique (VCCT). Nevertheless, according to KREGTING [79] and KHORAMISHAD *et al.* [80], CZM method can focus on surfaces debonding initiation and propagation, and applying mixed failure modes (I, II and III) while VCCT technique considers the failure of the composite immediately after loss of adhesion, and it is mostly applied for failure mode I.

2.4.1. Virtual crack closure technique (VCCT)

VCCT technique was first presented in 1977 by RYBICKI *et al.* [81]. It is a commonly used method for delamination analysis in composite materials. According to KRUEGER [82], the theory assumes that the energy required to separate the surfaces is the same energy required to close them. In this context, the analysis is linear elastic and the material may be isotropic, orthotropic or anisotropic.

To get to the VCCT method, it is important to go through the "Two Step Crack Closure Technique" [82]. This method is presented in Figure 44 and the work (ΔW) required to close the crack has the following relation

$$\Delta W = \frac{1}{2}\{X_{1l}\Delta u_{2l} + Z_{1l}\Delta w_{2l}\} \tag{89}$$

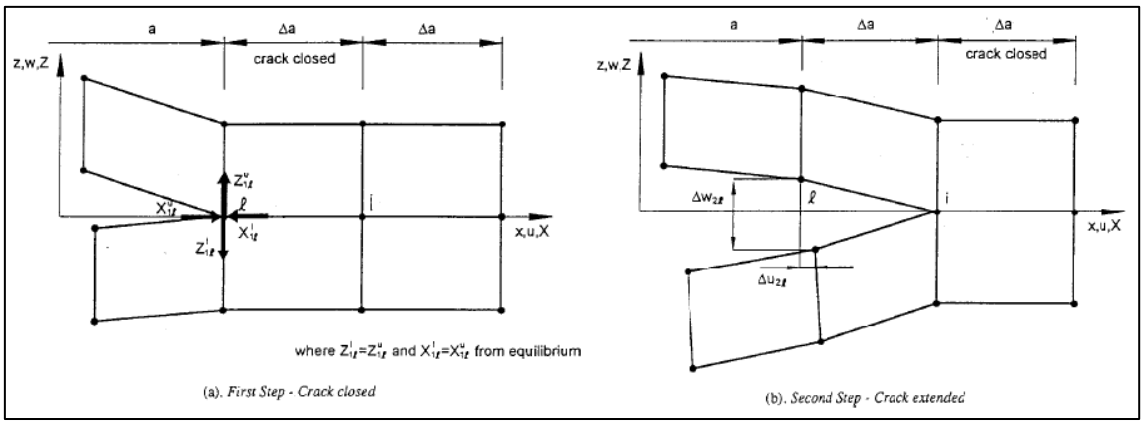

Figure 44 – Crack closure technique in two steps, a) Closed crack, b) Opened crack (from KRUEGER [82]).

where a is the initial crack length, X_{1l} and Z_{1l} are the shear and opening forces, respectively, for the nodal point l be kept closed (first step). Δa represents how much the crack opens in the second step, and, Δu_{2l} and Δw_{2l} are the displacements due to the differential of the shear and opening forces.

Index 1 and 2 refer respectively to the first and second steps.

The adaptation of this theory, called VCCT, is based on the same assumptions, however, it is also assumed that the opening of the crack (Δa) from $a + \Delta a$ at "i" node to $a + 2\Delta a$ at "k" node does not significantly change at the crack end as shown in Figure 45.

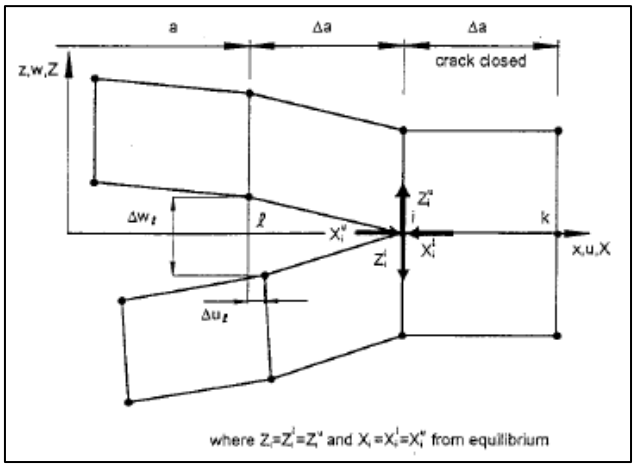

Figure 45 – Modified virtual crack closure technique (only one VCCT step) (from KRUEGER [82]).

Thus, considering the VCCT, the work (ΔW) required to close the crack along one side of the element will be

$$\Delta W = \frac{1}{2}\{X_i \Delta u_l + Z_i \Delta w_l\} \tag{90}$$

where X_i and Z_i are the shear and opening forces, respectively, for i node, Δu_l and Δw_l are the displacements due to the differential of the shear and opening forces in node l.

Then, the elastic energy release rate, $G_I \; e \; G_{II}$, can be calculated for a four- or eight-node element as shown in Figure 46 and following the following relationships:

For four-node elements:

$$G_I = \frac{1}{2\Delta a} Z_i (w_l - w_{l*})$$
$$G_{II} = \frac{1}{2\Delta a} X_i (u_l - u_{l*}) \tag{91}$$

For eight-node elements:

$$G_I = \frac{1}{2\Delta a}\left[Z_i (w_l - w_{l*}) + Z_j (w_m - w_{m*})\right]$$
$$G_{II} = \frac{1}{2\Delta a}\left[X_i (u_l - u_{l*}) + X_j (u_m - u_{m*})\right] \tag{92}$$

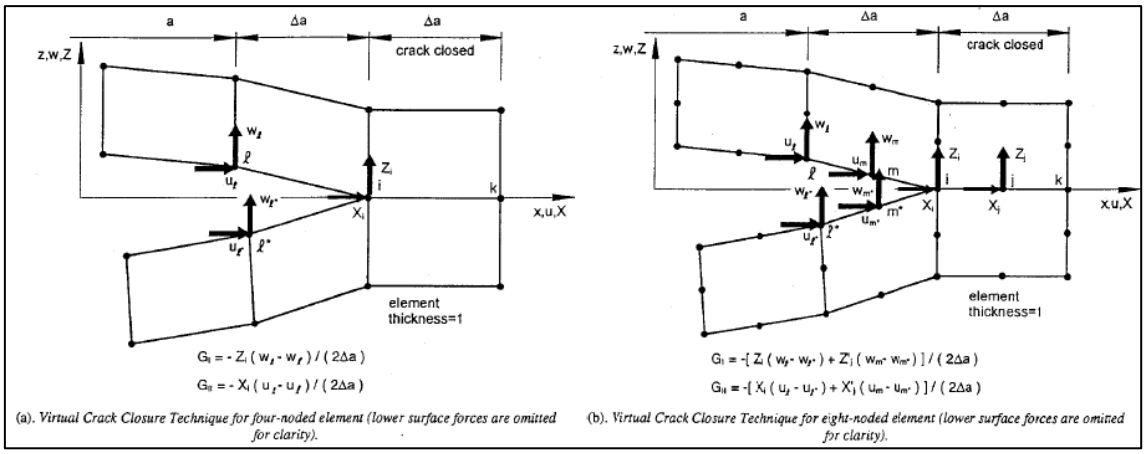

Figure 46 – VCCT for 2D solid elements, a) Four nodes elements, b) Eight nodes elements (from KRUEGER [82]).

The equations are also applicable to triangular parabolic elements if used at the crack tip. RAJU [83] and BARSOUM [84] proposed the use of special elements, or singular elements, at the end of the two-dimensional crack, as shown in Figure 47. Based on the node location at $\xi = 0.0, 0.25\ and\ 1.0$, these elements simulate with accuracy by incorporating a singularity of type $r^{-1/2}$ for the calculation of the stress intensity factor at the crack tip, where r is defined in section 2.4.2. The triangular elements can be obtained by dividing the rectangular element. According to BARSOUM, the use of these elements with symmetrical contours tends to show a high degree of convergence with the analytical solutions.

Therefore, rearranging Equations (92) using the singular elements of Figure 47, we have:

$$G_I = \frac{1}{2\Delta a}\{Z_i[t_{11}(w_l - w_{l*}) + t_{12}(w_m - w_{m*})] + Z_j[t_{21}(w_l - w_{l*}) + t_{22}(w_m - w_{m*})]\}$$

$$G_{II} = \frac{1}{2\Delta a}\{X_i[t_{11}(u_l - u_{l*}) + t_{12}(u_m - u_{m*})] + X_j[t_{21}(u_l - u_{l*}) + t_{22}(u_m - u_{m*})]\} \quad (93)$$

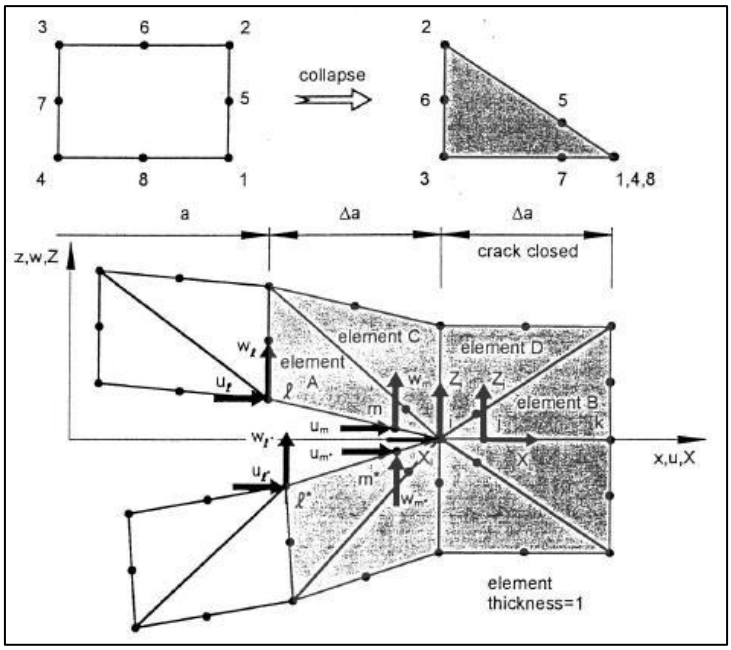

Figure 47 – VCCT with singular elements at crack tip from two-dimensional model (from KRUEGER [82]).

2.4.2. Cohesive zone model (CZM)

CZM predicts a material behavior of an interface between layers, from elastic deformation, to softening and damage accumulation, ending in eventual debonding [85]. It represents well the equation (88), which predicts the total failure the fracture energy of the material interface (G_c) per unit of area is reached.

In FEM, the interface is modeled with elements that have no thickness but provide the bonding between the two layers. A common CZM behavior is the bilinear debonding law shown Figure 48. The initial slope represents the linear elastic material behavior of the interface. When the maximum shear or tangential stress is achieved, the damage (d) is initiated. Equation (85), for instance, would predict the failure at this point. Then, the damage evolution and interface displacement are represented by the downward slope. The debonding failure is, therefore, achieved when the system reaches the maximum displacement and debonding energy (G_c).

Cohesive Zone debonding allows three modes of separation: Mode I debonding for normal separation, Mode II debonding for tangential separation, Mixed mode debonding for normal and tangential. The properties required are the maximum normal and/or tangential contact stress and the fracture energy for normal and/or tangential separation.

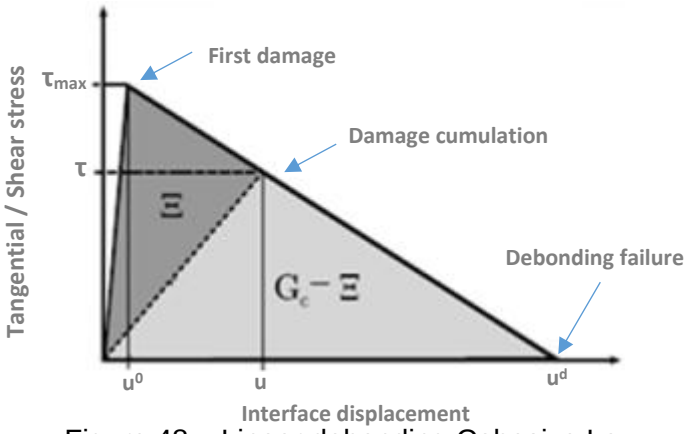

Figure 48 – Linear debonding Cohesive Law.

This method is the most representative of the problem of this work, therefore it was the chosen theory used for developing the FEM, which is better described in section 5.3. Nevertheless, it is important noting that it can exhibit convergence difficulties already noticed by other authors [86, 87]. That is why CZM for FEM usually enables the use of an artificial damping coefficient that is applied to stabilize the numerical solution, typically based on a procedure called viscous regularization. However, the larger is this value the more resistant and non-conservative the system will be. Therefore, according to BORELLI *et al.* [86], damping coefficient should not be greater than 0.1 times the FEM time increment (1s) to guarantee reliable results.

2.4.3. Mesh of pre-stablished defect

One of the most important parameters to ensure an FEM analysis with reasonable results is the mesh of the model. It is composed by the continuous perimeters of the finite domain, called elements, which have points in their contours to connect them to each other, called nodes. According to SAKAKIBARA [88], FEM solutions for LEFM using standard isoparametric elements tend to present errors between 5 and 10%. Even increasing the refinement of the mesh, the results may be distorted near the crack tip.

BARSOUM [84] was one of the researchers who found that moving the mean node of a quadrilateral element with eight nodes to the position of a quarter of the edge of the element, the desired variation of strains can be calculated along the radius r inside the element that has its origin in the crack tip. This new singular element is called the Quarter Point Element (QPE) [88]. As shown in Figure 49, nodes 6 and 8 can be moved to points 3 and 4, respectively, and points 3, 4 and 7 can be allocated in the same position. Thus, as the midpoints are moved up to a quarter of the edge, the global coordinate system becomes similar to the $1/\sqrt{r}$. It is important to note that a small number of QPEs involving the crack tip can result in a model with inadequate circumferential displacements. On the

other hand, excessive amounts of QPEs generate very small angles between them and generate errors due to the distortion of the elements. Therefore, the use of 6 to 8 QPEs is considered reasonable.

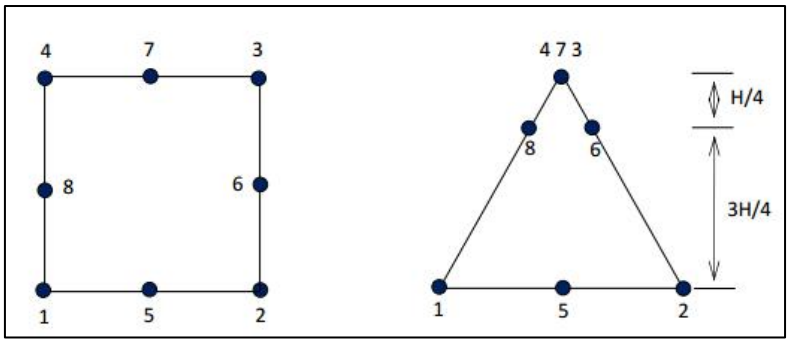

Figure 49 – Isoparametric quadrilateral element and quarter point QPE (from SAKAKIBARA [88]).

According to ANTUNES [89], the elements around the QPEs are also very important to improve the accuracy of the calculations of stress intensity factors. They are the transition elements, which follow the same concept of average node displacement with regards to the following relationship [88]

$$\beta L = \frac{L + 2\sqrt{L} + 1}{4} \tag{94}$$

where, in this case, the length of the QPE is 1 and L is the distance from the crack tip to the outer node of the transition element. Figure 50 shows a transition element with a QPE, and Figure 51 shows the final configuration of the mesh of an element having a crack with length a using QPEs, transition elements and rectangular isoparametric elements.

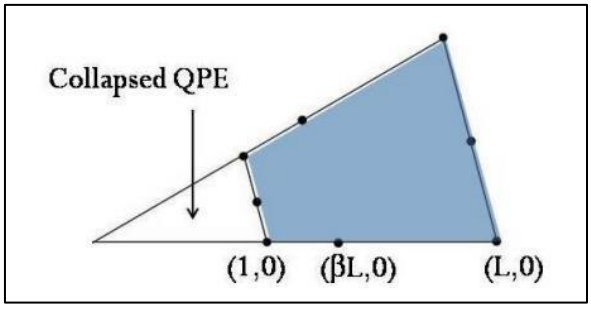

Figure 50 – Transition element (from SAKAKIBARA [88]).

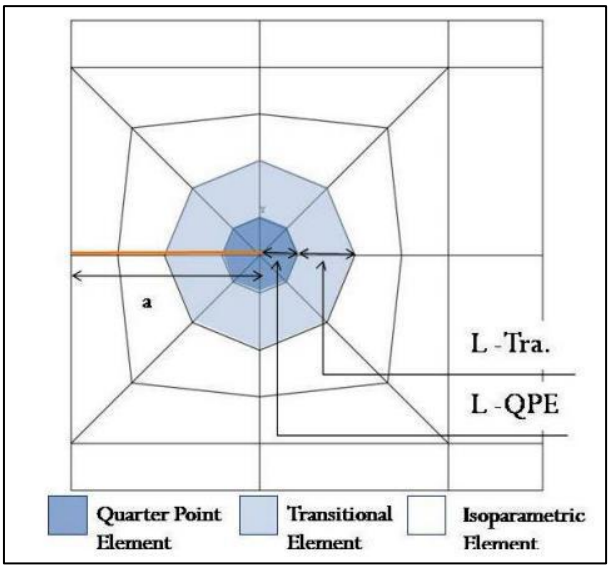

Figure 51 – Final crack mesh configuration (from SAKAKIBARA [88]).

Then, applying the mesh theory of QPEs and transition elements in the CZM technique presented in section 2.4.2, the FEM analysis tends to provide reliable results for the values of the release rate of elastic energy, or Griffith Energy G, and the stress intensity factor k. Therefore, this methodology can be adopted to validate possible analytical models developed for LEFM problems.

It is worth remembering that the tests are part of the third pillar of this work, which are performed to adequately characterize the properties and limits of the materials, feed the analytical model and help in the calibration of the FEM model. Some test options are presented in the next section.

2.5. SMALL SCALE TESTS

2.5.1. Tension as per ASTM D638

This test method predicts the assessment of mechanical tensile properties of reinforced and non-reinforced polymers from Dumbbell or Dog Bone shaped samples [90]. Basically, it is a test in which a sample is tensioned at a constant displacement rate.

The main properties acquired in the test are tensile modulus, yield limit, strain and ultimate tensile stress. However, for isotropic and homogeneous materials, the Poisson's coefficient can also be measured using a transverse strain gage.

For an isotropic material, it is necessary to test at least five samples to reduce the dispersion of results. For anisotropic, ten, with five in the longitudinal direction and five

in the transverse direction. Samples that fail due to some defect in the material or out of the thin section of the sample should be discarded and repeated.

Figure 52 presents a typical specimen of the test, of which dimensions are properly described in the standard and vary according to the characteristics of the material. Dumbbell-Shaped samples have five types. Type I is the most suitable, and should be used whenever samples can reach up to 7mm thick; Type II should be used if material rupture does not occur in the thinnest section of type I; Type III is for materials with thicknesses greater than 7 and less than 14mm; Type IV is recommended when a direct comparison is required between materials with different stiffness; Type V is limited to materials having thicknesses equal to or smaller than 4mm, or where a large number of specimens will be exposed in a limited space.

The speed of the test to be respected depends directly on the type of specimen and whether the material is rigid, semi-rigid or non-rigid. Rates range from 1 to 500 mm/min.

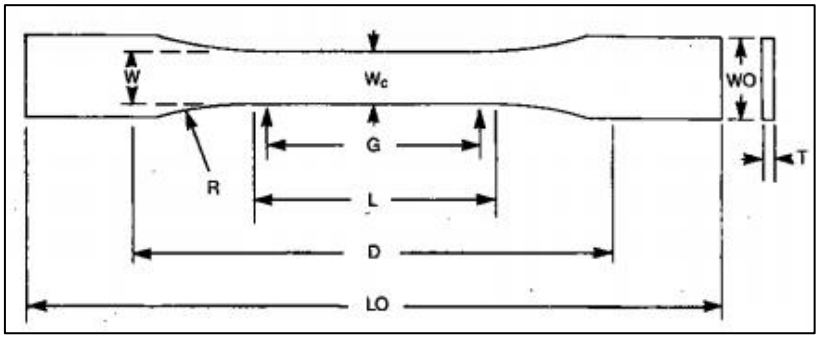

Figure 52 – Typical specimen for tensile test [90].

2.5.2. Compression as per ASTM D695

This test method covers the determination of the mechanical properties in compression of polymers and composites in general [91]. Basically, it is a test in which a specimen, generally cylindrical, is compressed at a constant and relatively low rate (1,3 mm/min).

The main properties acquired in the test are compressive modulus, yield limit, strain and compressive strength.

For an isotropic material, it is necessary to test at least five specimens to reduce the dispersion of results. For anisotropic, ten, with five in the longitudinal direction and five in the transverse direction. It is also recommended that twenty percent more specimens be considered as spares in case there is premature failure of the specimen due to some defect or other unforeseen during the test.

Figure 53 shows a schematic of the test, as well as the commonly used bench and its specimen.

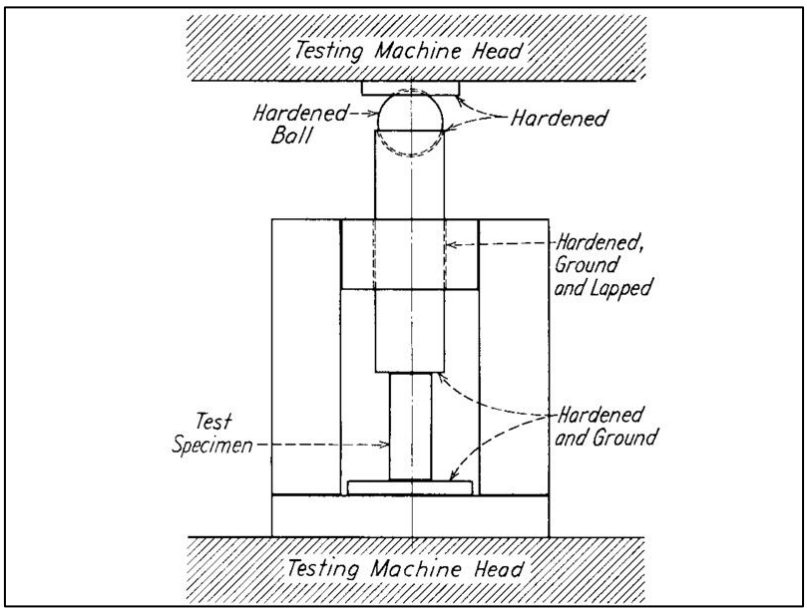

Figure 53 – Bench illustration of compression test [91].

2.5.3. Fracture toughness K_{1c} as per ASTM E399 and ISO 13586

This method mainly determines the fracture toughness (K_{Ic}) of the material under predominantly linear elastic condition in the plane strain state using a specimen with a preformed crack [92].

Specimens can have different configuration such as: Bend SE(B), Compact C(T), Disk-Shaped Compact DC(T), Arc-Shaped Tension A(T) and Arc-Shaped Bend A(B). The symbols B and T mean that the tests are performed by flexing or tension, respectively.

Figure 54 shows a specimen of type C(T) with its centralized crack and two holes for attachment to a tensile test bench.

The test predicts the application of a loading while measuring the Crack-Mouth Opening Displacement (CMOD). Thus, the value obtained K_{Ic} is used to reach the relationship between the ultimate or failure stress and the crack size for a given material when subjected to a load.

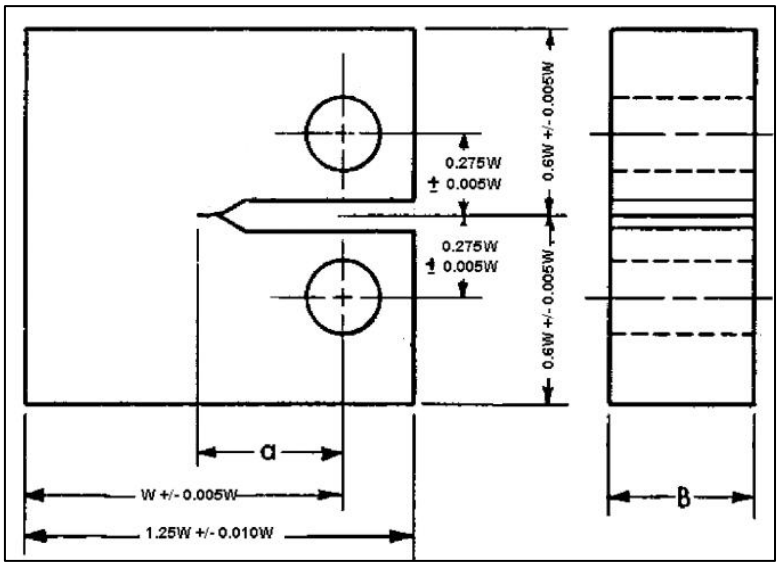

Figure 54 – Compact tensile specimen *C(T)* for fracture toughness test [93].

The size of the specimen required for the test results to be valid depends on ratio between toughness and squared yield of material, as described in Equation (95). Furthermore, the size of the crack, angles, roughness and dimensional and geometric tolerances are specified by the standard. Other devices, such as clip gage, are used to monitor the crack opening.

$$W - a \geq 2{,}5\left(\frac{K_{Ic}}{\sigma_{YS}}\right) \tag{95}$$

where:

- W is the width of the specimen, considered to the center of the holes where the loading is applied;
- a is the crack size, considered from the center of the holes where the loading is applied;
- σ_{YS} is the yield limit in the stress-strain curve.

It is recommended to perform the test with at least three specimens for each case.

For the quasi-static conventional test, the load should be applied at a stress intensity factor growth rate between 0,55 and 2,75 MPa.m$^{0.5}$/s during the initial elastic displacement.

2.5.4. Single lap shear as per ASTM D3165

This test method determines the shear strength of adhesives and is based on ASTM D3165 [94]. As described in section 2.2.3, the adhesive properties are very dependent on their thickness, wettability and the quality of the interface with the substrate. Therefore, the reproducibility of the values reached in the test depends directly on these parameters, so the preparation of the specimens must be done with a good control.

For the shear of the specimen, it is tensioned on a bench at its ends. The type of specimen is illustrated in Figure 55 of specimens possible to perform the double shear test, which are presented. The standard suggests the dimensions that must be followed depending on the material tested, however the most important is that the geometries of the system ensure that the failure will always occur on the adhesive or cohesive interface.

At least five specimens are recommended to minimize dispersion of results. Tests that fail due to an undesirable defect, be it in the adhesive, substrate or interface, should be repeated and the specimens discarded. A recommended speed is 1mm/min.

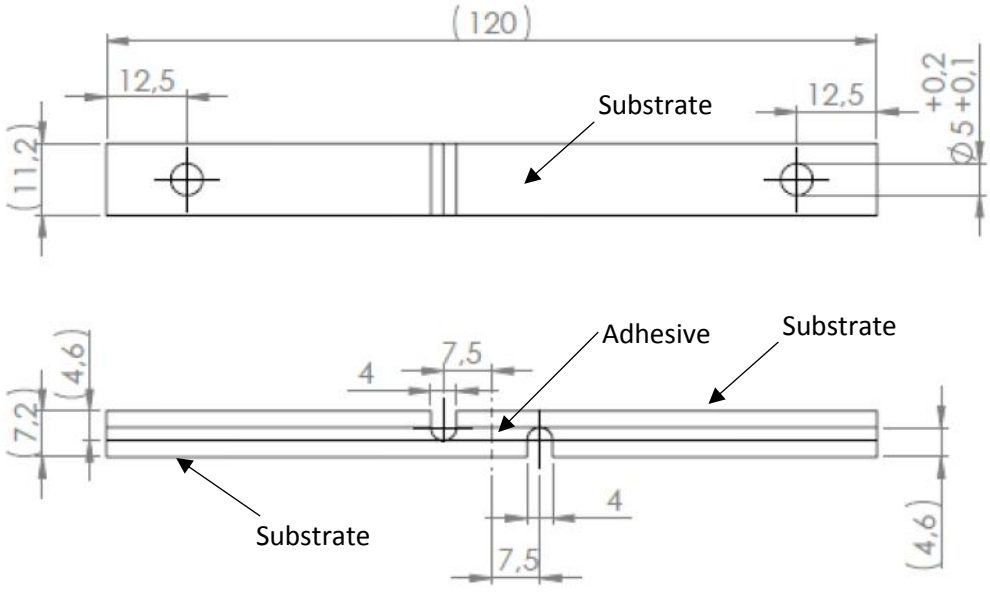

Figure 55 – Specimen for single lap shear test.

2.5.5. Double cantilever bean as per ASTM D6671

This test method describes the determination of interlaminar fracture toughness, G_c, of continuous fiber-reinforced composite materials at various Mode I to Mode II loading ratios using the Mixed-Mode Bending (MMB) Test [95].

A properly calibrated test machine is used which can be operated in a displacement control mode with a constant displacement rate in the range of 0.5 to 5.0 mm/min. The method can be used to determine the following delamination toughness values: Delamination Initiation and Propagation.

At least five specimens are recommended to minimize dispersion of results. Tests that fail due to an undesirable defect, be it in the adhesive, substrate or interface, should be repeated and the specimens discarded.

Some information about the MMB apparatus, specimens and variables are presented in the following figures.

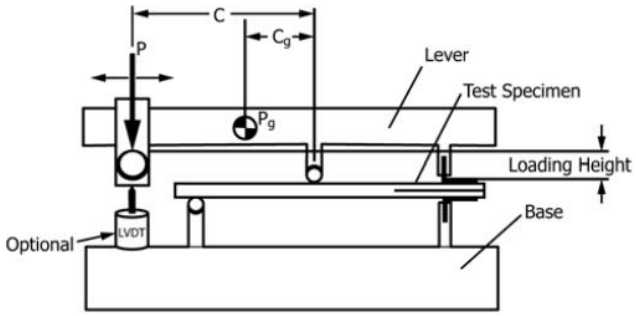

Figure 56 – MMB apparatus.

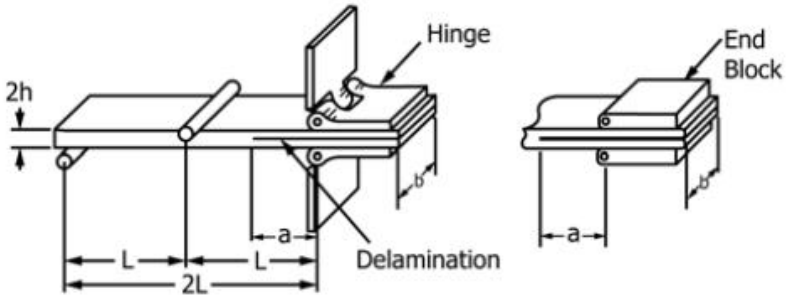

Figure 57 – MMB specimen and variables.

Chapter 3 – Objective

The objective of this work is to propose a composite system based on a toughened epoxy resin for anchoring the CFAs of flexible risers. Some different fillers, in terms of morphology, aspect ratio, concentration and functionalization, are studied to increase adhesion with CFA interface, and epoxy mechanical properties such as modulus and toughness, and therefore maximize pull-out resistance of the anchoring system.

It also aims to develop an analytical model of the anchoring mechanism, verified by finite element analysis, to evaluate the sensitivity of the system to the variation of these epoxy mechanical and adhesion properties.

Chapter 4 – State of art

4.1. CFA-EPOXY ANCHORING COMPOSITE SYSTEM

In the subsea oil and gas segment, a common technique used for anchoring the tensile armors of flexible riser within the end fitting is through an embedded epoxy resin, as presented in section 2.1.3, since it provides good chemical resistance and stable mechanical performance. When these armors are made by composite, that is CFAs, the interface with the epoxy is considered as bonded.

For many applications, the adhesion between structures for efficiently transferring static and dynamic loads is a difficult problem to solve, especially for products which operate for long periods of time under extreme environments such as in contact with corrosive fluid and high temperature. Therefore, one of the great challenges of risers with CFA solution is to ensure its anchoring in the end fittings throughout life time. And, as seen in the previous sections, there are several parameters inherent to the interface between the CFAs and the epoxy resin, as well as their mechanical properties, that directly impact the performance of the system.

Thus, this work proposes a toughened composite system for anchoring the CFAs, in which the epoxy resin within the end fitting behaves as matrix and the CFAs as main reinforcement.

Ratifying what was described in section 2.1.2, CFA is an orthotropic composite ply with unidirectional carbon fibers, embedded in an epoxy matrix, aligned in the direction of its main axis [2], see Figure 58a). Then, by analyzing Figure 5 from section 2.1, the flexible riser body is formed by one or two pairs of a layer with CFAs independent to each other and laid following an angle from the riser main axis. It is important to highlight that the pair exhibits anti-symmetry at this angle, that is, while one layer arranged at an angle θ, the second is at $-\theta$.

When the CFAs get in the end fitting, they become attached to each other by an embedded epoxy resin. Therefore, since the CFAs are bonded to the epoxy, it is proposed that a new composite is formed where the CFA acts as reinforcement and the epoxy as matrix. That means epoxy's mechanical properties influence directly on the performance of the anchoring system, as presented in sections 2.2 and 2.3. Thus, considering the CFA layers placed at $\pm\theta$, not yet in helicoidal but in plate shape, it is

possible to make analogy between Figure 33 and Figure 34 from section 2.2.7, and Figure 58b), which have laminated composites with their angled fibers.

Then, by extrapolating to helicoidal shape, it could be concluded that the two or four CFA layers bonded to each other within the end fitting are basically a cylindrical laminate composite with two or four plies.

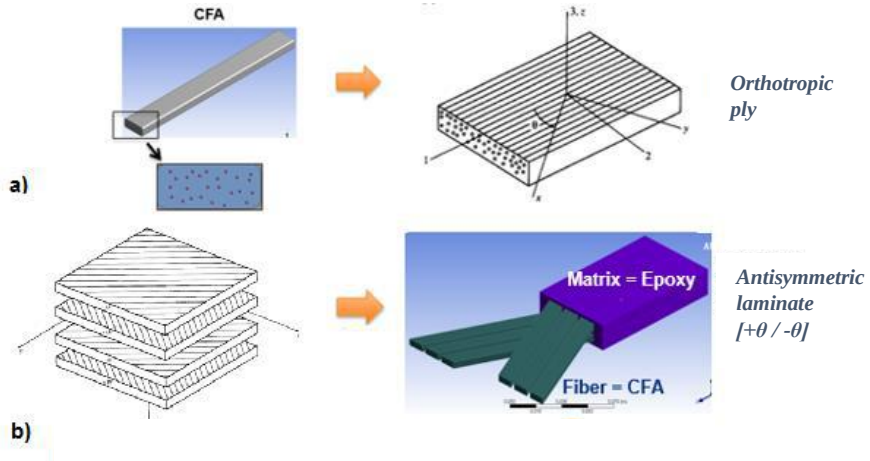

Figure 58 – Similarity between: a) CFA and orthotropic ply model, b) Antisymmetric laminate [+θ/-θ] ° and an antisymmetric laminate where fibers are CFASs and matrix is the epoxy resin.

The main effort withstood by the anchoring system and transferred to the EF body is the tensile loads from the riser body through the CFAs in their axis direction. Therefore, the shearing between CFAs and epoxy is predominant in the mechanism. Thus, similarly to section 2.3.3, CFA debonding (or pull-out) failure mode becomes the most likely phenomenon that shall be investigated and prevented.

Figure 59 shows a cross section of EF with the CFAs anchoring chamber. While Figure 59a) presents a complete EF example, Figure 59b) detaches the anchoring chamber with the epoxy matrix and a representative embedded CFA. Finally, Figure 59c) illustrates a single straight CFA-epoxy system, which was the model considered for pull-out study.

It is important to note that this study does not use any specific anchoring shape, such as opening the armor layers (changing layer diameter) like examples presented in section 2.1.3, since it depends on each supplier's EF design. That means the CFAs are considered organized as they arrive from the body of the riser, with same layer diameter. And embedded epoxy is developed having constant thickness along the anchoring.

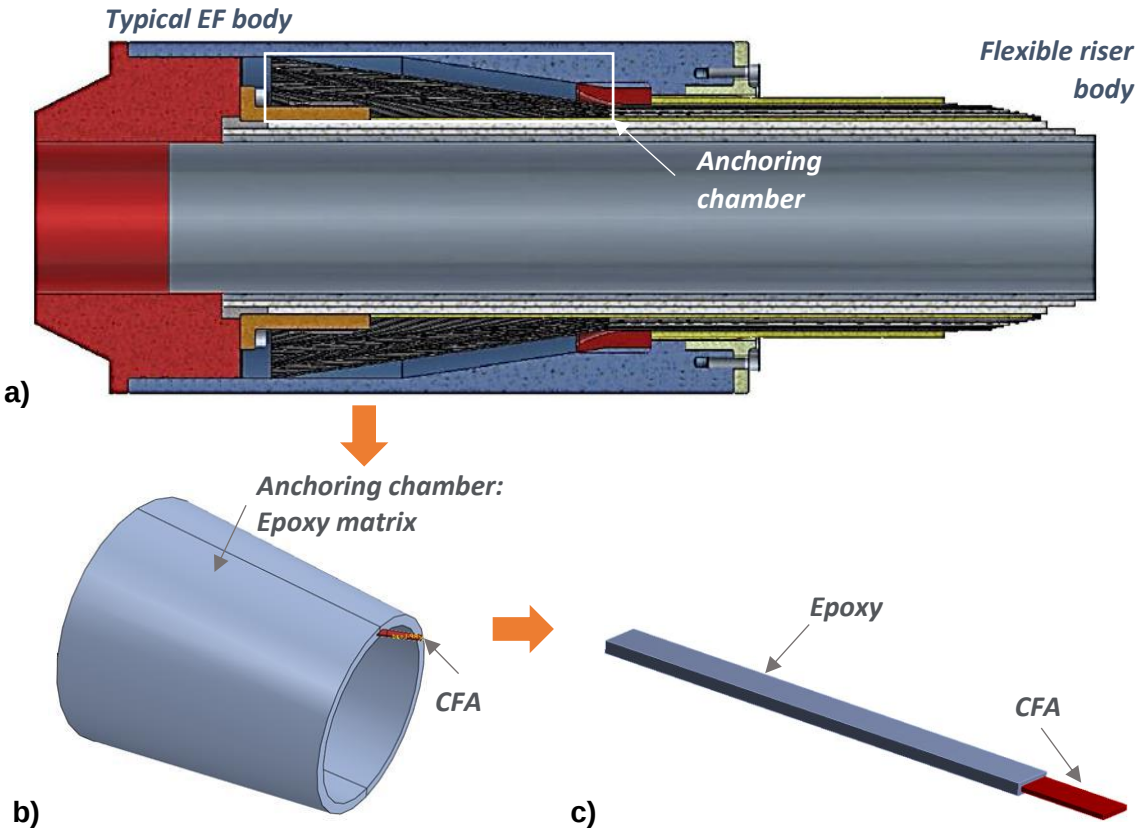

Figure 59 – Cross section example of a riser EF with CFA anchoring chamber: a) Complete EF, b) Anchoring chamber with epoxy matrix and a representative CFA, c) Single straight CFA-epoxy system considered for pull-out study.

During the entire work, the CFA is considered a constant parameter with its pre-established properties, while the epoxy and interface properties are variables studied and with sought improvement of the model.

4.2. TOUGHENING CFA-EPOXY FOR IMPROVING ANCHORING SYSTEM

According to section 2.3.3 and by freezing CFA mechanical properties, the better the epoxy properties, such as adhesion, modulus and toughness, the more resistant the anchoring system. Therefore, this research proposes adding fillers to the epoxy, such as short fibers, particles or nanotubes presented in section 2.2.4, seeking improvement of mechanical properties and adhesion. The choice of the filler and the characterization methods used in this study is described in section 5.4.

Finally, Figure 60 presents the final composite for improving the anchoring of CFAs of flexible risers with some examples of fillers studied as a potential solution. It is formed by the CFA as main reinforcement, with orthotropic properties and unidirectional aligned carbon fibers, and the filler toughened epoxy as matrix with isotropic linear elastic properties.

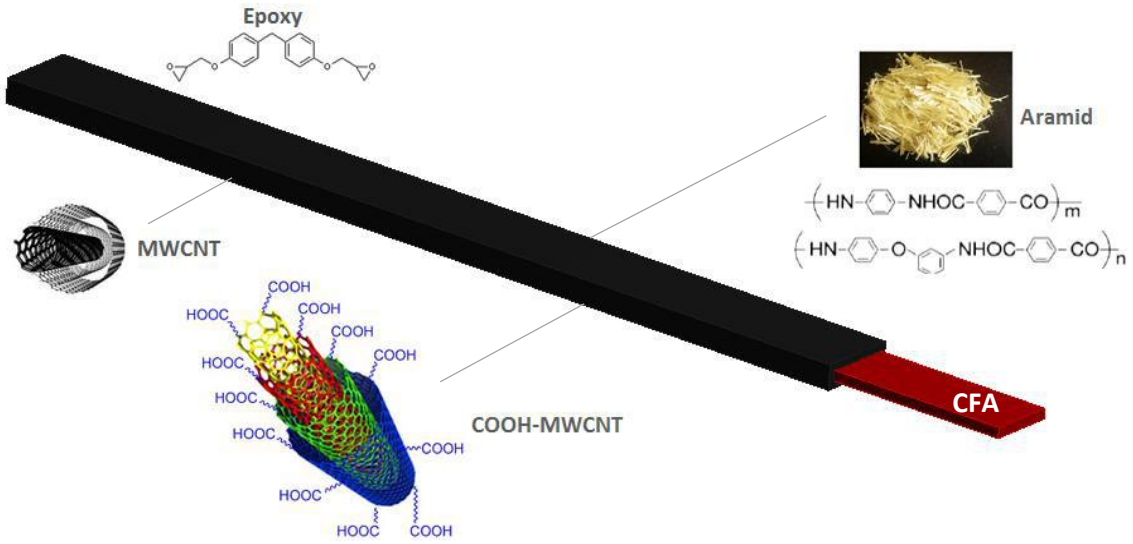

Figure 60 – Illustration of proposed toughened CFA-epoxy composite with some examples of fillers.

To evaluate the gain of mechanical and adhesive properties by toughening the epoxy matrix with a chosen filler, different types and concentrations are studied and small-scale tests are performed. Details of whole methodology is presented in the following section.

A pull-out analytical method is proposed and verified by FEM for evaluating the gain of anchoring system by improving the matrix and interface with CFA. The results from tests with toughened epoxy are applied in the analytical model to compare its pull-out resistance to a neat epoxy matrix anchoring system.

Chapter 5 – Methodology of research

5.1. GENERAL SCOPE

The main steps planned for the research were: Conception of CFA-epoxy composite anchoring system considering the CFAs as main reinforcement and epoxy as matrix of a cylindric laminate composite; Development of the analytical failure pull-out model to demonstrate the dependency of the CFA anchoring behavior on epoxy mechanical and adhesion properties, and to propose a new CFA pull-out failure model; Development of a FEM to verify the accuracy of the proposed analytical model; Evaluation of potential filler for toughening the epoxy; Study of a toughened epoxy solution with the chosen filler and concentration; Carrying out epoxy and CFA-epoxy mechanical experiments and fracture analysis with Neat and toughened epoxies; Filler investigation by analyzing morphology, verifying aspect ratio and functionalization to correlate with the mechanical experiments results; Then, evaluation of the gain of CFA-epoxy anchoring resistance by applying properties of toughened epoxy on the pull-out failure analytical model.

The following flowchart summarizes the main steps of the research.

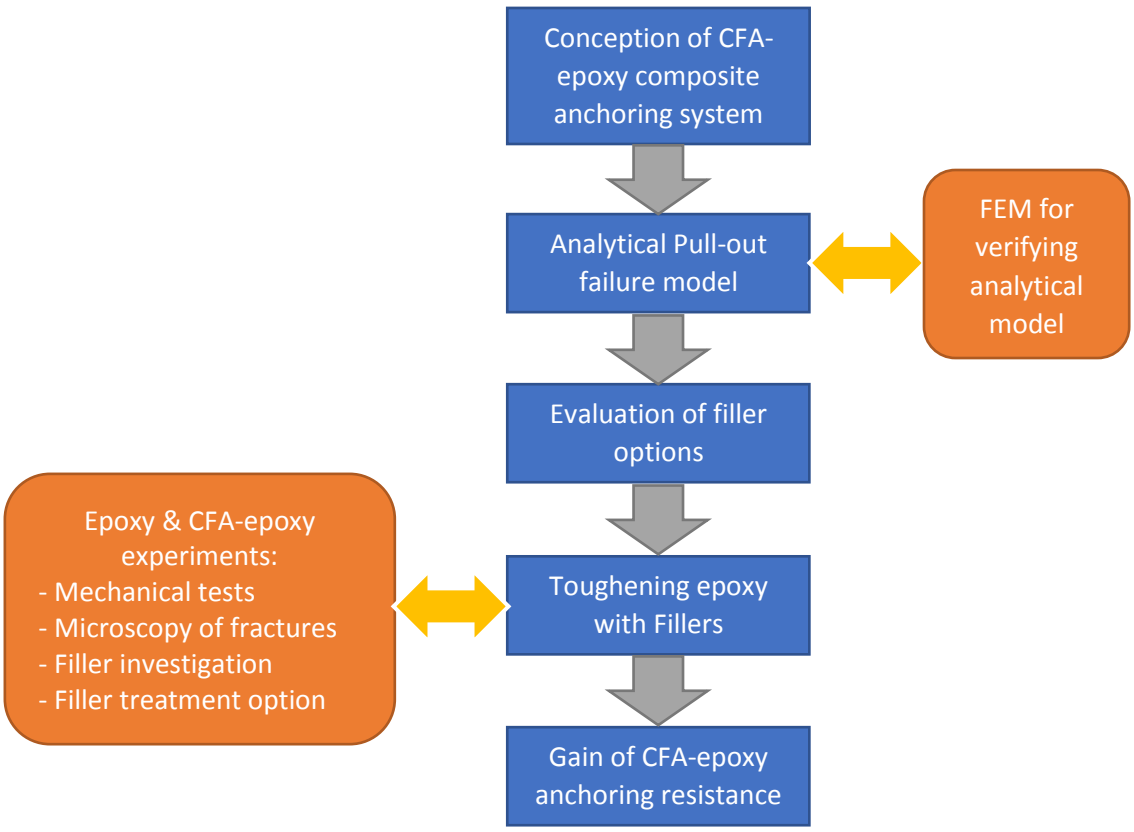

Figure 61 – Flowchart of main research steps.

5.2. ANALYTICAL MODEL

Figure 62 summarizes the parameters considered during the development of the analytical model. The external forces, the mechanical properties of the CFA and the geometric information of the flexible riser were constants of the model. The variables that feed the method and were studied were the mechanical properties of the epoxy matrix and its adhesion to CFAs.

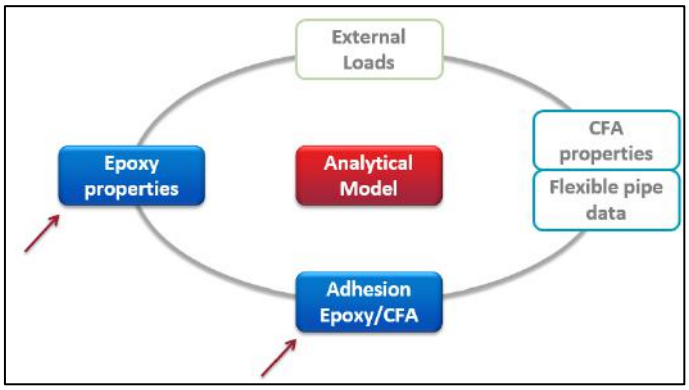

Figure 62 – Needed parameters for developing of analytical model.

5.2.1. Anchoring composite

For evaluation of the system, the study started by using micromechanics presented in section 2.2.6 to reach the properties of the CFA-epoxy system, then defining the properties of each layer, that is each ply, anchored in the EF. At this first step, it is evaluated in the main axis of the ply (1-2), that is, in CFAs direction, as shown in Figure 63.

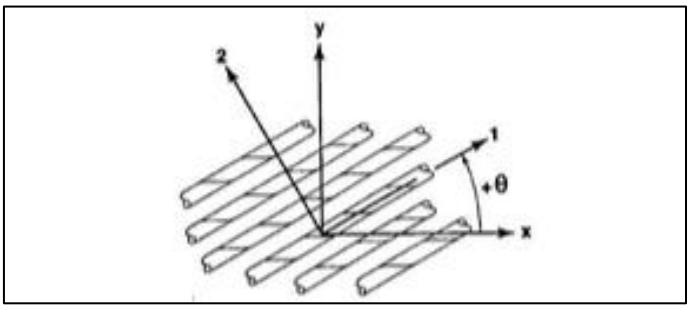

Figure 63 – Rotation of principal axis from x-y axis [26].

Then, considering a flexible riser with one pair of CFA layers, at ply 1 (internal layer), and using equation (3), we have:

$$v_{CFA_1} + v_{E_1} + v_v = 1 \tag{96}$$

$$v_{E_1} = 1 - v_{CFA_1} - v_v \tag{97}$$

where v_{E_1} and v_{CFA_1} are the volume fractions of epoxy and CFA, respectively, in ply 1 and v_v the fraction of internal voids already described in section 2.2.6. It is important to note that, in this case, the volume fractions are functions of the riser configuration. Thus, the variables "CFA cross-section", "number of CFAs per ply" and "internal and external ply diameters" define v_{E_1} and v_{CFA_1}.

Therefore, from equations (15) and (16):

$$E_{1_{Lam1}} = E_{1_{CFA}} v_{CFA_1} + E_E\left(1 - v_{CFA_1} - v_v\right) \tag{98}$$

$$\nu_{12_{Lam1}} = \nu_{12_{CFA}} v_{CFA_1} + \nu_E\left(1 - v_{CFA_1} - v_v\right) \tag{99}$$

where:

$E_{1_{Lam1}}$ = Longitudinal modulus of inner layer (ply 1);

$E_{1_{CFA}}$ = Longitudinal modulus of CFA;

E_E = Epoxy tensile modulus;

$\nu_{12_{Lam1}}$ = Poisson*'s* coefficient of inner layer (ply 1);

$\nu_{12_{CFA}}$ = Poisson*'s* coefficient of CFA;

ν_E = Poisson*'s* coefficient of epoxy;

Note that the properties of the epoxy do not have indices in equations (98) and (99), because the epoxy matrix is considered isotropic throughout the study.

From equations (24) and (25), it is possible to reach transversal $E_{2_{Lam1}}$ and shear $G_{12_{Lam1}}$ modulus of ply 1:

$$E_{2_{Lam1}} = E_E\left[\left(1 - \sqrt{v_{CFA_1}}\right) + \frac{\sqrt{v_{CFA_1}}}{1 - \sqrt{v_{CFA_1}}\left(1 - E_E/E_{2_{CFA}}\right)}\right] \tag{100}$$

$$G_{12_{Lam1}} = G_E \left[\left(1 - \sqrt{v_{CFA_1}}\right) + \frac{\sqrt{v_{CFA_1}}}{1 - \sqrt{v_{CFA_1}}\left(1 - G_E / G_{2_{CFA}}\right)} \right] \quad (101)$$

where $E_{2_{CFA}}$ and $G_{2_{CFA}}$ are, respectively, transverse and shear modulus of CFA, and G_E is the epoxy shear modulus.

Analogously, the same properties can be evaluated for ply 2. However, although plies 1 and 2 are made of the same CFA and epoxy matrix, v_{CFA_2} is slightly different from v_{CFA_1} due to the geometric variation of the layer. The diameters of ply 2 are larger because it is the outer layer and the number of CFAs also tends to be greater.

After assessing the two plies, it was possible to define the stiffness matrix Q using the macro-mechanics as discussed in section 2.2.7. Using equation (32) in ply 1, we have:

$$\begin{gathered} Q_{11_{Lam1}} = \frac{E_{1_{Lam1}}}{1 - \nu_{12_{Lam1}} \nu_{21_{Lam1}}} \\ Q_{12_{Lam1}} = Q_{21_{Lam1}} = \frac{\nu_{12_{Lam1}} E_{2_{Lam1}}}{1 - \nu_{12_{Lam1}} \nu_{21_{Lam1}}} \\ Q_{22_{Lam1}} = \frac{E_{2_{Lam1}}}{1 - \nu_{12_{Lam1}} \nu_{21_{Lam1}}} \\ Q_{66_{Lam1}} = G_{12_{Lam1}} \end{gathered} \quad (102)$$

Thus:

$$[Q]_{Lam1} = \begin{bmatrix} Q_{11_{Lam1}} & Q_{12_{Lam1}} & 0 \\ Q_{12_{Lam1}} & Q_{22_{Lam1}} & 0 \\ 0 & 0 & Q_{66_{Lam1}} \end{bmatrix} \quad (103)$$

The stiffness matrix shown in equation (103) is from ply 1 at the CFA main axis (1-2). Now, considering that it has its CFAs placed at θ degrees, the transformed stiffness matrix $[\bar{Q}]_{Lam1}$ was evaluated by equation (31). Likewise, for ply 2, with CFAs placed at $-\theta$, $[\bar{Q}]_{Lam2}$ could also be assessed:

$$[\bar{Q}]_{Lam1} = \begin{bmatrix} \bar{Q}_{11_{Lam1}} & \bar{Q}_{12_{Lam1}} & \bar{Q}_{16_{Lam1}} \\ \bar{Q}_{12_{Lam1}} & \bar{Q}_{22_{Lam1}} & \bar{Q}_{26_{Lam1}} \\ \bar{Q}_{16_{Lam1}} & \bar{Q}_{26_{Lam1}} & \bar{Q}_{66_{Lam1}} \end{bmatrix} \quad (104)$$

$$[\bar{Q}]_{Lam2} = \begin{bmatrix} \bar{Q}_{11_{Lam2}} & \bar{Q}_{12_{Lam2}} & \bar{Q}_{16_{Lam2}} \\ \bar{Q}_{12_{Lam2}} & \bar{Q}_{22_{Lam2}} & \bar{Q}_{26_{Lam2}} \\ \bar{Q}_{16_{Lam2}} & \bar{Q}_{26_{Lam2}} & \bar{Q}_{66_{Lam2}} \end{bmatrix}$$

Since flexural and torsional loads are neglected in this study within the EF, only the axial stiffness matrix $[A]$ is evaluated, and for cylindrical coordinates $[A']_{3x3} = [A]_{3x3}$. Then:

$$\begin{aligned} [A']_{3x3} &= [A]_{3x3} \\ &= [\bar{Q}]_{Lam1}(z_{Lam1} - z_{Lam1-1}) + [\bar{Q}]_{Lam2}(z_{Lam2} - z_{Lam2-1}) \end{aligned} \quad (105)$$

where:

z_{Lam1} = Distance from the center of laminate to the outer surface of ply 1;

z_{Lam1-1} = Distance from the center of laminate to the inner surface of ply 1;

z_{Lam2} = Distance from the center of laminate to the outer surface of ply 2;

z_{Lam2-1} = Distance from the center of laminate to the inner surface of ply 2;

Therefore, the complete stiffness matrix of the anchoring cylindric laminate is:

$$[E]_{6x6} = \begin{Bmatrix} [A']_{3x3} & 0 \\ 0 & 0 \end{Bmatrix} \quad (106)$$

Through equation (106) and the relationship given by equation (43) in section 2.2.7, it is possible to correlate the laminate stresses and strains. These parameters may be useful for evaluating the whole composite behavior when submitted to external loads and eventually using some design criteria such as Tsai-Wu, for instance.

Nevertheless, since this study focus on the CFA anchoring and, in this case, the main failure mode considered in this work is its pull-out from EF due to riser axial loads, the approach using debonding energy as per section 2.3.3 was developed in next section.

5.2.2. The anchoring mechanism and pull-out failure model

Despite the particularities of EF geometry from different suppliers and the capstan effect due to the helicoidally organized tensile armors over the flexible pipe, the anchoring resistance of the composite armors can be evaluated preliminarily with a single straight CFA pull-out [96]. Indeed, this kind of study and experiment can provide important properties of the cohesive zone between CFA and epoxy and confirm the importance of having a good adhesion system and a stiff and tough matrix for anchoring the armor.

As already presented in section 2.3.3, there is a common expression that relates linearly a general pull-out force F to an embedded surface, that predicts the interface fails at a constant shear stress ($F_d = 2\pi r L \tau$), where L is the embedded length and r is reinforcement radius. Nevertheless, the best relation representing, for instance, a pull-out failure of a fiber with high longitudinal modulus from a polymeric matrix with low relative modulus from a given composite comes, actually, from an expression of the total strain energy of the system with $\sqrt{L}$ variation [97, 34, 98].

Thus, assuming the CFA as reinforcement and the epoxy as matrix of a bigger scale anchoring composite block inside the EF, the approach with $\sqrt{L}$ is proposed for studying the CFA pull-out.

Therefore, considering a thin epoxy layer following the CFA rectangular shape, that is $\varphi = 0$, but $\theta \neq 0$, the equilibrium of shear forces at distance y with those at the CFA's surface ($y = t/2$) in the anchoring block element shown in Figure 64 can be correlated:

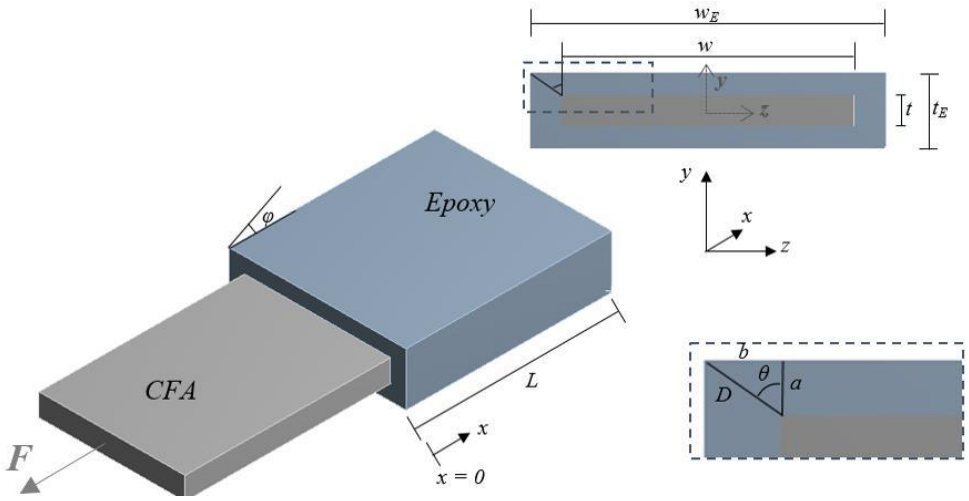

Figure 64 – CFA-epoxy pull-out system.

$$P_E dx\tau = P_{CFA} dx\tau_E \tag{107}$$

$$\tau = \frac{P_{CFA}}{P_E}\tau_E \tag{108}$$

where $P_E = f(D, \theta, w, t)$ and $P_{CFA} = g(w, t)$ are the epoxy and CFA perimeter, respectively.

Now, the relation between τ, the shear strain, $d\gamma/dd$ and the shear modulus, G_E, can be written as:

$$\frac{d\gamma}{dd} = \frac{\tau}{G_E} = \frac{\tau_E P_{CFA}}{G_E P_E} \tag{109}$$

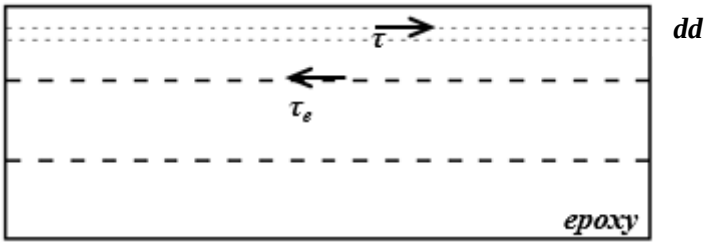

Figure 65 – Shear stresses in the CFA-epoxy anchoring block element.

Integrating this equation, and assuming $G_E = E_E/[2(1+\nu_E)]$, where E_E and ν_E are the epoxy tensile modulus and Poisson's ratio, respectively, the shear stresses at the epoxy surface, τ_E, can be defined:

$$\int_{u_{CFA}}^{u_E} d\gamma = \frac{\tau_E}{G_E}\int_0^D \frac{P_{CFA}}{P_E} dd \tag{110}$$

$$\tau_E = \frac{E_E(u_E - u_{CFA})}{2(1+\nu_E)P_{CFA}\int_0^D \frac{1}{P_E} dd} \tag{111}$$

The CFA stresses will vary from σ_{CFA} to $\sigma_{CFA} + d\sigma_{CFA}$ along an element dx in the embedded surface, see Figure 66. Then, equilibrating the surface shear and tensile forces [99]:

$$S_{CFA} d\sigma_{CFA} = P_{CFA}\tau_i dx \tag{112}$$

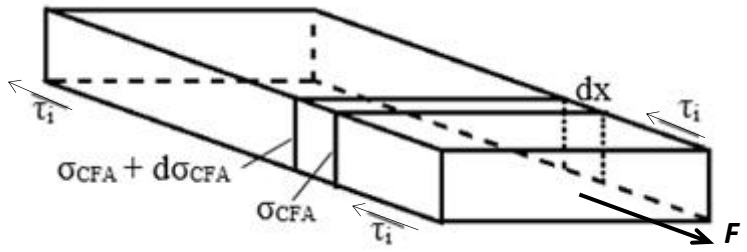

Figure 66 – CFA element with tensile and shear stresses.

Since for elastic stress transfer $\tau_i = -\tau_E$, and substituting it from equation (111):

$$\frac{d\sigma_{CFA}}{dx} = -\frac{1}{S_{CFA}} \frac{E_E(u_E - u_{CFA})}{2(1+\nu_E)\int_0^D \frac{1}{P_E} dd} \tag{113}$$

It is known that the CFA displacement, u_{CFA}, has a correlation with its stress and strain, $du_{CFA}/dx = \sigma_{CFA}/E_{CFA}$, and at $d = D$, $du_E/dx = \varepsilon_E$, where ε_E is the epoxy strain. Therefore, differencing the equation (113):

$$\frac{d^2\sigma_{CFA}}{dx^2} = -\frac{1}{S_{CFA}} \frac{E_E\left(\varepsilon_E - \frac{\sigma_{CFA}}{E_{CFA}}\right)}{2(1+\nu_E)\int_0^D \frac{1}{P_E} dd} \tag{114}$$

To simplify the following expressions, a dimensionless parameter is introduced:

$$n_{CFA}{}^2 = \frac{E_E}{2(1+\nu_E)E_{CFA}} \tag{115}$$

Then, the differential equation (114) can be rearranged as

$$\frac{d^2\sigma_{CFA}}{dx^2} = \frac{n_{CFA}{}^2}{S_{CFA}\int_0^D \frac{1}{P_E} dd}(\sigma_{CFA} - \varepsilon_E E_{CFA}) \tag{116}$$

Assuming $\varepsilon_E = 0$ at $d = D$, it becomes a second order linear ordinary differential equation (ODE), which can be written as

$$y''(x) - cy(x) = 0 \tag{117}$$

where

$$c = \frac{n_{CFA}{}^2}{S_{CFA}\int_0^D \frac{1}{P_E} dd} \tag{118}$$

For boundary conditions, $\sigma_{CFA} = \sigma_{CFA_E}$ (CFA stress prior entering in epoxy) at $x = 0$ and $\sigma_{CFA} = 0$ at $x = L$, thus the ODE (117) has the solution:

$$\sigma_{CFA} = \sigma_{CFA_E} \frac{e^{-\sqrt{c}x}\left(e^{2\sqrt{c}L} - e^{2\sqrt{c}x}\right)}{e^{2\sqrt{c}L} - 1} \tag{119}$$

Figure 67 shows the graph of the decreasing behavior of CFA stress σ_{CFA} in the anchoring length.

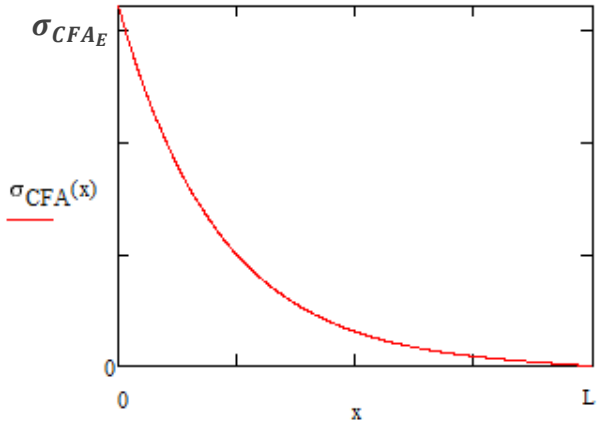

Figure 67 – Decreasing behavior of CFA stress along the anchoring length in the epoxy.

The shear stress at the interface between CFA and epoxy can then be reached by combining equations (112) and (119):

$$\tau_E = -\frac{S_{CFA}}{P_{CFA}} . \frac{d\sigma_{CFA}}{dx} \tag{120}$$

Which gives the following equation of shear stress (graph is presented in Figure 68):

$$\tau_E = \frac{S_{CFA}}{P_{CFA}} \left(\sqrt{c}\sigma_{CFA_E} . csch(\sqrt{c}L) cosh\left(\sqrt{c}(L-x)\right)\right) \tag{121}$$

Thus, the maximum shear stress, $\tau_{e_{max}}$, is at $x = 0$. Then, equation (121) becomes

$$\tau_{e_{max}} = \frac{S_{CFA}\sigma_{CFA_E}\sqrt{c}coth(\sqrt{c}L)}{P_{CFA}} \tag{122}$$

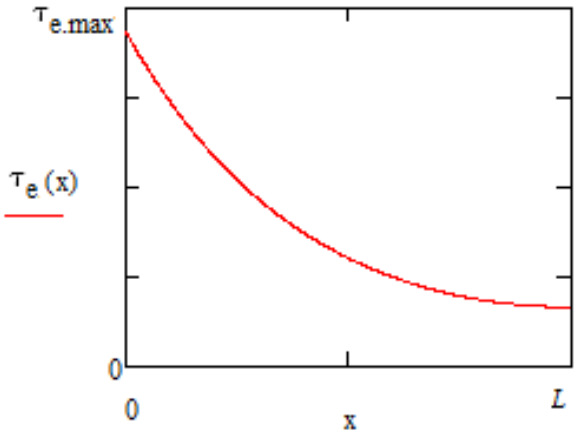

Figure 68 – Decreasing behavior of Shear stress between CFA and epoxy along the anchoring length.

Now, the strain energy of the CFA, U_{CFA}, can be evaluated as

$$U_{CFA} = \int_0^L \frac{{\sigma_{CFA}}^2 S_{CFA}}{2E_{CFA}} dx \tag{123}$$

Which gives

$$U_{CFA} = \frac{S_{CFA}{\sigma_{CFA_E}}^2}{2E_{CFA}} \left(\frac{1}{2} \left(\frac{\coth(\sqrt{c}L)}{\sqrt{c}} - L.csch^2(\sqrt{c}L) \right) \right) \tag{124}$$

And, the induced energy in the epoxy, U_E, at CFA surface is

$$U_E = \frac{P_{CFA}}{2} \int_0^L \tau_E . u_{CFA} \, dx \tag{125}$$

where u_{CFA} can be calculated from equation (111) assuming zero shear strain at $d = D$:

$$u_{CFA} = -\frac{\tau_E P_{CFA} \int_0^D \frac{1}{P_E} dd}{n^2 E_{CFA}} \tag{126}$$

Then, applying in equation (124):

$$U_E = \frac{S_{CFA}{\sigma_{CFA_E}}^2}{2E_{CFA}} \left(\frac{1}{2} \left(\frac{\coth(\sqrt{c}L)}{\sqrt{c}} + L.csch^2(\sqrt{c}L) \right) \right) \tag{127}$$

Therefore, the total strain energy of the system, U_T, is:

$$U_T = U_{CFA} + U_E = \frac{S_{CFA}{\sigma_{CFA_E}}^2}{2E_{CFA}} \left(\frac{\coth(\sqrt{c}L)}{\sqrt{c}} \right) \tag{128}$$

The CFA pull-out occurs when the total strain energy, U_T, is achieved. Thus, at the interface, it fails when the tensile force is large enough to overcome the debonding energy, G_c, per unit of embedded area. Thus, the relation $U_T = P_{CFA} L G_c$ can be applied [97, 34].

Then, from equation (128), and knowing the external tensile force ($F = \sigma_{CFA_E} S_{CFA}$), the general formula for CFA pull-out or debonding force, F_d, can finally be written as

$$F_d = \sqrt{2E_{CFA} G_c S_{CFA} P_{CFA} L \sqrt{c} \tanh(\sqrt{c}L)} \tag{129}$$

5.3. FEM FOR VERIFYING PULL-OUT FAILURE MODEL

To verify the equation (129), a 2D plane stress FEM of a single CFA pull-out was performed considering a cohesive zone model (CZM) contact debonding [85] between the CFA and epoxy. To enable such analysis, the CZM of CFA-epoxy was simplified considering only at the width w of CFA cross section, that is parallel to yz plane, where $\theta = 0°$, which gives $D = a$, see Figure 64.

Indeed, in practice it is easier to guarantee a homogenous cohesive zone with flat and larger surfaces, especially if the epoxy has relative high viscosity ($> 10000\ mPa.s$) since it circumvents geometries more difficultly, then narrow surfaces may raise mis bonding. Figure 71 presents the CFA pull-out model where $w \cong 7 \times t$.

Depending on the boundary conditions due to the EF epoxy chamber design, the pull-out of the CFA can be assumed as mode II bilinear dominated from CZM as per a fibre debonding [85]. Thus, the separation of the material interfaces is dominated by the displacement jump tangent to the interface.

Three parameters were required for CZM: Critical debonding energy for tangential slip, G_{2c}; Maximum equivalent shear stress, $\tau_{e_{max}}$, which is given by equation (122); And Artificial damping coefficient, μ. According to other authors [86, 87], this value should not be greater than 0.1 times the FEM time increment ($1s$) to guarantee reliable results. In the other hand, too low values of μ may turn the model more difficult to converge and time consuming. Therefore, the values $0.01s$ and $0.005s$ were considered to keep low computational time.

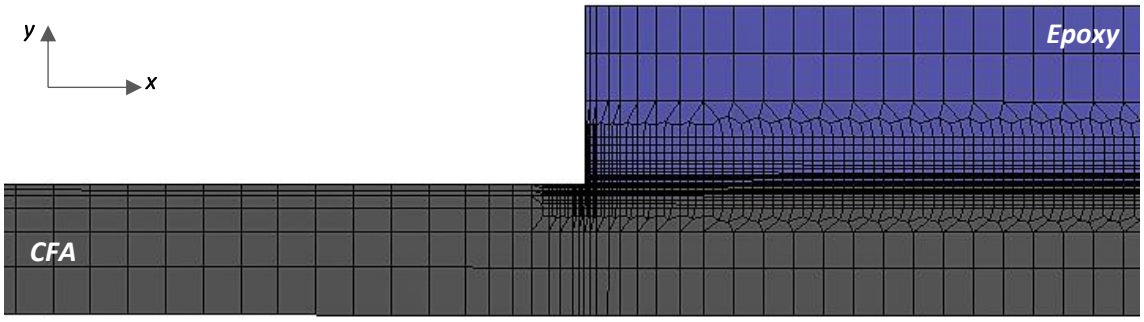

Figure 69 – Mesh of FEM CFA pull-out system.

A homogenous mesh well refined especially at the cohesive zone was prepared as presented in Figure 69. At the debonding tip, small QPE elements were designed as

recommended for fracture mechanics model [84] and described in section 2.4.3. See Figure 70.

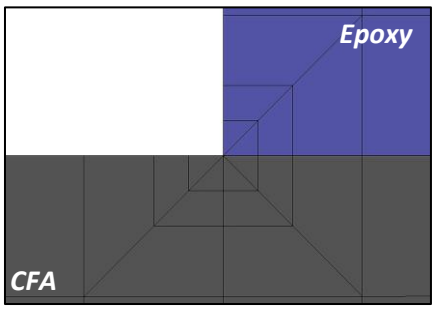

Figure 70 – Mesh with QPEs at debonding tip.

As boundary conditions, a displacement in x direction was introduced at the extremity of the CFA, corner opposite to the epoxy. This one had free displacement at yz plane. And, a symmetry was applied normal to xz plane as shown in Figure 71.

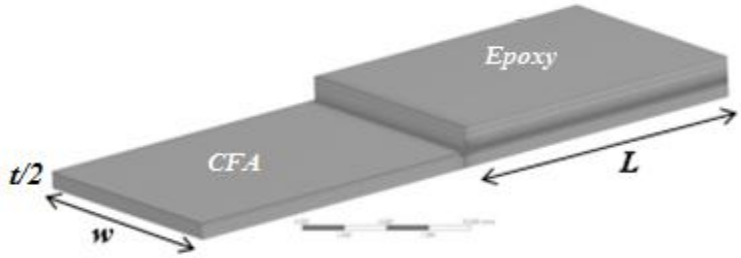

Figure 71 – FEM of CFA-epoxy pull-out system with symmetry in xz plane.

Two FEM models have been prepared to verify the deviation from analytical model for thinner and thicker epoxy layers, t_E, and length, L. Therefore, thicknesses t_E and $20 \times t_E$, and lengths L and $10 \times L$ were studied. Then, the debonding energy, G_{2c}, and the epoxy tensile modulus, E_E, were correlated with the CFA pull-out force, F_d.

Table 4 presents the main properties and geometries of CFA and epoxy given by *TechnipFMC*® group and considered in the study case for performing the analysis.

Table 4 – CFA and epoxy main properties used in FEM

	Tensile Modulus E_1 (*GPa*)	Poisson's coefficient v_{12}	Thickness (*mm*)	width (*mm*)
CFA	136	0.3	2.2	14.2
Epoxy	8*	0.35	1.5 and 30	14.2

*These are initial values since these properties were variables of the model.

5.4. TOUGHENING EPOXY MATRIX AND TESTING

5.4.1. Defining filler to reinforce epoxy

To reinforce the epoxy matrix, some filler materials were studied. Technical parameters for improving properties and its feasibility for implementation were considered for the definition of the most suitable for the application.

The following verified technical characteristics are presented:

- Mechanical resistance, tensile and shear modulus;
- Adhesion;
- Elongation at rupture;
- Fracture toughness;
- Glass transition temperature (Tg);
- Shrinking after cure;
- Chemical resistance when submitted to CO_2, H_2O, H_2S under high temperatures;
- Viscosity;
- Gel time.

The first four items are considered primordial for the system, as they directly impact the optimization of the composite and the stability of its properties at high temperatures; Post-curing is also a parameter to be analyzed, since large volume variations can generate residual stresses and, consequently, premature failure of the laminate; As explained in section 2.1, the anchoring of the CFAs is in contact with the flexible riser annulus fluids, so the chemical resistance is another factor that must be evaluated; Mechanical strength and modules shall be warranted to confirm the integrity of the structure under the stress and strain state; Very high viscosities can compromise the injection of the epoxy resin causing internal voids in the laminate, and the curing time, if it is much larger than usual, can invalidate the solution, as it would increase its operating cost.

It is important to point out that the selected materials do not always have bibliographic references related to all these parameters. In this case, the materials that offered more

information in the literature were considered more viable because of the greater knowledge of the solution. Other factors adopted for the feasibility study were the cost and availability of the material on the market. Then, the feasibility items were:

- Knowledge of solution (Literature references);
- Cost and material availability on market.

Figure 72 presents a summary of the classification performed considering the mentioned parameters for the following materials: MWCNTs (DWCNTs included), SWCNT, Graphite, PTFE, CTBN, PA, PU, Carbon black, CTNB liquid and Aramid. It is a trend assessed based on the literature that was described is section 2.2.4.

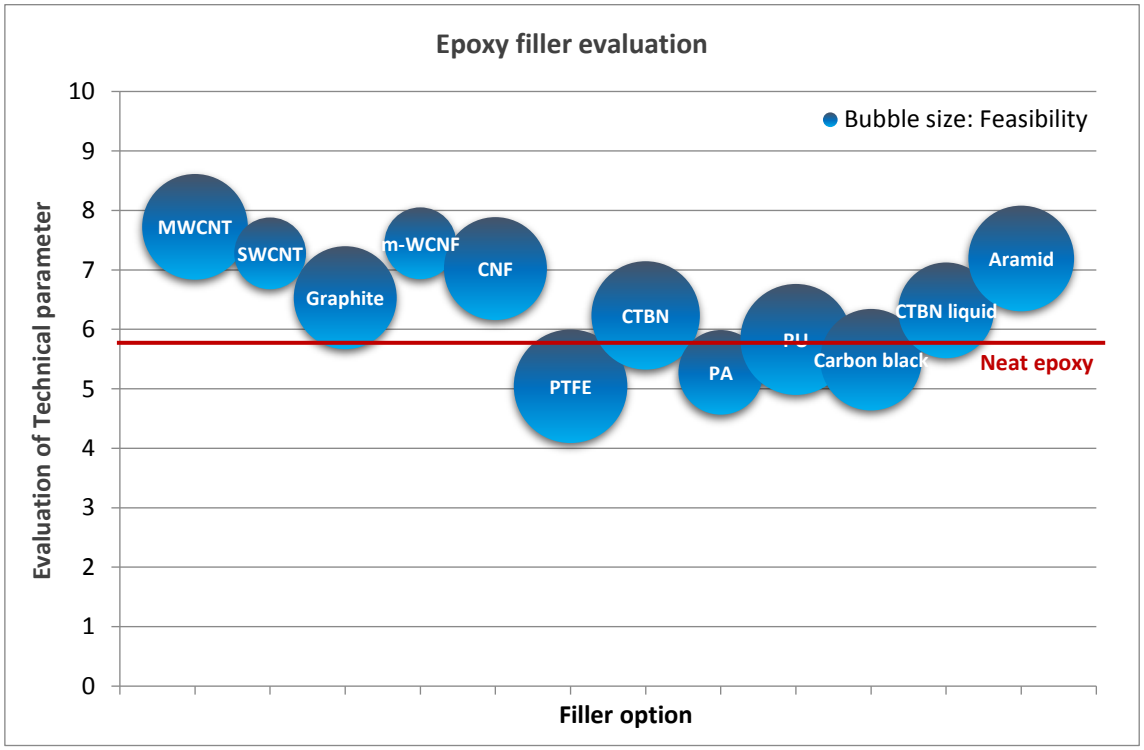

Figure 72 – Comparative bubbles graph of materials for epoxy reinforcement.

In the graph, the y-axis represents the score of 1 to 10 assigned to the technical parameters of the options, of which mechanical resistance, adhesion, fracture toughness and elongation received the highest weight. The bubble size refers to the solution score for feasibility.

Thus, the following conclusions were reached:

- PTFE and PU polymers have good viability, mainly due to cost, if compared to nanoparticles, and availability in the market [44]. However, PTFE results loss of

toughness as presented in section 2.2.4.1, and the adhesion strength to the adherent and the final Tg of the system are unknown, since no bibliographic references were found on the subject. And PA material is sensitive to mechanical embrittlement by hydrolysis [101].

- Liquid and granular CTBNs confirmed good feasibility and increased fracture toughness and elongation. However, the major drawbacks of these options are the decrease in Tg according to SALINAS-RUIZ *et al.* [100], the uncertainty regarding its chemical resistance when subjected to CO_2, H_2O, H_2S in high temperatures and the uncertainty on the adhesion strength to the adherent;

- MWCNT and Aramid, in turn, were viable and with a potential good technical performance. As mentioned in sections 2.2.4.2 and 2.2.4.3, Aramid and MWCNT confirmed excellent gains in mechanical properties, adhesion without losing toughness and Tg [101]. Nevertheless, Aramid has important drawbacks of swelling and hydrolysis [103], while MWCNT provides very good thermal and chemical stability [100, 33]. The negative point of this material could be the cost, however considering the concentrations used in the cited literature, this factor could be negligible for the final cost of the product, although cost of processing should be further considered for any of chosen filler.

Therefore, the material selected to reinforce the epoxy for anchoring CFAs were MWCNT. Small scale tests for characterization of mechanical resistance and adhesion to the CFA were carried out.

It is important to highlight that the evaluation of the chemical resistance of these materials with epoxy when subjected to CO_2, H_2O and H_2S under high temperatures is not foreseen in this study, however it is an important factor and should be considered in future works.

5.4.2. Scope of tests and material

To characterize the gain of mechanical properties of the filled epoxy, tensile [90], compressive [91] and fracture toughness [92, 93] small-scale tests were carried out with toughened and neat epoxy specimens. Then, the most mechanically performant epoxy composite was taken for debonding toughness by double cantilever beam MMB test [95] and shear strength [94] by lap shear test with CFA-epoxy samples. Table 5 summarizes the list of mechanical tests.

The CFA material used was an orthotropic unidirectional carbon fiber composite with a thin short fibers Mat at the surface supplied by *TechnipFMC® Group*. The epoxy resin chosen for the anchoring study was a diglycidyl ether bisphenol F-epichlorohydrin with cyclohexylamine based hardener.

Table 5 – Scope of mechanical tests

N°	Test	Material	Properties sought
1	Tensile	Epoxy	UTS, YS, Tensile modulus, Elongation
2	Compressive	Epoxy	Compressive strength, modulus
3	Fracture toughness	*Epoxy*	Fracture toughtness *(K_{1c}, G_{1c})*
4	Double cantilever beam MMB	Epoxy-CFA	Debonding toughness *(G_c, G_{1c}, G_{2c})*
5	Lap shear	Epoxy-CFA	Shear strength

MWCNTs were acquired from *Nanocyl®* and *TimesNano®* suppliers, and some of those with -COOH and -NH_2 covalent bond functional groups. According to suppliers, the aspect ratio varied from 100 to 2500 depending on CNT type. Thus, following the already cited literature for reinforcement of matrices with MWCNT, two different weight concentrations were considered: 0.5 wt.% and 1.0 wt.%. Table 6 summarizes the characteristics of all studied MWCNTs.

Table 6 – Summary data of studied MWCNTs

N°	Supplier	Functional group	Diameter (ηm)	Length (μm)
1	*Nanocyl®*	-	~10	1-2
2	*TimesNano®*	-	20-30	10-30
3	*TimesNano®*	-COOH	20-30	10-30
4	*TimesNano®*	-NH_2	20-30	~50
5*	*Nanocyl®*	$C_3H_6N_6$	20-30	10-30
6*	*TimesNano®*	-COOH & $C_3H_6N_6$	20-30	10-30
7*	*TimesNano®*	-NH_2 & $C_3H_6N_6$	20-30	10-30

(*) Non-covalent *π-π* bond functionalization with Melamine ($C_3H_6N_6$) performed at MSSMAT laboratory with nanotubes from suppliers *Nanocyl®* and *TimesNano®*.

A Transmission electron microscopy (TEM) was accomplished with all CNTs, not yet mixed into the epoxy, to confirm and compare their sizes, number of walls and

morphology. The results of analysis are detailed in section 6.2.3. The microscopy work was carried out within the MATMECA consortium supported by the ANR under contract number ANR-10-EQUIPEX-37. It has benefited from the facilities of the Laboratory MSSMat (CNRS UMR8579), École *Centrale Supélec*, France.

Tensile tests were performed with the 1 to 4 nanotube types from the table due to the simplicity of the test and the important information that it can provide such as strength, modulus, elongation and toughness. Since many CNT types and two different weight concentrations were selected, only the Nano composite which provided relevant improvement under tension was taken for the other tests.

Specimens with MWCNTs 5 to 7 listed in Table 6 were performed only after carrying out the whole campaign of mechanical tests. The method used was an additional surface treatment by non-covalent π-π bond functionalization with Melamine ($C_3H_6N_6$) and is better detailed in section 5.4.4. The purpose was to better improve more the interface interaction CNT-epoxy and, therefore, reaching an even better mechanical behavior. The effectiveness of the treatment was assessed through Energy-dispersive X-ray spectroscopy (EDX) with TEM and X-ray photoelectron spectroscopy (XPS). Thus, an extra tensile test was performed with the MWCNT that confirmed more presence of non-covalent functional groups. Unfortunately, no tests were assessed with $C_3H_6N_6$ functionalized epoxy and CFA because it was studied at the end of this work, but it is recommended for future researches since it has provided good improvement in epoxy strength properties. Further information is presented in section 6.2.5.

Some Scanning electron microscopy (SEM) and optical microscopy were conducted after performing all tests to verify the CNTs dispersion and to characterize the fracture. The microscope was the JEOL JSM-6010PLUS/LV.

Preparation of epoxy material, execution of tensile and compressive mechanical tests, EDX analysis, TEM, SEM and optical microscopies were performed at MSSMAT laboratory, *École Centrale Supélec*. XPS study was carried out by ITODYS laboratory from *Université Paris Diderot - Sorbonne Paris Cité*. And, mechanical tests with CFA and fracture mechanics with epoxy were conducted at *Rescoll Société de Recherche*® laboratory in Bordeaux.

5.4.3. Experimental procedure and material processing

For processing the Nano composite samples, some steps were defined and respected during the whole campaign. Knowing that a good dispersion of MWCNTs is very

important to guarantee a homogenous sample material, two different methods of mixing were considered separately and then compared to each other: high shear mixing three roll mill and ultrasonication.

When using three roll mill, a time of one hour with a gap between cylinders of 5µm and speed 30rpm was set. Whereas using ultrasonication, the setup was Pulse On for two seconds, Pulse Off for four seconds and 40% of amplitude for one hour. In this case, the sample was placed in cold water bath to avoid overheating.

To mitigate defects in samples, two vacuums were applied during thirty minutes at ambient temperature prior and just after applying the hardener. The second vacuum step was possible due to the high pot life provided by the chosen epoxy-hardener compound. The ratio epoxy/hardener used was 3:1. For the samples that had CFA (debonding toughness and lap shear), the adhesion was performed at this step. Then, the prepared materials were placed in the molds and cured at 60°C for twenty hours. The neat epoxy samples followed almost the same steps, except for the mixing machine and first vacuum.

Prior preparing the samples, CFAs were cut by diamond blade to reach the correct length, stabilized for twenty-four hours at sixty degrees Celsius, then conditioned at twenty degrees Celsius and fifty percent relative humidity. For bonding with epoxy, the CFA was degreased with ethanol, and a minimum of two hours of evaporation was respected before adding the epoxy adhesive. Figure 73 resumes all steps performed for processing the samples.

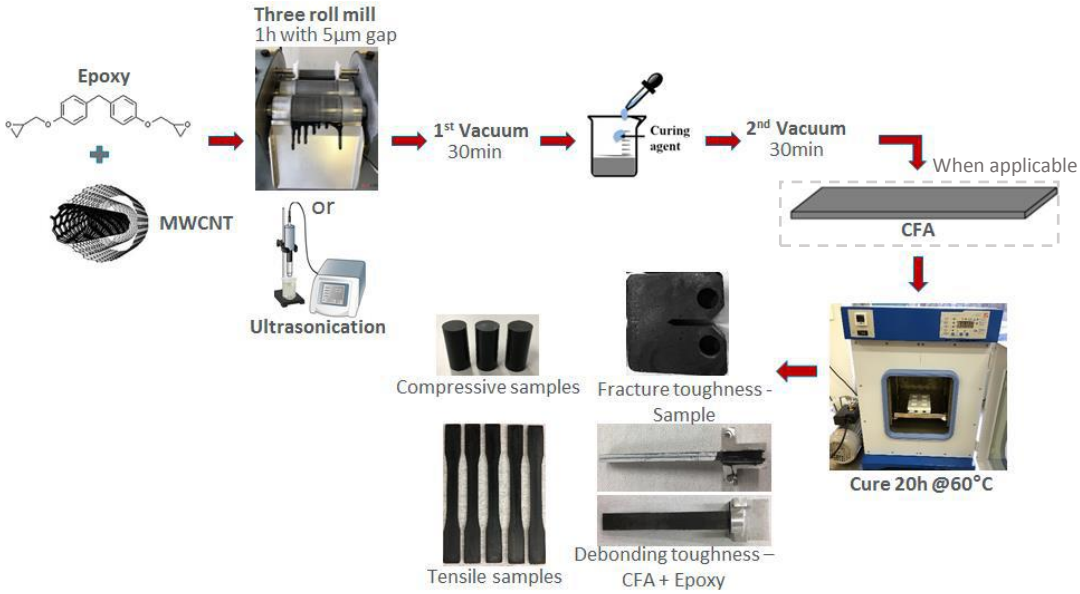

Figure 73 – Summary of samples processing protocol.

Five samples were prepared for each test. The machine used for the tensile tests was an *Instron 4206*, with a 30kN static load cell, ±2.5mm travel extensometer and speed 1.2mm/min. Test was based on ASTM D638 [90]. For the compressive tests, an *Instron 4482* machine was used with a 30kN static load cell, and same travel extensometer and speed. Test was based on ASTM D695 [91]. Fracture toughness tests were carried out based on ISO 13586 [92] and geometry on ASTM E399 [93], with static load cell 10kN, laser extensometer and speed 2mm/min. Lap shear from ASTM D3165 [102], with static load cell 45kN, video extensometer and speed 1mm/min. Finally, debonding toughness tests were performed based on ASTM D6671 [95], with a mixed mode bending (MMB) device, with 10kN static load cell and speed 0.5mm/min.

5.4.4. Protocol of non-covalent surface treatment

After performing the campaign of mechanical tests, an additional surface treatment was carried out based on a study done by CHA *et al.* [58]. Therefore, three types of MWCNTs were selected for non-covalent *π-π* bond functionalization with Melamine ($C_3H_6N_6$). The objective was to improve more the interface interaction CNT-epoxy and reach even better mechanical properties.

Melamine ($C_3H_6N_6$) from *Aldrich*® supplier was acquired as functional molecule. As shown in Figure 74, it has a hexagonal C-N ring structure suitable for *π-π* interactions with carbon nanotubes.

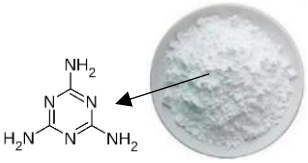

Figure 74 – Melamine ($C_3H_6N_6$).

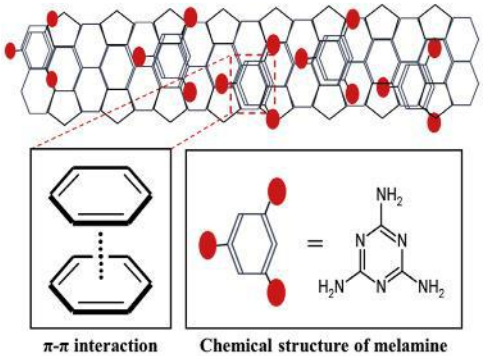

Figure 75 – Non-covalent *π-π* bond functionalization of MWCNT with Melamine ($C_3H_6N_6$) [58].

For preparing the MWCNTs+$C_3H_6N_6$ compound, 500mg of Melamine was dissolved in ethanol. Then, 500mg of MWCNT was added to the solution and sonicated for one hour. The solution was magnetic stirred for another one hour at seventy degrees Celsius. The solution was then filtered with a PTFE membrane with 0.2 µm under vacuum for 10 min and the resulting black solid was dried at a hundred degrees Celsius for twenty-four hours. The MWCNT+$C_3H_6N_6$ powder was then ready for testing.

Chapter 6 – Results and discussion

6.1. PULL-OUT FAILURE MODEL

The CFA pull-out formulation assessed in section 5.2.2 has confirmed the exponential behavior of the CFA pull-out force F_d with the increase of anchoring L, also function of CFA, epoxy and cohesive zone properties. It resulted in lower values of F_d, when compared to the common expression that relates F_d, the embedded surface L, and a constant shear stress.

Regarding the graph presented in Figure 76, it is clear the difference between the pull-out models cited in section 2.3.3. $F_{d_{mean.shear}}$ is based on interface failure at a constant shear stress along L. That is

$$F_{d_{mean.shear}} = P_{CFA} L \tau_{mean} \tag{130}$$

where τ_{mean} is the shear strength of the interface CFA-epoxy. It varies linearly with L, limited by the axial force resistance of the CFA (F_{CFA}). This means it reaches the maximum pull-out force when $L = L_c$, that is the critical length, which is given by

$$L_c = \frac{\sigma_{CFA_{Max}} S_{CFA}}{P_{CFA} \tau_{mean}} \tag{131}$$

where $\sigma_{CFA_{Max}}$ is the CFA tensile strength. Note that this expression does not depend on epoxy mechanical properties neither on its geometry.

Third curve predicts CFA debonding when the maximum shear stress reaches the interface shear strength at some point along anchoring length, in this case at the entrance of CFA to the epoxy anchoring block. It considers epoxy parameters, nevertheless the failure occurs prematurely due to the stress concentration. Thus, increasing the anchoring length impacts only up to maximum shear stress, then pull-out force remains constant. The formulation is given by equation (122) from section 5.2.2.

$$F_{d_{.shear}} = \frac{\tau_{mean} P_{CFA} \tanh\left(\sqrt{c} L\right)}{\sqrt{c}} \tag{132}$$

Figure 77 shows the difference of behavior between the proposed CFA debonding force (F_d) and pull-out based on maximum shear stress at the entrance of the anchoring block.

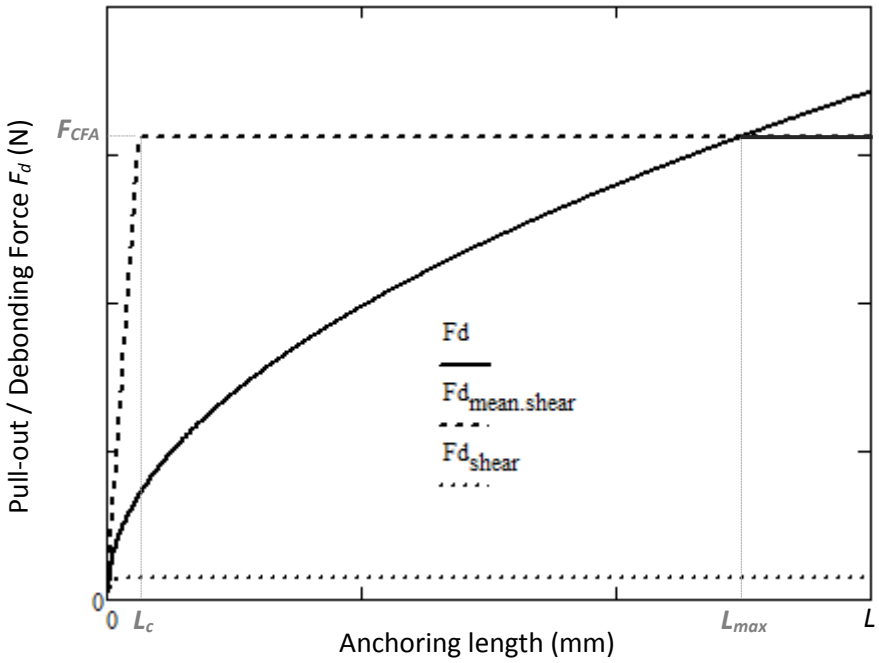

Figure 76 – CFA debonding force (F_d) vs anchoring length (L). Comparison between proposed pull-out model based on debonding energy, common pull-out expression based on mean shear stress varying linearly with L, equation (86), limited by CFA maximum axial force (F_{CFA}), and pull-out formulation based on maximum shear stress at the entrance of the anchoring block.

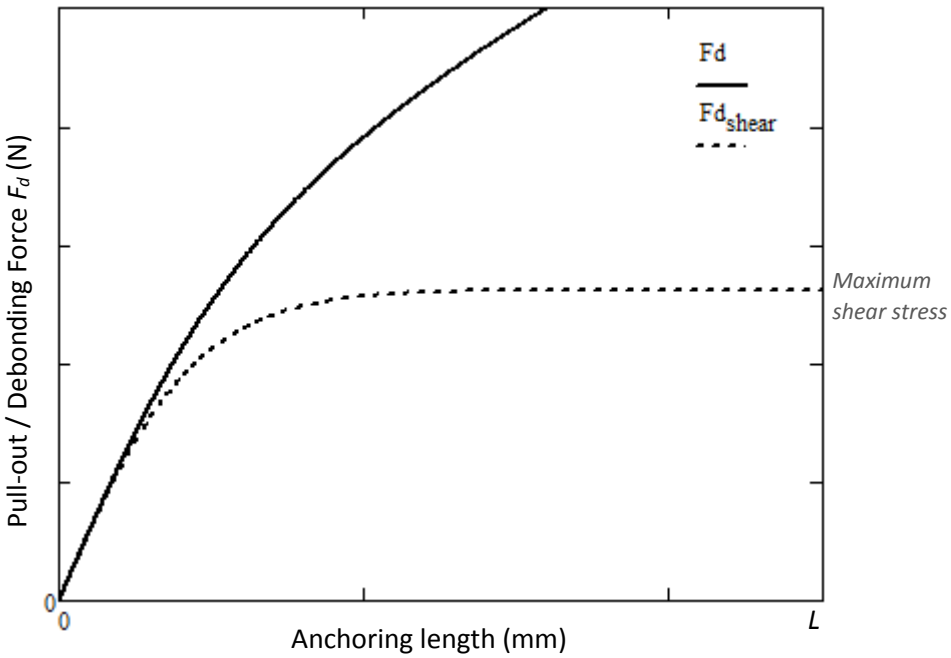

Figure 77 – CFA debonding force (F_d) vs anchoring length (L). Comparison between proposed pull-out model and pull-out formulation based on maximum shear stress at the entrance of the anchoring block.

It is important to mention that the proposed analytical model also has a maximum anchoring length L_{max}, which occurs when it reaches the axial force resistance of the CFA (F_{CFA}).

Another failure mechanism that can limit the pull-out force is by reaching the maximum epoxy elongation. It may create crack propagation spots and split the anchoring length, which would impact even more the pullout resistance, especially if the epoxy has some defects/voids that came from processing or curing phases. The elongation of the epoxy ε_E could be calculated through the equation (126) in section 5.2.2

$$\varepsilon_E = \frac{|u_{CFA}|}{L} = \frac{\tau_E P_{CFA} \int_0^D \frac{1}{P_E} dd}{n^2 E_{CFA} L} = \frac{\tau_E P_{CFA}}{c S_{CFA} E_{CFA} L} \tag{133}$$

Therefore, assuring an epoxy matrix with good strength and elongation is important to guarantee a resistant and tough anchoring system.

Regarding the epoxy geometry parameters, while the increasing anchoring length is exponentially directly proportional to CFA pull-out force, the larger the epoxy thickness or perimeter, lower will be the debonding resistance, also exponentially. Figure 78 shows this behavior and an asymptotic trend to a minimum force.

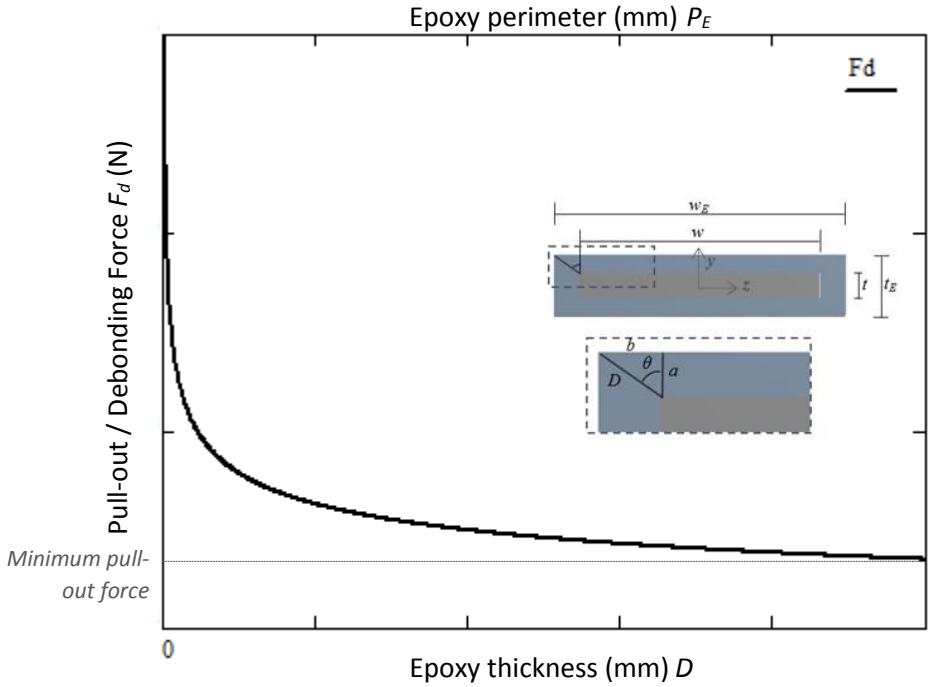

Figure 78 – CFA debonding force (F_d) vs epoxy diagonal thickness (D) or epoxy perimeter (P_E).

Finally, to confirm the influence of epoxy mechanical properties, that is tensile modulus E_E, and energy debonding CFA-epoxy G_c on pull-out resistance, two graphics are presented hereafter. It can be seen from formulation that G_c provides greater impact since modulus E_E is term of the constant c, which is in square root. Anyway, both properties were sought to be increased with the toughened epoxy but not forgetting strength and elongation.

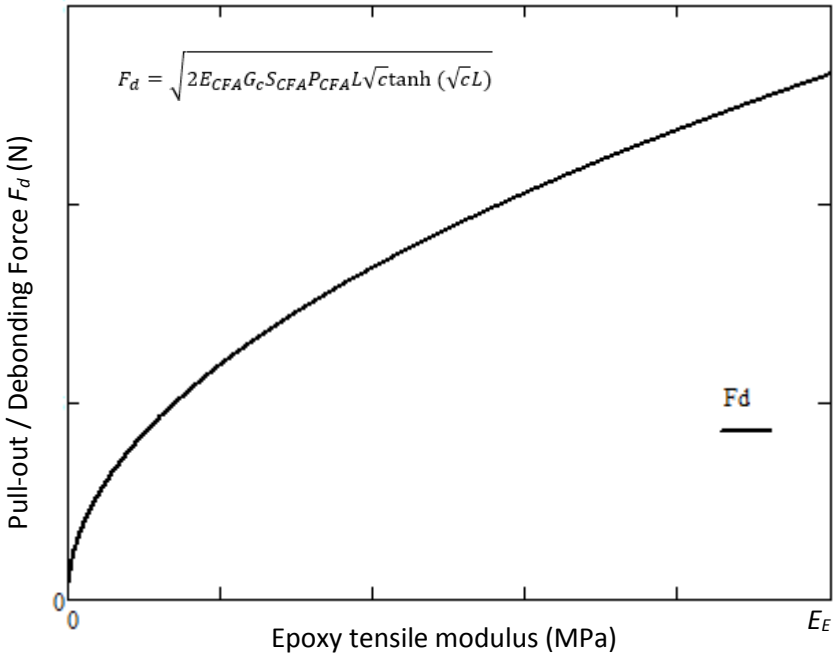

Figure 79 – CFA debonding force (F_d) vs epoxy tensile modulus (E_E).

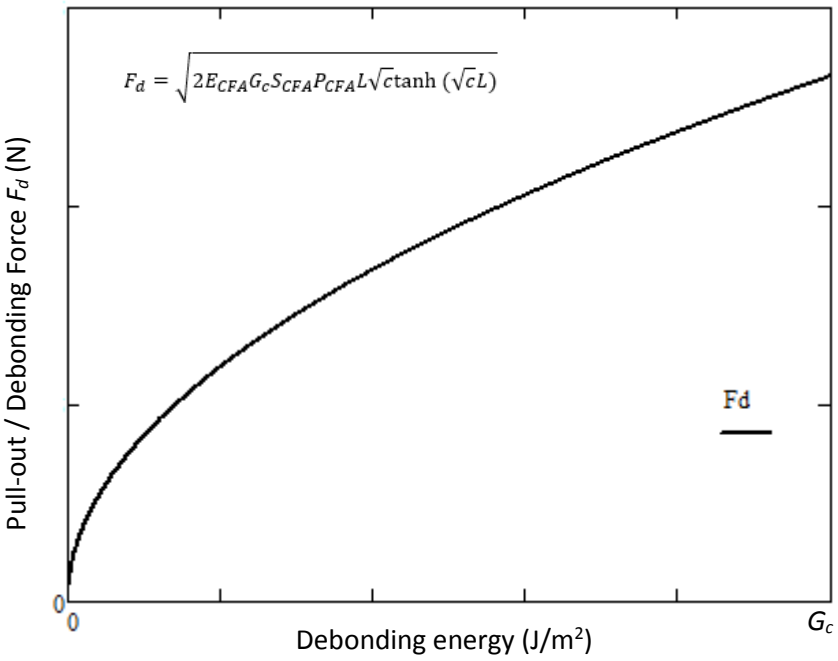

Figure 80 – CFA debonding force (F_d) vs CFA-epoxy debonding energy (G_c).

Therefore, the proposed CFA pull-out model confirmed the dependence of epoxy, CFA and adhesion mechanical properties, although CFA properties were considered constant throughout the study.

Graphs of CFA tensile stress σ_{CFA} and shear stress τ_E assessed in section 5.2.2 and summarized in Figure 81 confirmed for both stresses the exponential decreasing behaviour along the anchoring length L, as expected.

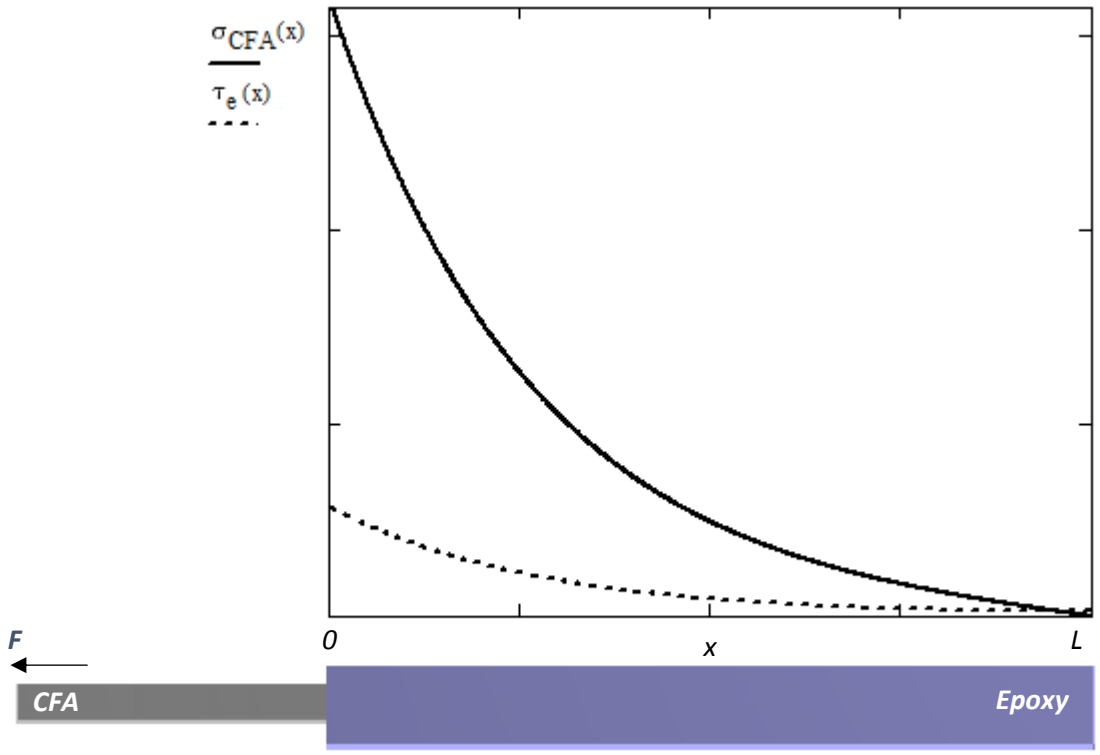

Figure 81 – Illustration of decrease of tensile stress σ_{CFA} and shear stress τ_E along anchoring length.

The analytical model was evaluated and compared to FEM considering a case study with some material properties and geometry presented in section 5.3, and varying basically G_c and n_{CFA}, that is epoxy tensile modulus, E_E.

A comparison of analytical and numerical models is shown in Figure 82. It verified the stability of the model also for higher lengths and thicker matrix, presented in Figure 82c).

FEM has reached an average deviation of 5% with no increase on the range edges even for high length and larger G_c, which confirmed a good approach of the proposed formulation. The damping coefficient of 0.01 and 0.005 that were proposed based in reference [87] presented small difference between their results and consistent convergence for each analysis.

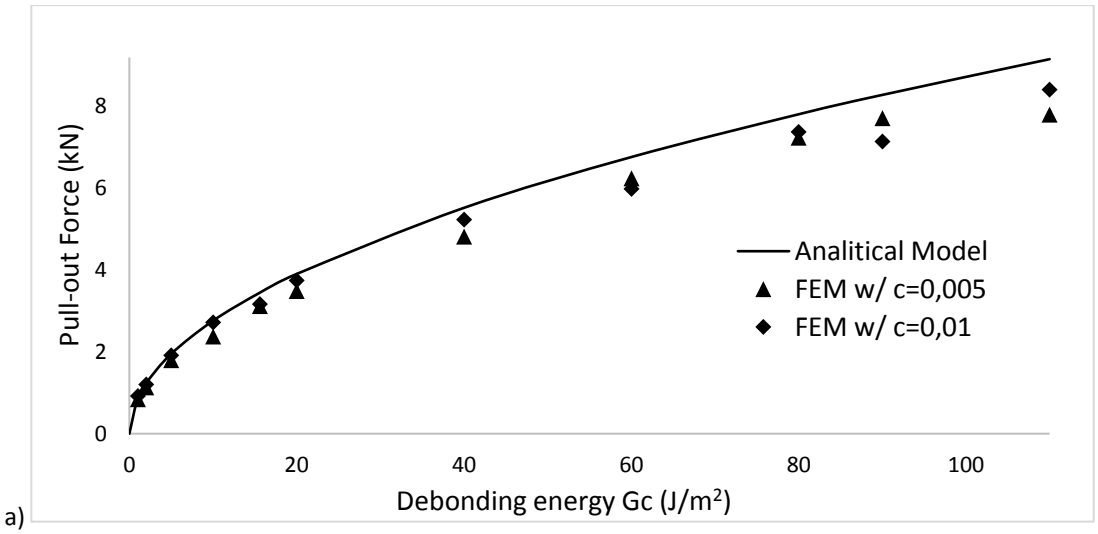

a)

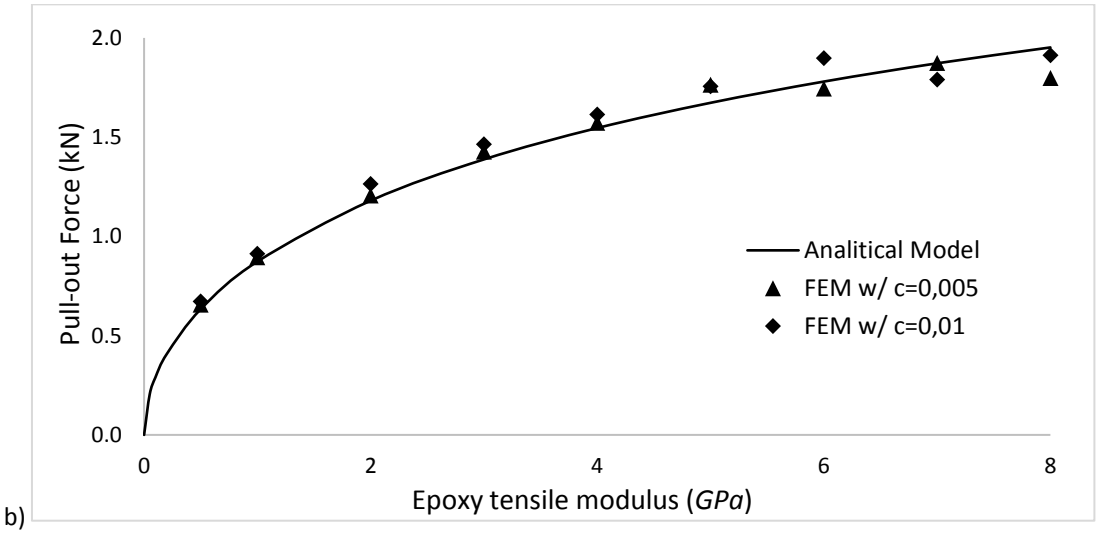

b)

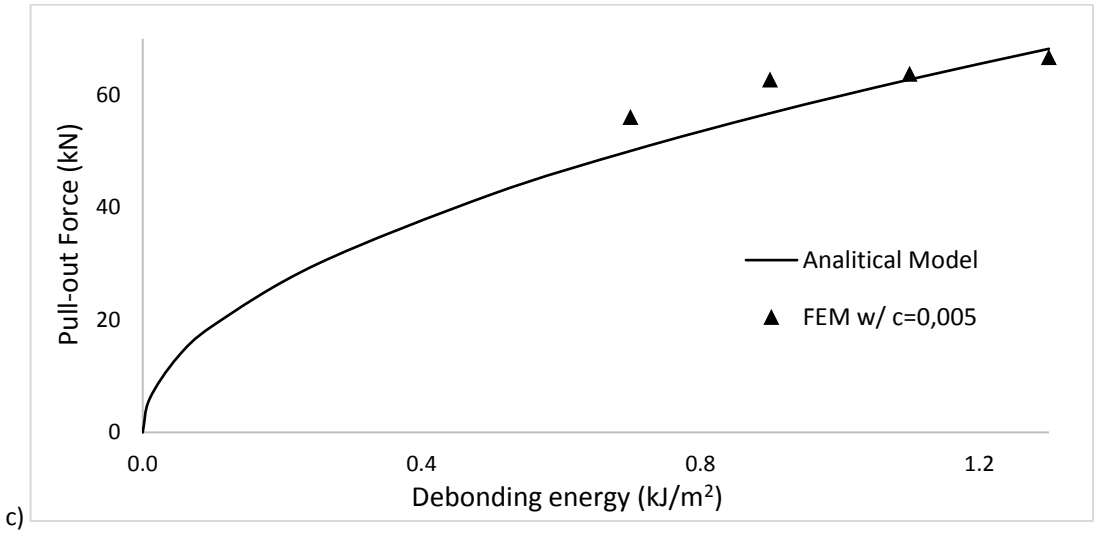

c)

Figure 82 – Analytical and numerical models of CFA pull-out force F_d vs: a) debonding energy G_c for $L = 20mm$ and $t_E = 5.2mm$; b) epoxy tensile Modulus E_E for $L = 20mm$ and $t_E = 5.2mm$; c) debonding energy G_c for $L = 200mm$ and $t_E = 70mm$.

By analyzing graphs from previous pages and equation (133), it is clear the dependency of CFA anchoring mechanism to CFA, epoxy and adhesion properties. Since CFA is constant during the whole work, the epoxy and cohesive zone must be improved to increase the pull-out/debonding force.

Next section presents the results found by toughening the epoxy with MWCNTs.

6.2. TOUGHENING EPOXY STUDY

6.2.1. Small scale mechanical tests

The results found from the mechanical tests confirmed an improvement of epoxy mechanical properties and CFA-epoxy adhesion. Table 7 correlates the CNTs and mechanical tests executed. It is important to ratify that only the most performant epoxy composite in tension was taken for the other tests due to the large number of tests. Nevertheless, additional tensile and compressive tests were carried out with non-functionalized MWCNTs and COOH-MWCNTs from *TimesNano*® with 0.5 wt.% and 1.0 wt.%. The objective was to compare the effect of the weight concentration and functionalization of CNTs with the same size, morphology and from the same supplier.

Table 7 – Resume of mechanical tests performed with each MWCNT

			Mechanical test				
N°	Supplier	Functional group	Tension	Compression	Fracture Toughness	Lap shear	Double cantilever beam
1	*Nanocyl*®	-	x	-	-	-	-
2	*TimesNano*®	-	x	x	-	-	-
3	*TimesNano*®	-COOH	x	x	x	x	x
4	*TimesNano*®	$-NH_2$	x	-	-	-	-

An important remark about *Nanocyl*® CNTs is that only 0.5 wt.% was considered. Since they had lower density, a much bigger volume was required to reach the desired weight concentration. Its morphology has been verified through TEM analysis and a correlation to the density is presented in section 6.2.3. When trying to prepare samples with 1.0

wt.%, the viscosity increased greatly, and the samples ended up with many defects. Even applying 0.5 wt.% the viscosity was much higher than for the other CNTs. Other options of processing could be tried to reach higher weight concentration in future studies. The other CNTs were tested with 1.0 wt.% in this test batch.

Figure 83 shows the tensile specimens prepared for testing. The protocol applied for processing them provided relatively good homogeneity and no visual defects, although some voids and CNT clusters were found during microscopy analysis. Further information about dispersion is presented in next section.

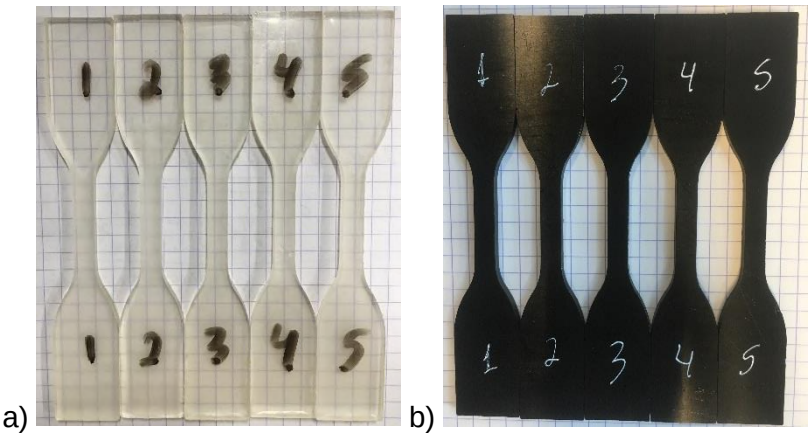

Figure 83 – Tensile samples: a) Neat epoxy, b) Toughened MWCNT epoxy.

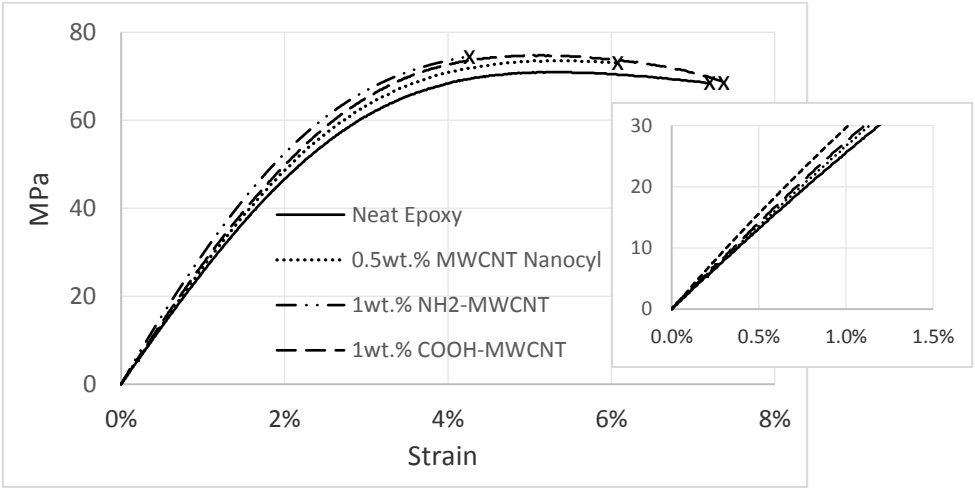

Figure 84 – Stress-strain curves from tensile tests of with neat and toughened MWCNTs epoxies.

By analyzing the graph from Figure 84, it is noted that toughened epoxies, especially NH_2- and COOH-MWCNTs with 1.0 wt.%, confirmed an increase up to 15% of tensile modulus and slight improvement of UTS. Although NH_2-MWCNT composite provided the

highest modulus, it has decreased almost in half the original elongation to rupture. There are some potential reasons for this behavior: NH_2-MWCNTs has larger aspect ratio due to the higher length (50µm), therefore it might have toughened too much the matrix becoming it brittle. Furthermore, the higher is the CNTs aspect ratio the more difficult to disperse them. Thus, it might have had more clusters than the other composites, which could facilitate premature failure. This subject is better discussed after fracture microscopy that is presented in section 6.2.2. Another option is that NH_2 functional groups could have provided better bonding to epoxy monomers due to larger quantity of these functional groups.

COOH-MWCNT composite samples in the other hand, guaranteed certain increasing of modulus without losing elongation, which generally confirms an increase in toughness. Figure 85 summarizes the tensile modulus of this tension batch. The result found in for the neat epoxy was coherent with properties given by supplier.

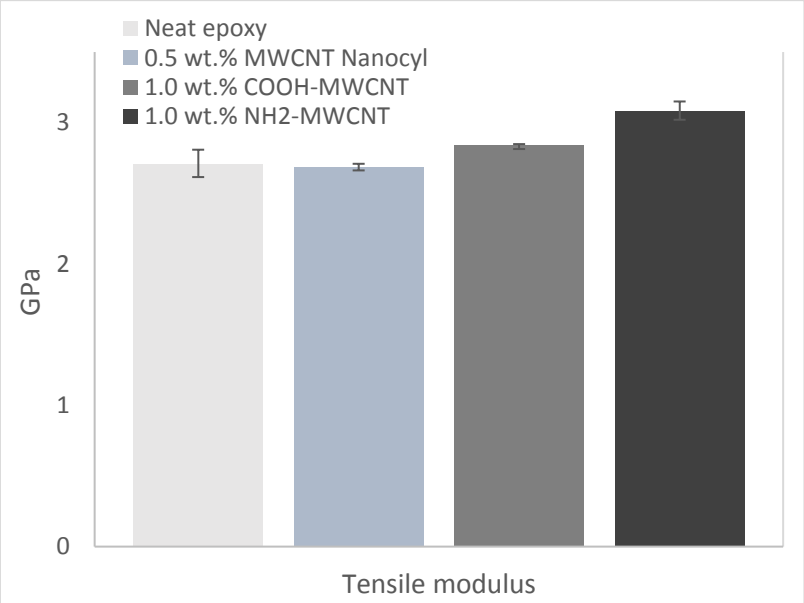

Figure 85 – Tensile modulus of neat and toughened MWCNTs epoxies.

As explained in the beginning of this section, second batch of tension and compressive tests were carried out with non-functionalized MWCNTs and COOH-MWCNTs with 0.5 wt.% and 1.0 wt.%. Then, 1.0 wt.% COOH-MWCNT composite was taken for the further tests.

Table 8 summarizes all tests performed with toughened and neat epoxy, and with CFA-epoxy system.

Table 8 – Summary of test results with standard deviations from neat and MWCNTs toughened epoxy samples, with CNT concentrations of 0.5 wt.% and 1.0 wt.%.

Test / Unit	Property / Unit	Neat epoxy	0.5 wt.% MWCNT	0.5 wt.% COOH-MWCNT	1.0 wt.% COOH-MWCNT
Tensile (*MPa*)	Strength	$75.2_{\pm 0.9}$	$77.8_{\pm 1.2}$	$72.0_{\pm 0.9}$	$76.4_{\pm 0.8}$
	Modulus	$2950_{\pm 75}$	$2900_{\pm 30}$	$3000_{\pm 30}$	$3350_{\pm 100}$
	Strain	$5.4\%_{\pm 0.5}$	$5{,}0\%_{\pm 0.3}$	$5.9\%_{\pm 0.8}$	$5.3\%_{\pm 0.6}$
Compressive (*MPa*)	Strength	$97_{\pm 0.9}$	$100_{\pm 0.8}$	$98_{\pm 0.0}$	$102_{\pm 0.7}$
	Modulus	$2300_{\pm 130}$	$2480_{\pm 150}$	$3110_{\pm 80}$	$3360_{\pm 180}$
Fracture toughness	($MPa.m^{0.5}$)	$1.07_{\pm 0.18}$	-	-	$1.02_{\pm 0.05}$
Lap shear (*MPa*)	Strength	$26.8_{\pm 5}$	-	-	$31.6_{\pm 3}$
Double cantilever beam	G_{1c} (J/m^2)	$114_{\pm 24}$	-	-	$141_{\pm 18}$
	G_{2c} (J/m^2)	$27_{\pm 5}$	-	-	$33_{\pm 4}$
	G_c (J/m^2)	$141_{\pm 30}$	-	-	$174_{\pm 21}$

According to the table, although the addition of 0.5 wt.% MWCNTs did not provide expressive changes on epoxy properties, the composite with 1.0 wt.% COOH-MWCNT confirmed an increase in some mechanical properties. Tensile modulus and debonding toughness, which are primordial parameters for transferring and withstand the CFA loads in the anchoring system, reached nominal improvement of 14% and 23%, respectively. Moreover, no significant brittle behavior of the epoxy was observed.

Regarding the 0.5 wt.% MWCNT and 1.0 wt.% COOH-MWCNT, the elongation had negligible decrease and the tensile and compressive strengths remained almost the same, still with a small gain. In addition, the compressive modulus increased 46% with 1.0%wt COOH-MWCNT. Note that using contact extensometer for measuring compressive modulus of materials that reach large deformation gave results with greater scattering than for the other tests and properties. Thus, it can be qualitatively concluded that there was, in fact, an improvement in compressive modulus, however with caution to mention it quantitatively.

A different behavior has been identified for the 0.5 wt.% COOH-MWCNT samples. It gave smaller UTS and slight bigger elongation. This could be explained by eventual higher concentration of CNT clusters or some mistake done during the processing of the

composite. It might be the same reason 1.0 wt.% MWCNT did not give improvement either.

Figure 86 shows the stress-strain curves of the tensile tests and the following other figures present in this sequence: the compressive samples (Figure 87), graph summarizing compressive modulus (Figure 88) and the stress-strain curve from compressive tests of neat and most toughened MWCNT epoxy (Figure 89).

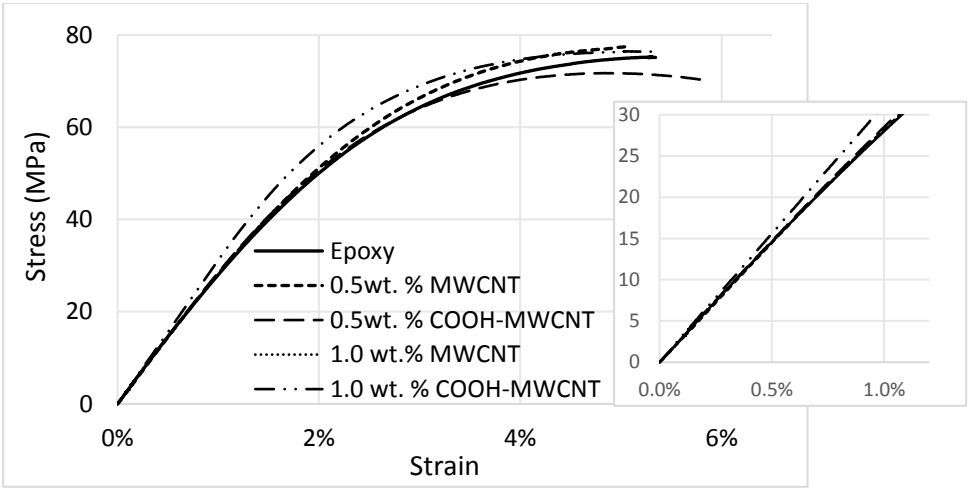

Figure 86 – Stress-strain curves of tensile tests with neat and toughened MWCNTs epoxies.

a)

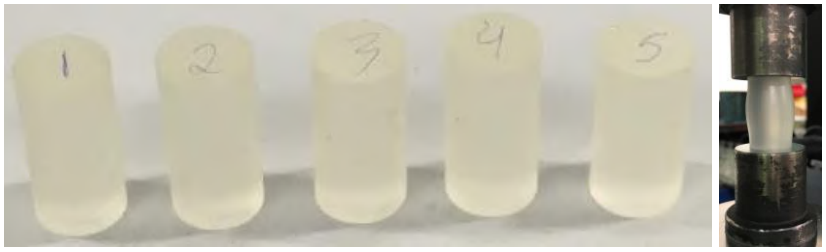

b)

Figure 87 – Compressive samples before and after testing: a) Neat epoxy, b) Toughened MWCNT epoxy.

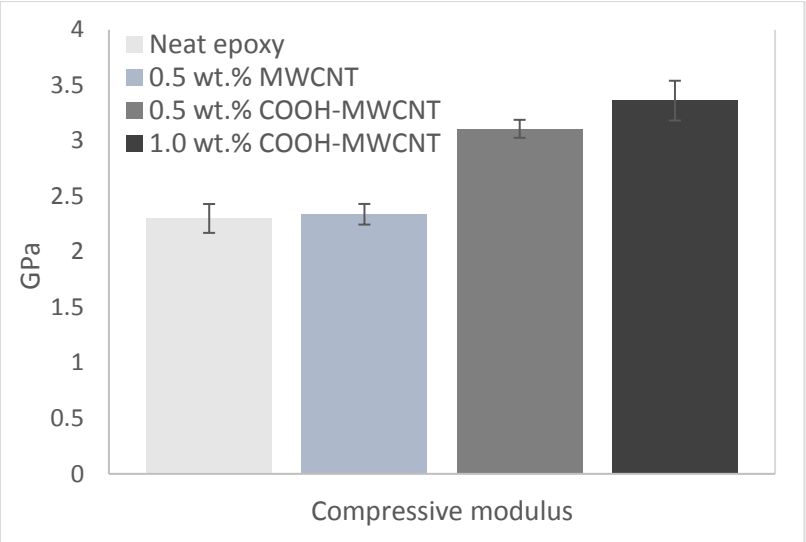

Figure 88 – Compressive modulus of neat and toughened MWCNTs epoxies.

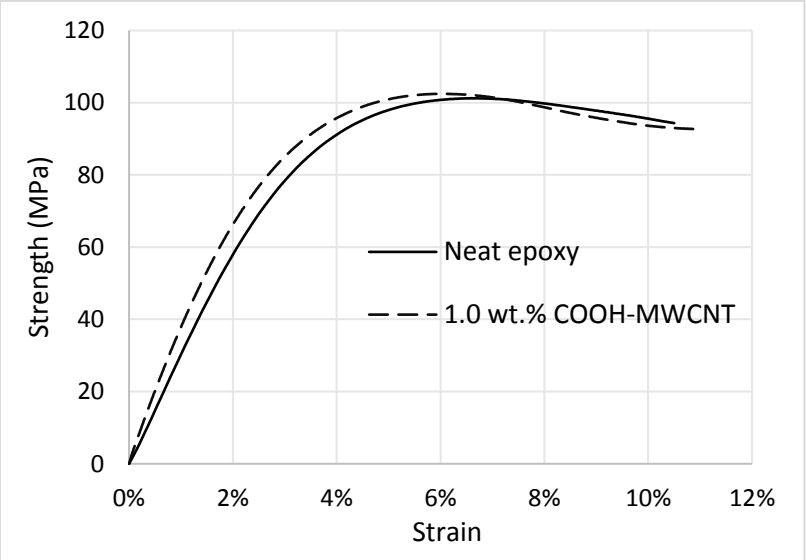

Figure 89 – Stress-strain curve from compressive tests of neat and most toughened MWCNT epoxy.

Although tensile and compressive tests indicated an increase of toughness, results from crack propagation test did not show much change in fracture toughness. In fact, this kind of test tends to be more sensitive to micro defects or eventual CNT clusters since they create spots of stress concentration, which is the base for crack propagation, as presented in section 2.3.2. Indeed, Figure 90 evidences some defects on the external surface of neat and toughened samples that might have impacted on the results.

By the way, no similar voids were found, at least visually, in the volume of the samples. Figure 91 presents the crack surfaces of samples from Fracture toughness tests. Only

four samples were considered in this case because one sample from each material had crack propagation in wrong path.

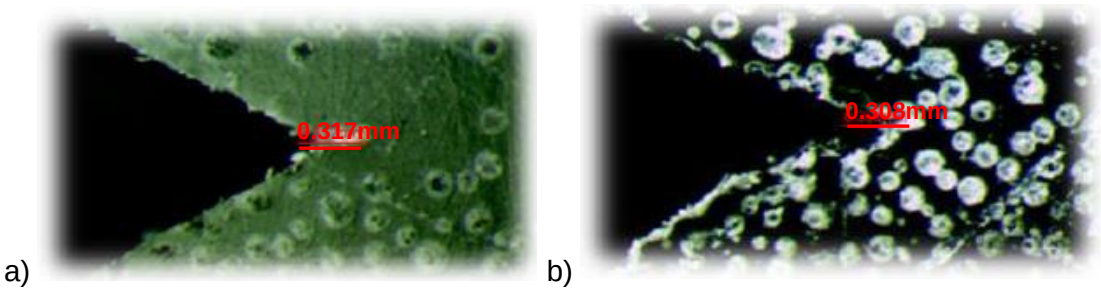

a) b)

Figure 90 – Crack tip from samples prior testing showing voids at external surface: a) Neat epoxy, b) 1.0 wt.% COOH-MWCNT epoxy.

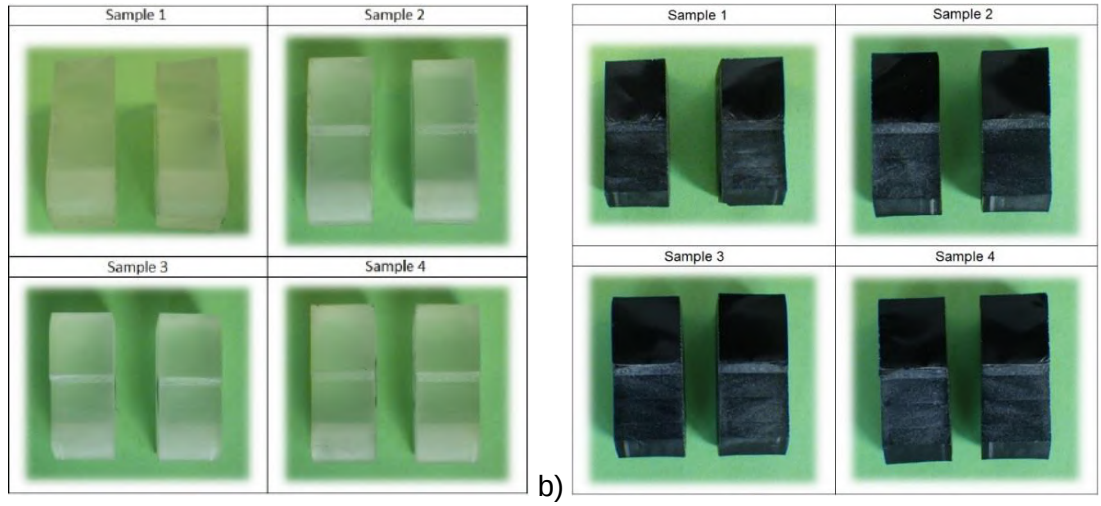

a) b)

Figure 91 – Surfaces of Fracture toughness samples: a) Neat epoxy, b) 1.0 wt.% COOH-MWCNT epoxy.

Regarding results from tests with CFAs from Table 8, toughened epoxy confirmed an increase in adhesion properties when compared to neat epoxy.

The shear strength reached an improvement of 18% through lap shear tests. However, by analyzing Figure 93, it is noted that the rupture of the specimens was not cohesive or adhesive, they occurred at the first ply of the CFA, that is at Mat level. Therefore, having greater shearing results with carbon nanotubes could be explained by the fact that they toughened the adhesive and the shear stresses were more equally distributed along the bonded surface, even up to substrate level. The following pictures show the lap shear samples before and after testing.

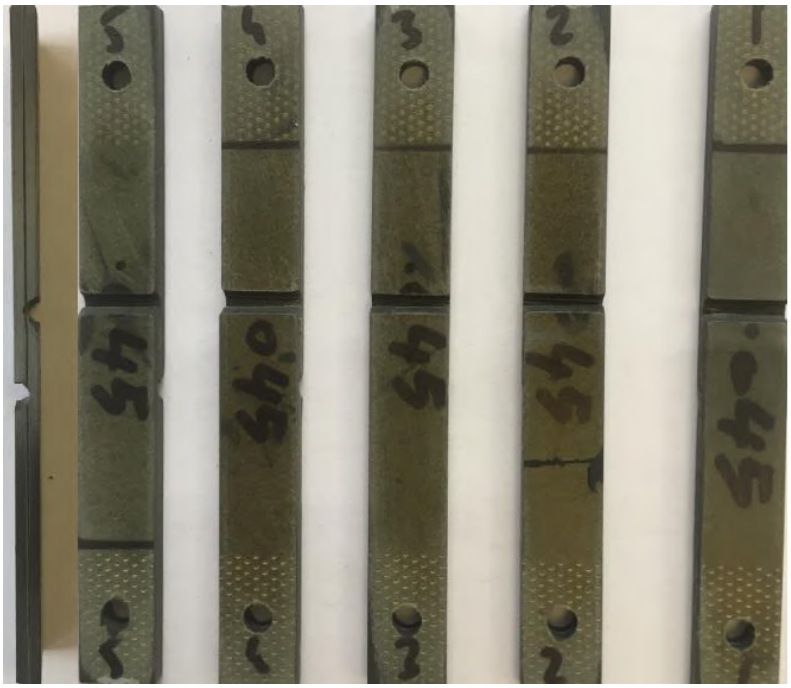

Figure 92 – Lap shear samples before testing. Side view of one CFA on the left showing the thicknesses of CFA and epoxy adhesive film.

Figure 93 – Lap shear samples after testing showing fracture surfaces at the bottom of picture. Rupture in substrate, at the first ply of the CFA, that is at Mat level.

All debonding toughness, mixed mode G_c, and modes I and II increased between 22% and 24%. Nevertheless, it is important to highlight that results presented big scatter between samples, as evidenced in the following graph, Figure 94. It could be linked to the repeatability of the protocol for preparing the samples. Figure 95a) shows an example of sample prior testing and Figure 95b) the device used. According to Figure 96, fracture initiation was at adhesive level in all neat epoxy samples and in two of toughened epoxy's. The other ruptures occurred at substrate level.

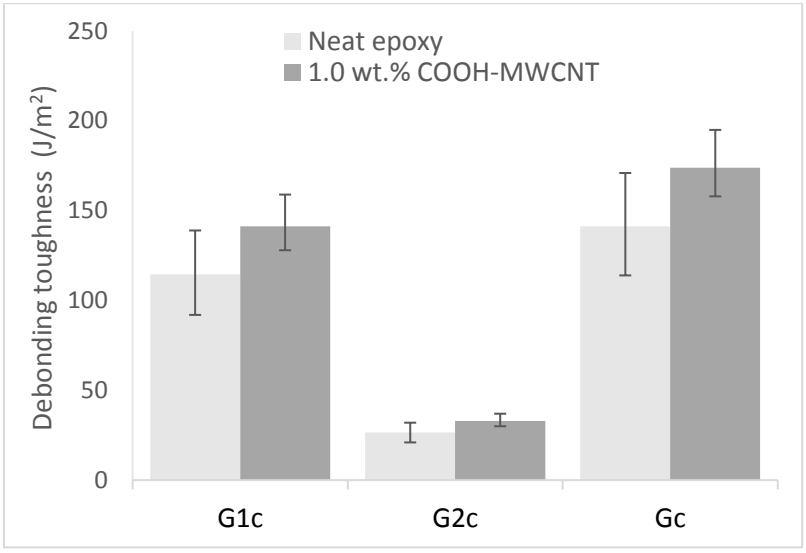

Figure 94 – Debonding toughness in Modes 1, 2 and Mixed of CFA-epoxy system, with neat and toughened 1.0 wt.% COOH-MWCNTs epoxies.

a) 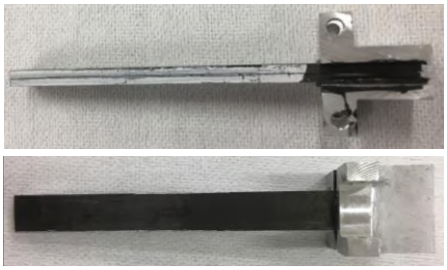 b) 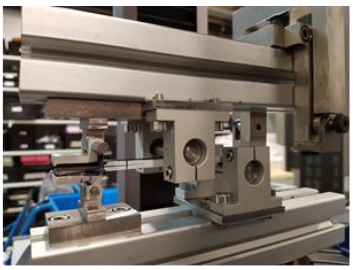

Figure 95 – a) Debonding toughness sample and b) testing device.

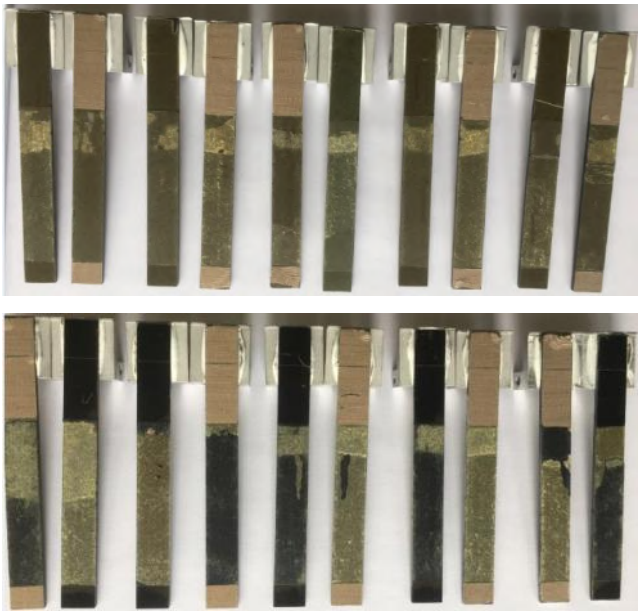

Figure 96 – Debonding toughness samples – Fracture surfaces: a) Neat epoxy, b) COOH-MWCNT epoxy.

The improvement of epoxy properties by toughening with carbon nanotubes has been proven through most of performed tests. It has provided greater behavior under tension, compression, shear and debonding energy. And these properties are quite important for the CFA-epoxy anchoring system, as demonstrated by the pull-out failure model.

Though, results were not as high as expected, if compared to the gain of 59% in tensile modulus presented by in section 2.2.4.3, or 72% in tensile strength and 124% in fracture toughness confirmed by ALAMRY *et al.* [52], for instance.

There are some parameters that might have impacted on final results which could be studied more deeply in future works. For example, the crosslinking with CNTs may be different with another type of epoxy and/or hardener; And other variables like the length and aspect ratio of nanotubes and particularly the protocol of material processing.

As mentioned in previous sections, assuring good CNT dispersion and eliminating voids in matrix should help to reach even better mechanical results. Therefore, next section summarizes some microscopy analysis performed with toughened materials to verify the dispersion of nanotubes and eventual defects.

6.2.2. CNT dispersion – Optical microscopy and SEM

Some optical microscopy and SEM analysis were carried out with some of toughened epoxy materials from tensile samples to characterize the fracture surface, verify eventual defects and CNT dispersion. Then, this last parameter was used to compare the two mixing methods, three roll mill and ultrasonication.

Figure 97 presents four images of the optical microscopy made from epoxy with MWCNT from *Nanocyl*®. Images done by SEM were not conclusive. The fracture has initiated from a micro bubble at the corner with around 50µm diameter. It had small mirrored area at the rupture initiation, then mainly dominated by brittle behavior. The voids could be explained by the fact it had higher viscosity than the other materials due to morphology and viscosity of this nanotube. Therefore, it was more difficulty to remove the micro bubbles even with the vacuum. In the other hand, no CNT clusters were found.

Apparently, the mixing method by ultrasonication used for this sample was effective for this type of CNT, even with high viscosity. It is important noting that it had the smallest aspect ratio (10ηm diameter and 1-2µm length), which might also have helped the dispersion. Even though, it did not provide much improvement in mechanical properties, as it was presented in previous section.

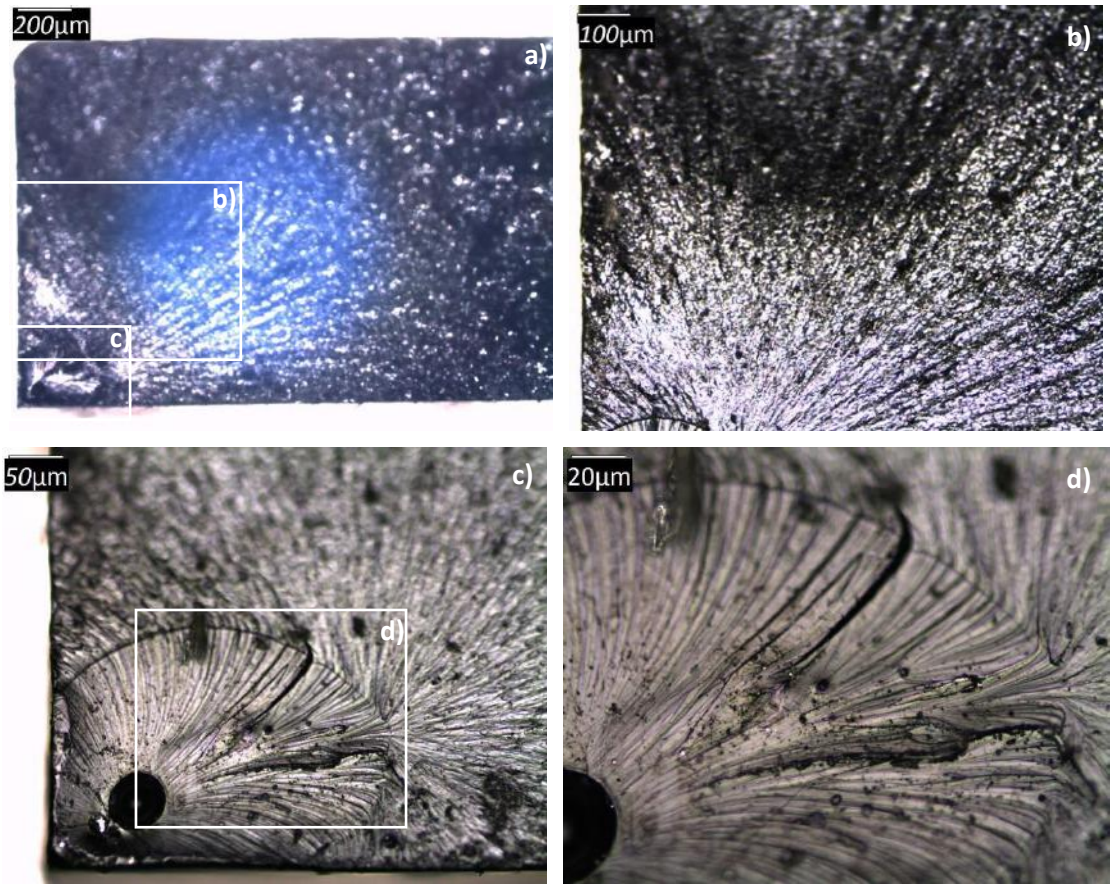

Figure 97 – Optical microscopy zoomed x2.5, x5, x10 and x20 of epoxy with MWCNT from *Nanocyl*®. Identifying presence of defect at the fracture initiation. CNTs dispersed by ultrasonication.

COOH-MWCNT samples was analyzed by SEM and optical microscopy and considering both mixing methods. Figure 98 shows two images from SEM of a piece from a region of the sample, that is relatively far from the rupture.

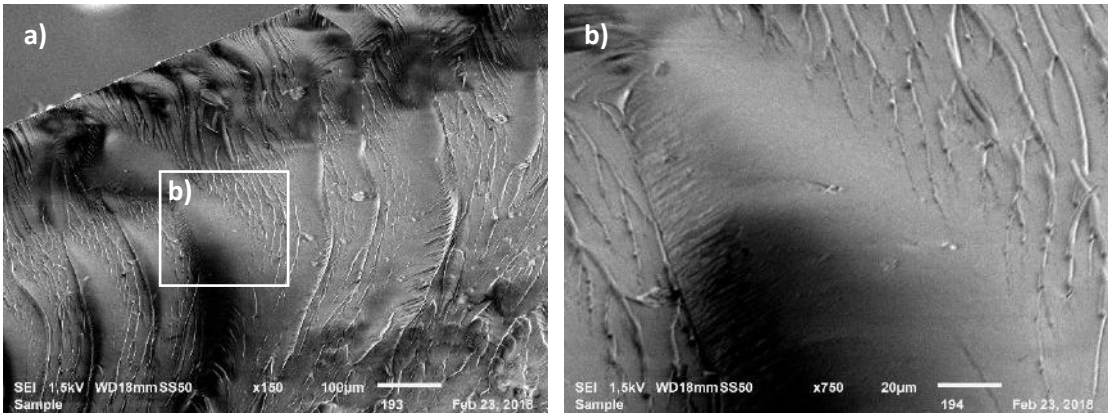

Figure 98 – SEM images showing from 1.0 wt.% COOH-MWCNT epoxy: a) x150, b) x750. CNTs dispersed by ultrasonication.

No CNT clusters were found in SEM images and structure showed relative good dispersion.

In the other hand, the optical microscopy performed at the fracture surface showed potential CNT clusters with 10µm to 20µm, including exactly at fracture initiation. See Figure 99. That means even for structures with well dispersed CNTs, small amounts of agglomerates can still be found, and may even drive the crack initiation.

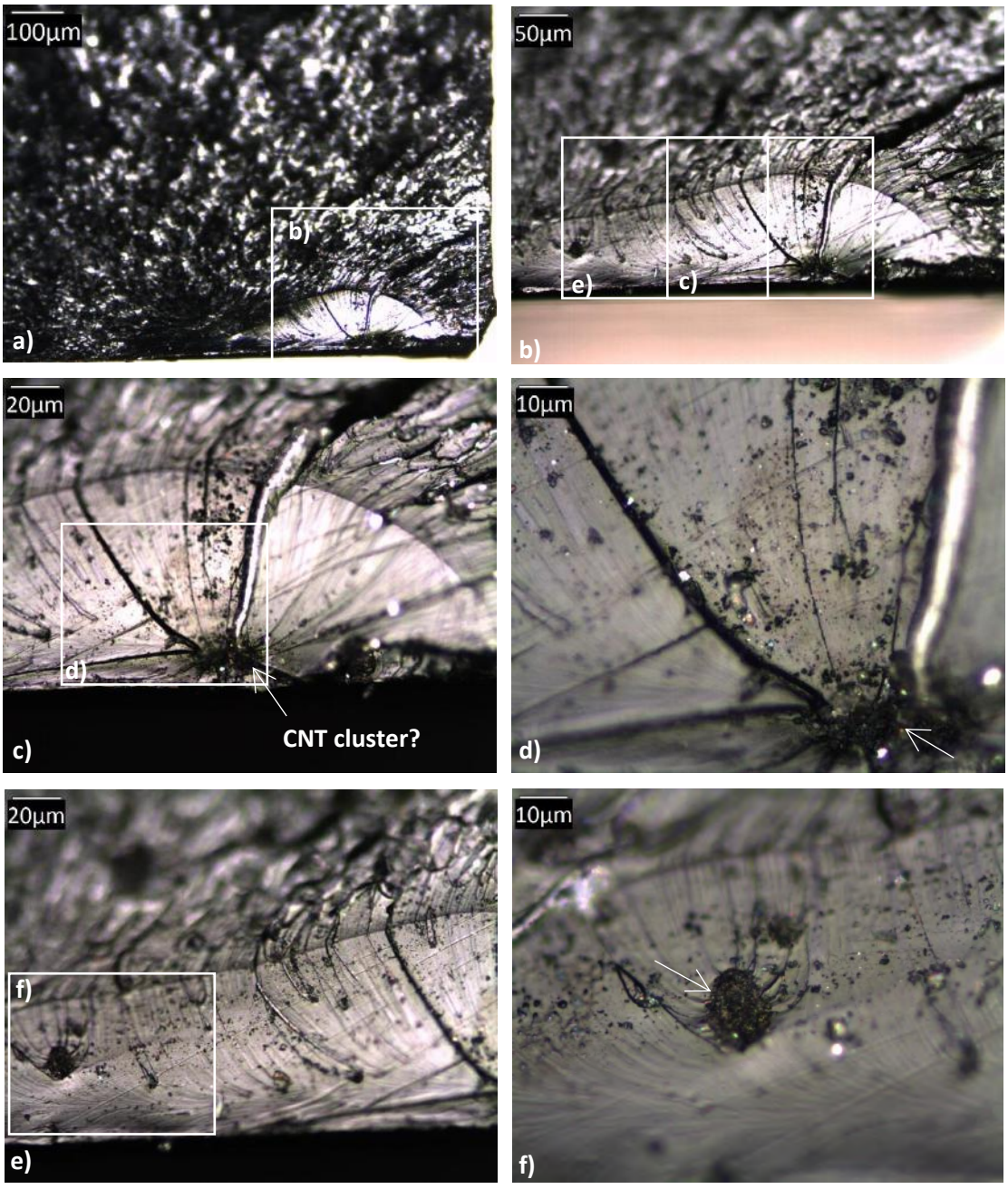

Figure 99 – Optical microscopy zoomed x5, x10, 20 and x50 of COOH-MWCNT epoxy. Identifying presence of CNT cluster at the fracture initiation. CNTs dispersed by ultrasonication.

Therefore, the fracture might have initiated from a CNT cluster with around 10µm diameter at the edge of the sample. It also had small mirrored area at the rupture initiation, then mainly dominated by brittle behavior. Only small voids have been observed, if compared to first samples.

The other samples of COOH-MWCNT, now dispersed by three roll mill, were then metallized for SEM analysis. Thus, the following figures present images of 0.5 wt.% and 1.0 wt.%.

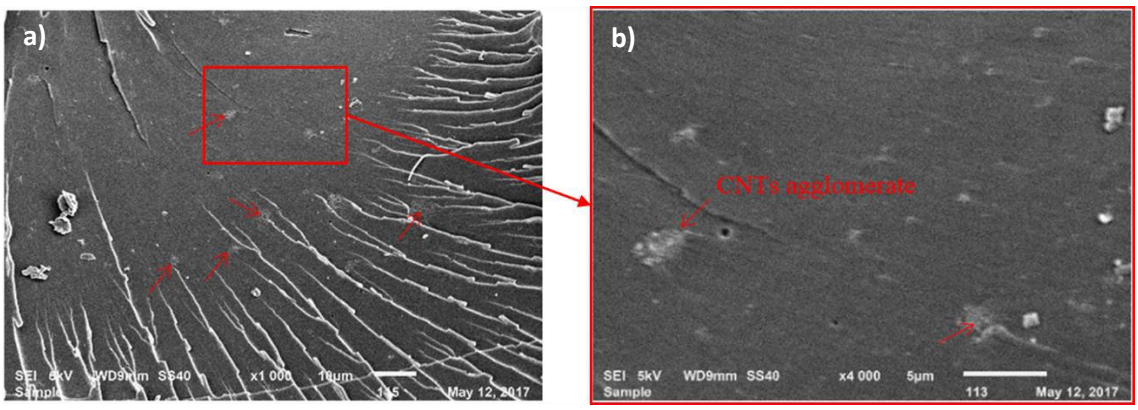

Figure 100 – SEM images showing dispersion of CNTs in the epoxy matrix: a) x1000 from 0.5 wt.% COOH-MWCNT; b) x4000 from 0.5 wt.% COOH-MWCNT. CNTs dispersed by three roll mill.

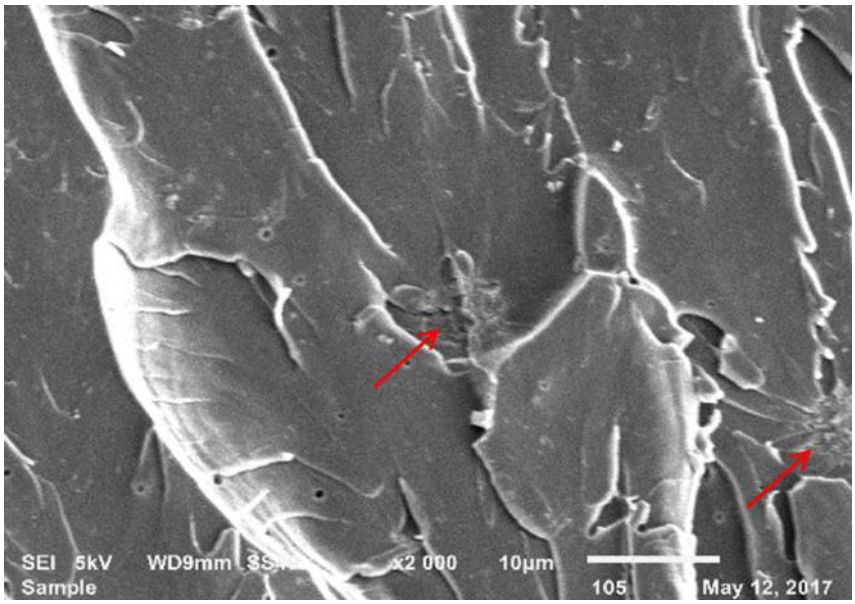

Figure 101 – SEM images x2000 from 1.0 wt.% COOH-MWCNT showing dispersion in the epoxy matrix. CNTs dispersed by three roll mill.

In Figure 100a), although it presents a relatively good dispersion, several CNTs clusters were found. Figure 100b) shows some of them zoomed. By inspecting the 1.0 wt.% COOH-MWCNTs sample, it was more difficult to find clusters, nevertheless Figure 101a) and b) show CNT clusters with approximately 5 to 10µm diameter, which is similar to the sizes found from ultrasonicated samples. Note that 5µm was the same gap used for the dispersion in the three-roll mill (minimum feasible from machine). Even if smaller gaps were possible in the three-roll mill, the setup (speed, gap and duration) could impact not only on the homogeneity of the dispersion but also on CNT structural integrity, that is, depending on configuration, it could break some of the nanotubes and the aspect ratio would be compromised.

By the way, considering the two COOH-MWCNTs samples mixed either by three-roll mill and ultrasonication, it appears both methods were effective with the chosen protocol. Indeed, they have provided similar mechanical results.

The last samples studied was the NH_2-MWCNT epoxy, mixed by ultrasonication. By analyzing the optical microscopy images from Figure 103 TEM images from Figure 102, it is clear the presence of CNT clusters. As per COOH-MWCNT, the fracture initiated from a CNT cluster, but with bigger sizes, with around 50µm diameter at the edge of sample. Different from the other materials, it did not have mirrored area at the rupture initiation, and mainly dominated by brittle behavior.

This information could explain the brittle behavior and premature rupture (with low elongation) found in tensile tests. The NH2-MWCNTs have highly toughened and the big CNT clusters contributed for propagating the crack as a defect.

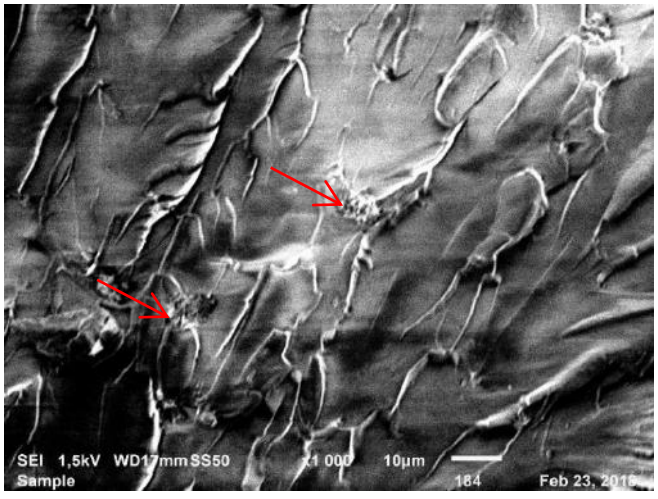

Figure 102 – SEM images showing from 1.0 wt.% NH_2-MWCNT epoxy with two potential CNT clusters: x1000. CNTs dispersed by ultrasonication.

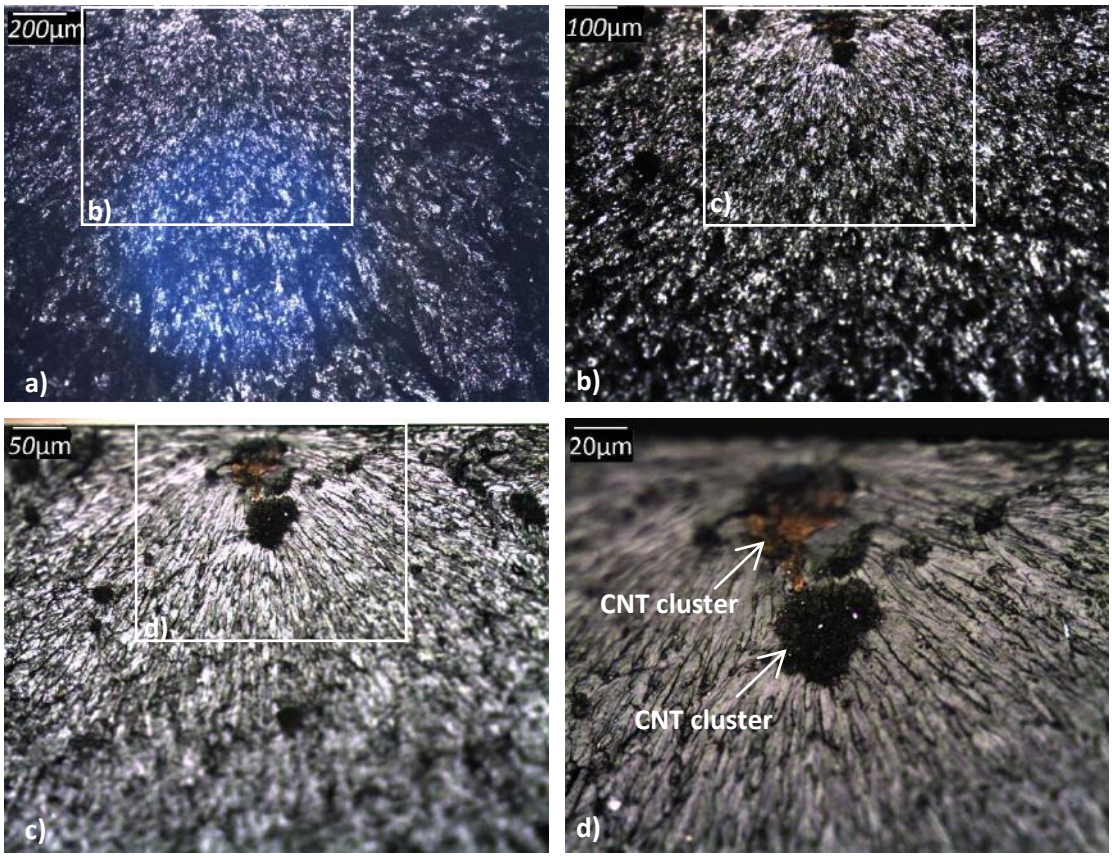

Figure 103 – Optical microscopy zoomed x2.5, x5, x10 and x20 of 1.0 wt.% NH_2-MWCNT epoxy. Identifying presence of CNT cluster at the fracture initiation. CNTs dispersed by ultrasonication.

6.2.3. CNTs morphology - TEM results

Knowing that carbon nanotubes can be very different from each other, some TEM analysis were done with three types, not yet mixed into the epoxy: MWCNT from *Nanocyl*®, COOH-MWCNT and NH_2-MWCNT from *TimesNano*®. The objective was to verify their morphology, size and number of walls, and to correlate to the mechanical test results.

The following two images were taken from MWCNT from *Nanocyl*®. Figure 104a) shows a CNT with seven walls relatively well aligned and continuous, and some amorphous phased carbons. Diameter was measured in a few CNTs and confirmed an average of 10±1ηm. Measuring the length was trickier because the nanotubes crossed each other making agglomerates, which made difficult to distinguish their extremities. However, lengths of at least 1µm were confirmed. These sizes were in accordance to information given by supplier.

In Figure 104b), it can be observed some heterogeneity in their morphology. A couple of CNTs had distorted form and less number of walls.

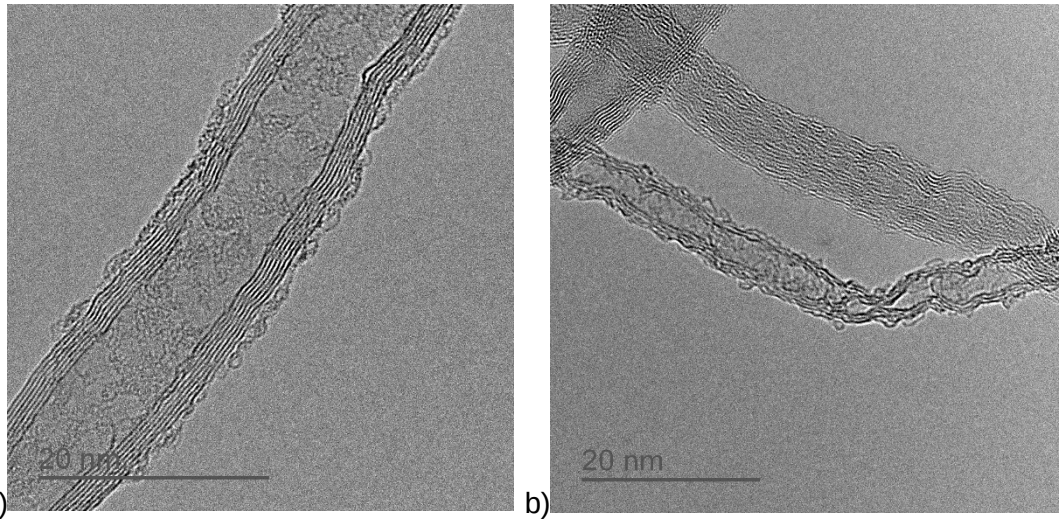

Figure 104 – TEM showing the walls and amorphous carbon phase of MWCNT from *Nanocyl*® supplier: a) Seven-wall CNT, b) Heterogenous CNTs morphology.

The images captured from COOH-MWCNTs confirmed relevant difference if compared to the first one analyzed. Although they were also well aligned and continuous, they had between seventeen and twenty walls, and average of 20±1ηm, see Figure 105. These sizes were in accordance to information given by supplier.

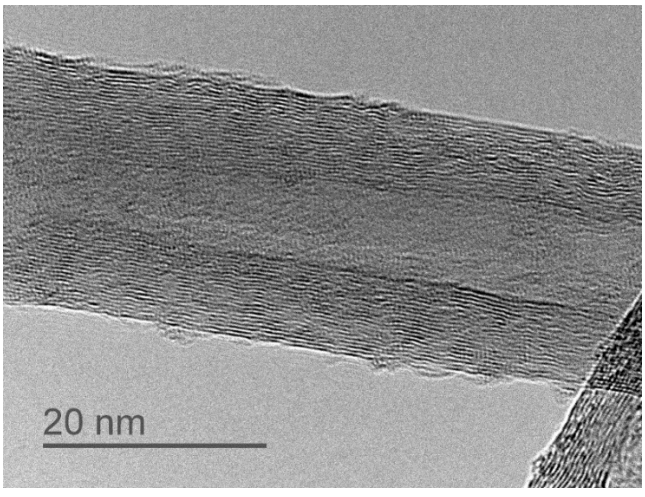

Figure 105 – TEM showing around twenty walls of functionalized COOH-MWCNT from *TimesNano*® supplier.

No heterogeneity was observed in morphology, however a large discrepancy in their lengths was identified. Figure 106 presents the CNTs well attached to the carbon grid used to collect the sample. Figure 106a) shows a longer CNT coming out from an

agglomerate, therefore it might have had at least 3µm length. While Figure 106b) confirmed some small lengths up to 1µm. According to supplier and to Table 6 from section 5.4.2, these nanotubes should have between 10 and 30µm. It could be explained by the fact that CNTs can be broken during covalent functionalization processing, as mentioned in section 2.2.4.3.

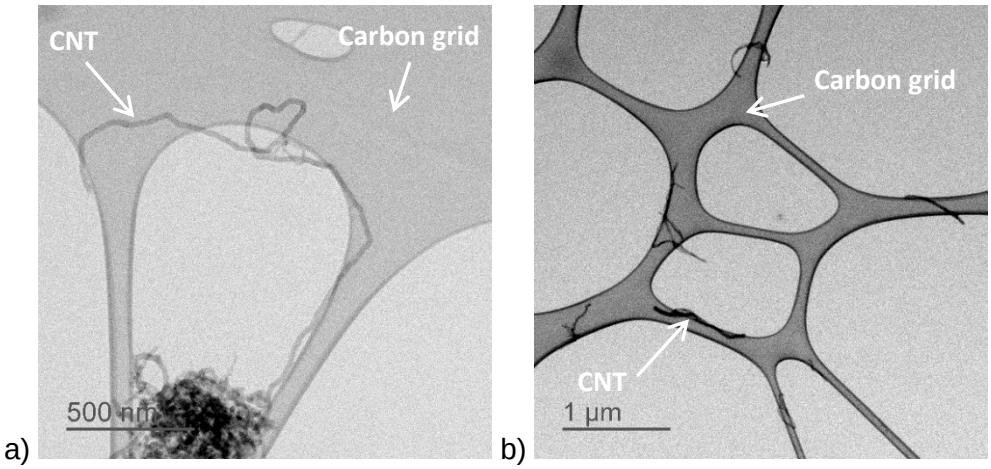

Figure 106 – TEM showing heterogenous lengths of COOH-MWCNT: a) Cluster with a long MWCNT, b) MWCNTs shorter than 1µm.

The third nanotube studied had good alignment and relatively homogenous morphology as well. But again, an important difference in geometry was observed. Although it had the same average 20ηm diameter of COOH-MWCNT, NH_2-MWCNTs presented higher number of walls, up to thirty. Furthermore, the largest lengths were confirmed with this CNT. Indeed, according to supplier, these nanotubes should have around 50µm. These information can be verified in Figure 107a) and b).

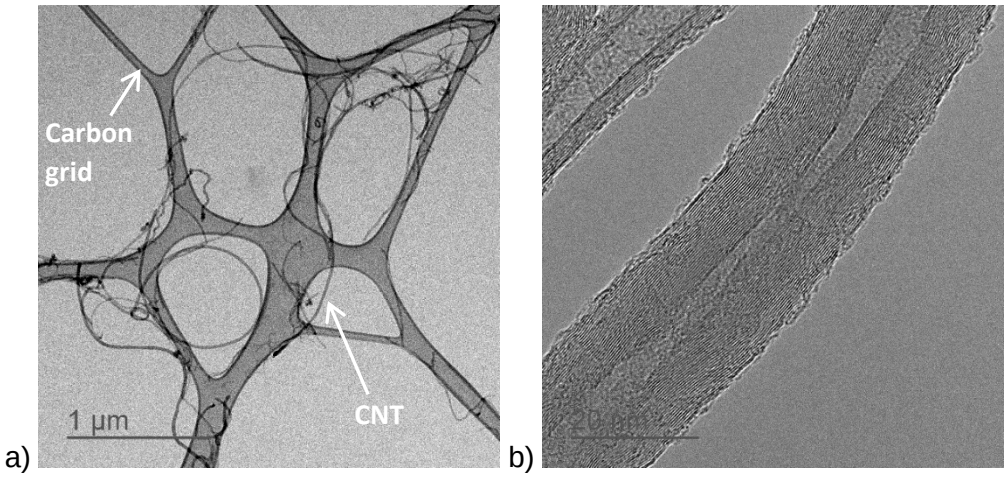

Figure 107 – TEM of NH_2-MWCNT from *TimesNano*® supplier: a) Confirming large length, b) showing a CNT with around thirty walls.

By analyzing all TEM images, some assumptions could be made when correlating to mechanical test results. The high increase of viscosity and consequent difficulty for eliminating voids identified during processing the first MWCNT may be related to the small number of walls (~7) and diameter (~10). According to a study performed by LAURENT *et al.* [103], this nanotube could have a density roughly 20% smaller than COOH-MWCNT used, as presented in the graph hereafter.

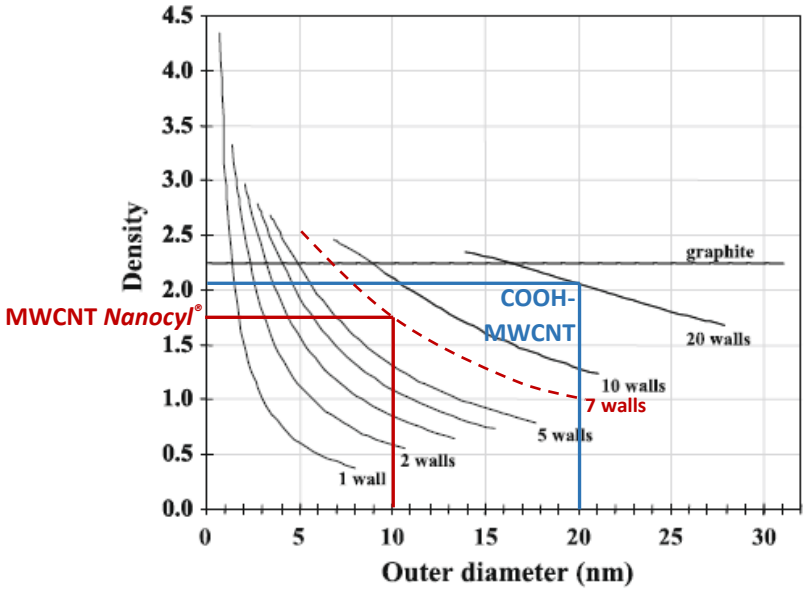

Figure 108 – Graph correlating CNT density to diameter and number of walls [103].

Regarding NH_2-MWCNTs, they seem to be more rigid than the others due to the high number of walls, which could explain the most brittle behavior found in the tensile tests Figure 84. Still, the bigger the length the harder is to untangle nanotubes, thus the length could justify the wide CNT clusters observed in microscopy since it had the largest length.

Therefore, although COOH-MWCNTs presented some split lengths, their general morphology could provide relatively low viscosity for helping eliminate voids and a moderate CNT dispersion, at least with smaller clusters than NH_2-MWCNT's.

6.2.4. Non-covalent functionalization of CNTs

This section summarizes the results of the non-covalent functionalization Melamine ($C_3H_6N_6$) conducted at the end of the research and proposed as potential option for improving even more epoxy mechanical properties. It is important to highlight that only tensile tests were carried out, which means that adhesion with CFA was not investigated here and therefore should be done in future works.

6.2.4.1. Effectiveness of treatment - EDX and XPS results

EDX analysis provided some preliminary information about the efficiency of the treatment by evaluating the presence of nitrogen at the CNT surface. Nevertheless, the results by themselves were not conclusive since it seemed that it captured false signals, out of the nanotubes, as shown in HAADF cartographies in Figure 109, Figure 111 and Figure 113. Then, a cross-checking with XPS data allowed to select which material might had had the most effective non-covalent functionalization.

The following figures present the results of EDX and XPS performed with three types of nanotubes before and after non-covalent functionalization: MWCNT from *Nanocyl*®, COOH-MWCNT and NH_2-MWCNT. The effectiveness of the treatment was evaluated by verifying the increase the atomic concentration of nitrogen at the surface of CNTs. It is important to highlight that both methods present some dispersion, therefore the analysis were more comparative between materials rather seeking absolute values.

For the first CNT, although EDX spectrum table informs that concentration of nitrogen slightly increased with the functionalization, the cartography shows that some signals were caught outside of nanotubes. Indeed, when verifying XPS table, the gain of nitrogen seems to be negligible. Another point observed was the atomic concentration of oxygen. EDX and XPS registered opposite results. While the first identified reduction, the second reported raising.

a)

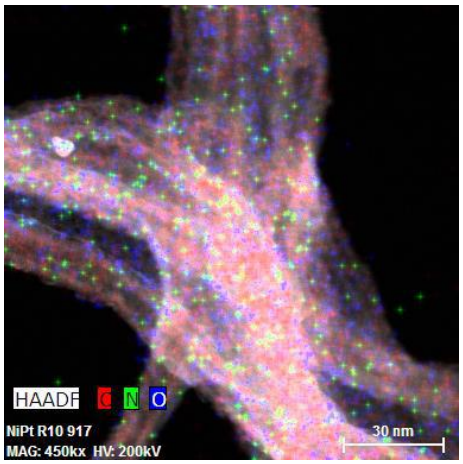

b)

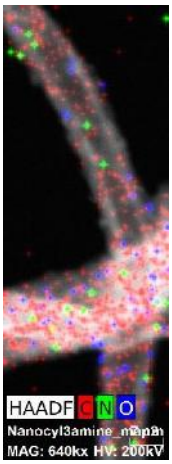

Spectrum: 1

El	AN	Series	Net unn. C [wt.%]	norm. C [wt.%]	Atom. C [at.%]	Error (1 Sigma) [wt.%]
C	6	K-series	7125	83.85	83.85	87.04	2.73
O	8	K-series	1078	12.72	12.72	9.91	0.57
N	7	K-series	76	3.43	3.43	3.05	0.43
Total:				100.00	100.00	100.00	

Spectrum: 1

El	AN	Series	Net unn. C [wt.%]	norm. C [wt.%]	Atom. C [at.%]	Error (1 Sigma) [wt.%]
C	6	K-series	536	86.63	86.63	89.08	4.58
O	8	K-series	44	7.93	7.93	6.12	1.23
N	7	K-series	8	5.44	5.44	4.79	1.95
Total:				100.00	100.00	100.00	

Figure 109 – EDX cartography of C, N and O elements from MWCNT *Nanocyl*®: a) Without treatment, b) with Melamine ($C_3H_6N_6$) non-covalent functionalization.

a)

Peaks

Name	Peak BE	FWHM eV	Area (P) CPS.eV	Atomic %	Q
C1s	284.39	0.84	180318.55	65.90	Yes
C1s A	285.40	1.31	43404.98	15.87	Yes
C1s B	286.71	1.28	15038.48	5.50	Yes
C1s C	288.20	1.57	11304.14	4.14	Yes
C1s D	289.90	1.42	7759.73	2.85	Yes
C1s E	291.30	1.89	10589.08	3.89	Yes
N1s	399.60	0.95	1719.29	0.40	Yes
O1s	532.58	2.86	9487.91	1.44	Yes

b)

Peaks

Name	Peak BE	FWHM eV	Area (P) CPS.eV	Atomic %	Q
C1s	284.41	0.83	187253.00	63.30	Yes
C1s A	285.39	1.22	37294.11	12.61	Yes
C1s B	286.60	1.38	20570.63	6.96	Yes
C1s C	288.23	1.56	12871.10	4.36	Yes
C1s D	289.70	1.44	7846.53	2.66	Yes
C1s E	291.30	1.89	13244.26	4.50	Yes
N1s	399.83	2.01	2561.51	0.56	Yes
O1s	532.34	4.16	32817.48	4.59	Yes

Figure 110 – XPS results from *Nanocyl*® MWCNT: a) Without treatment, b) with Melamine ($C_3H_6N_6$) non-covalent functionalization.

Now, regarding COOH-MWCNT results from EDX and XPS, both confirmed an increase of nitrogen atomic concentration, although the second method identified a greater value, up to 4.72%.

A large concentration of oxygen has been observed through XPS in this CNT prior to the treatment, which could be explained by the COOH- covalent functionalization. However, a huge drop of this value was reported after treating with Melamine. Possibly the procedure might have broken some COOH- bonds or either created Amide (CO-NH) groups in the structure.

a)

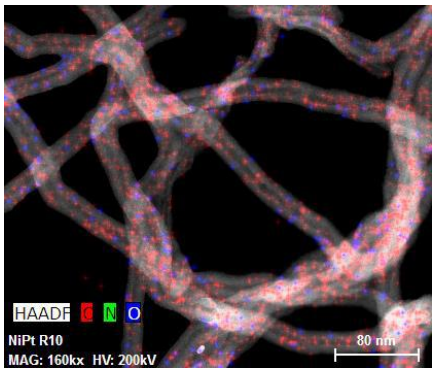

Spectrum: 1

El	AN	Series	Net unn. C [wt.%]	norm. C [wt.%]	Atom. C [at.%]	Error (1 Sigma) [wt.%]
C	6	K-series	1593	86.44	86.44	89.06	3.40
O	8	K-series	164	9.49	9.49	7.34	0.82
N	7	K-series	17	4.08	4.08	3.60	0.99
Total:				100.00	100.00	100.00	

b)

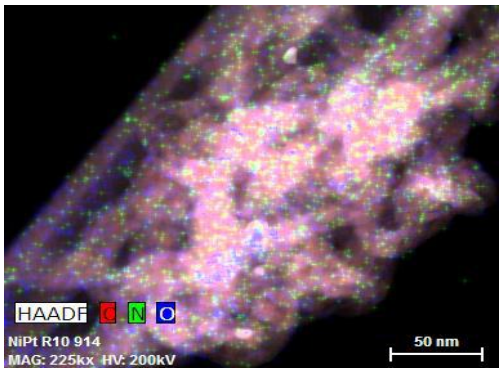

Spectrum: 1

El	AN	Series	Net unn. C [wt.%]	norm. C [wt.%]	Atom. C [at.%]	Error (1 Sigma) [wt.%]
C	6	K-series	36876	88.55	88.55	90.55	2.72
N	7	K-series	572	6.11	6.11	5.35	0.34
O	8	K-series	1951	5.34	5.34	4.10	0.23
Total:				100.00	100.00	100.00	

Figure 111 – EDX cartography of C, N and O elements from functionalized COOH-MWCNT: a) Without treatment, b) with $C_3H_6N_6$ non-covalent functionalization.

a)

Peaks

Name	Peak BE	FWHM eV	Area (P) CPS.eV	Atomic %	Q
C1s	284.29	0.86	13009.04	5.76	Yes
C1s A	285.29	1.17	107261.72	47.51	Yes
C1s B	286.55	1.19	4312.22	1.91	Yes
N1s	399.20	0.19	508.53	0.15	Yes
O1s	532.84	1.18	119347.62	21.88	Yes

b)

Peaks

Name	Peak BE	FWHM eV	Area (P) CPS.eV	Atomic %	Q
C1s	284.43	0.79	168048.74	57.74	Yes
C1s A	285.41	1.20	40250.35	13.84	Yes
C1s B	286.60	1.43	18809.46	6.47	Yes
C1s C	288.16	1.73	17026.46	5.86	Yes
C1s D	289.70	1.32	5905.72	2.04	Yes
C1s E	291.30	1.73	10039.47	3.46	Yes
N1s	398.96	2.41	22002.46	4.87	Yes
O1s	532.19	4.05	36054.83	5.13	Yes

Figure 112 – XPS results from functionalized COOH-MWCNT: a) Without treatment, b) with Melamine ($C_3H_6N_6$) non-covalent functionalization.

Finally, by analyzing NH_2-MWCNT, EDX registered small loss of N and O atomic concentration, while XPS reported negligible raise of N and big drop of O. Therefore, if considering only the increase of N, and comparing to COOH-MWCNT, it seemed to be less effective.

a)

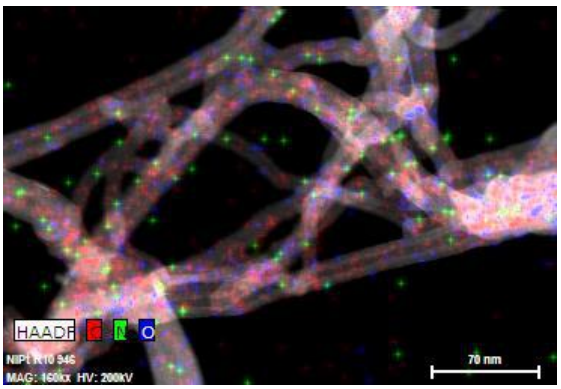

Spectrum: Spec2.xls

El	AN	Series	Net unn. C [wt.%]	norm. C [wt.%]	Atom. C [at.%]	Error (1 Sigma) [wt.%]
C	6	K-series	1933	81.21	81.21	84.66	3.08
O	8	K-series	309	13.00	13.00	10.17	0.86
N	7	K-series	38	5.79	5.79	5.17	0.98
Total:				100.00	100.00	100.00	

b)

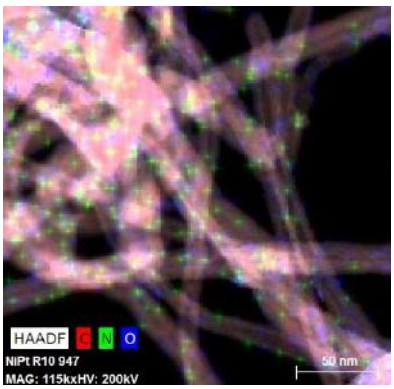

Spectrum: 1

El	AN	Series	Net unn. C [wt.%]	norm. C [wt.%]	Atom. C [at.%]	Error (1 Sigma) [wt.%]
C	6	K-series	6534	89.29	89.29	91.30	2.92
O	8	K-series	414	6.32	6.32	4.85	0.39
N	7	K-series	74	4.39	4.39	3.85	0.55
Total:				100.00	100.00	100.00	

Figure 113 – EDX cartography of C, N and O elements from functionalized NH_2-MWCNT: a) Without treatment, b) with Melamine ($C_3H_6N_6$) non-covalent functionalization.

a)

Peaks					
Name	Peak BE	FWHM eV	Area (P) CPS.eV	Atomic %	Q
C1s	284.42	0.89	159013.01	56.31	Yes
C1s A	285.42	1.18	32905.52	11.66	Yes
C1s B	286.60	1.37	17226.00	6.11	Yes
C1s C	288.23	1.56	9695.97	3.44	Yes
C1s D	289.70	1.36	5434.84	1.93	Yes
C1s E	291.30	2.06	9404.76	3.35	Yes
N1s	399.78	2.72	4266.12	0.97	Yes
O1s	532.87	3.06	82298.14	12.07	Yes

b)

Peaks					
Name	Peak BE	FWHM eV	Area (P) CPS.eV	Atomic %	Q
C1s	284.45	0.90	161908.46	59.35	Yes
C1s A	285.35	1.34	37802.52	13.86	Yes
C1s B	286.65	1.40	17696.33	6.50	Yes
C1s C	288.26	1.60	11393.64	4.19	Yes
C1s D	289.80	1.49	5573.10	2.05	Yes
C1s E	291.30	2.10	9633.24	3.55	Yes
N1s	399.38	2.61	7055.00	1.67	Yes
O1s	533.32	4.17	44918.25	6.82	Yes

Figure 114 – XPS results from functionalized NH_2-MWCNT: a) Without treatment, b) with Melamine ($C_3H_6N_6$) non-covalent functionalization.

Considering the data compiled from EDX and XPS, some results had some disparity when compared to each other. Variables such as the time settled for capturing EDX signals, eventual differences of CNTs surface oxidation due to XPS ultra-high vacuum or simply the treatment applied not reaching sufficiently π-π bonds, could be the raison. Anyway, since COOH-MWCNT showed greater effect to the functionalization, even if small, it was taken to tensile tests.

6.2.4.2. Tensile test results with COOH-MWCNT + $C_3H_6N_6$

After choosing the most effective functionalized composite according to EDX and XPS results, with COOH-MWCNT + $C_3H_6N_6$, its mechanical performance was evaluated

under tension. The stress-strain curves presented hereafter confirms the gain reached in tensile stress by treating COOH-MWCNTs with Melamine, which was ensured by the effectiveness of $C_3H_6N_6$ π-π bonds, even with apparent loss of some COOH- covalent functional groups.

By analyzing the graphs from Figure 115 and Figure 116, it can be seen an improvement of UTS up to 10% with small scattering, without losing toughness and by keeping the increase of tensile modulus already provided by COOH-MWCNT.

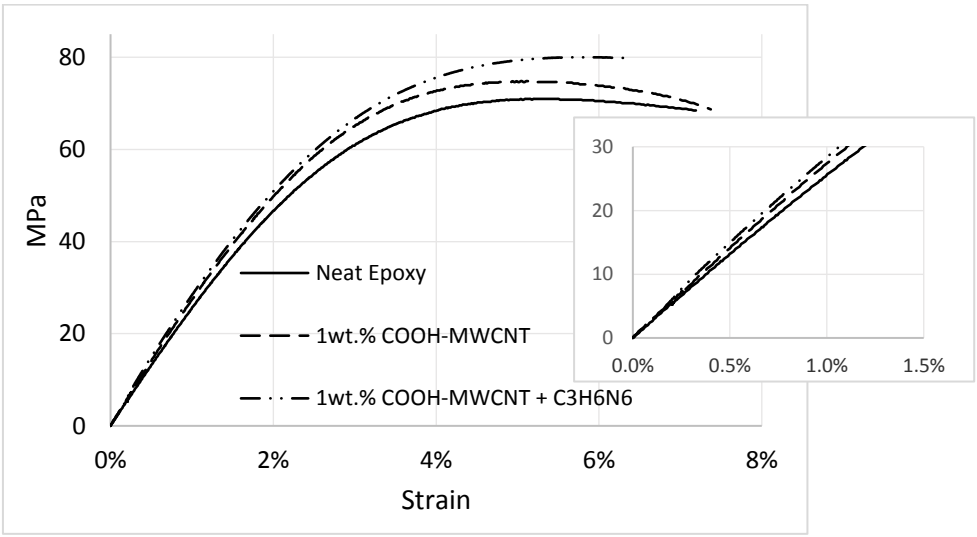

Figure 115 – Stress-strain curves from tensile tests of with neat, COOH-MWCNT and COOH-MWCNT + $C_3H_6N_6$ epoxies.

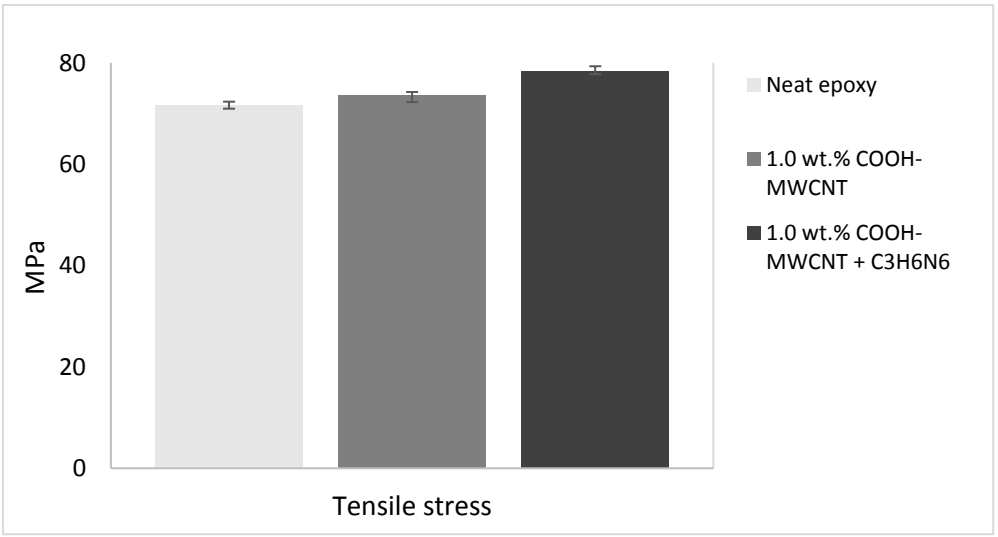

Figure 116 – Resume of tensile stresses with neat, COOH-MWCNT and COOH-MWCNT + $C_3H_6N_6$ epoxies.

Therefore, it can be concluded that performing non-covalent functionalization with $C_3H_6N_6$ π-π bonds raises the mechanical performance of the MWCNT toughened epoxy, even with a low effect treatment, as identified through EDX and XPS analysis. However, it must be noted that this kind of procedure is time-consuming, besides resulting small amounts of material at the end of protocol. Therefore, it should be considered only for cases in which improving UTS is necessary.

Adhesion to CFA was not evaluated and should be verified prior choosing it as solution, although it is also expected amelioration since $C_3H_6N_6$ groups could make π-π bonds to CFAs as well.

6.3. GAIN OF PULL-OUT RESISTANCE BY IMPROVING EPOXY

After studding the toughening of epoxy and evaluating the increasing of mechanical properties in section 6.2, the gain of anchoring resistance could be assessed by applying the data acquired from experiments to the pull-out failure model. It was possible to compare either the improvement of anchoring or the decrease of anchoring length for a given external force. This last approach might be important because it could be linked to the reduction of the EF size of flexible risers and therefore reduction of cost.

Therefore, the complete sensibility analysis, that is applying the gain of epoxy mechanical properties and adhesion to CFA, was performed with the neat and COOH-MWCNT toughened epoxies, since they were the materials taken for all mechanical tests.

Remembering the developed equation (129) of CFA pull-out from section 5.2.2:

$$F_d = \sqrt{2E_{CFA}G_cS_{CFA}P_{CFA}L\sqrt{c}\tanh(\sqrt{c}L)} \tag{134}$$

where E_{CFA}, S_{CFA} and P_{CFA} are the CFA longitudinal modulus, cross-section area and perimeter, respectively; G_c is the debonding energy, L is the anchoring length and c is given by the relation from ODE assessed in the development of formulation:

$$c = \frac{{n_{CFA}}^2}{S_{CFA}\int_0^D \frac{1}{P_E} dd} \tag{135}$$

P_E is the epoxy external perimeter and the dimensionless term ${n_{CFA}}^2$ is

$$n_{CFA}{}^2 = \frac{E_E}{2(1+\nu_E)E_{CFA}} \tag{136}$$

where E_E and ν_E are the epoxy tensile modulus and Poisson's coefficient, respectively.

Thus, considering that, by introducing carbon nanotubes, epoxy provided a nominal increase of 23% in debonding G_c and 14% in epoxy tensile modulus E_E, and considering Poisson's coefficient constant, the dimensionless term of CNT toughened epoxy is:

$$n_{CFA}{}^2_{CNT} = \frac{E_{E_{CNT}}}{2(1+\nu_E)E_{CFA}} = \frac{1.14E_E}{2(1+\nu_E)E_{CFA}} \tag{137}$$

And

$$c_{CNT} = \frac{n_{CFA}{}^2_{CNT}}{S_{CFA}\int_0^D \frac{1}{P_E}dd} = \frac{1.14E_E}{2(1+\nu_E)E_{CFA}} \tag{138}$$

Finally, applying c_{CNT} on equation (134) and considering $G_{c_{CNT}} = 1.23G_c$, the CFA pull-tout force $F_{d\,CNT}$ of COOH-WMCNT epoxy is

$$F_d = 1.62\sqrt{E_{CFA}G_cS_{CFA}P_{CFA}L\sqrt{c}\tanh(1.07\sqrt{c}L)} \tag{139}$$

Then, considering the epoxy and adhesion properties from Table 8 in section 6.2.1, the CFA data and anchoring geometry from Table 4, MWCNT toughened epoxy improved the anchoring resistance in 16%. See Figure 117.

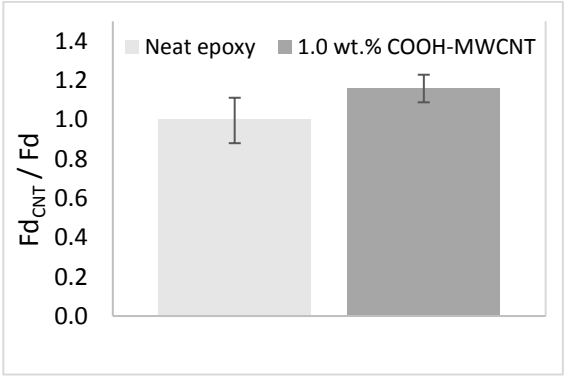

Figure 117 – Potential for increasing of anchoring resistance: Study with 1.0 wt.% COOH-MWCNT toughened epoxy.

Analogously, the anchoring length for a given external force would reduce at the same ratio since L is independent of epoxy and adhesion properties in formulation. Therefore, the EF length could be optimized and, consequently, it could shorten the cost.

By analyzing the elongation at the CFA-epoxy interface from equation (133) in section 6.1, it is inversely proportional to epoxy tensile modulus E_E. This means that raising this property without making the material brittle, besides reducing elongation while the system is under tension, it would mitigate the risk of creating fissures or crack propagation. Thus, MWCNT toughened epoxy gives more reliability to the structural integrity of CFA-epoxy system.

Summarizing, the increasing of properties confirmed in this work by introducing CNTs in epoxy already gives an improvement on CFA anchoring resistance. And, this information was properly proven by the developed pull-out failure analytical model.

Chapter 7 – Conclusions

The CFA-Epoxy anchoring system has been addressed in this work as a composite in which CFA is considered as reinforcement and epoxy as matrix. Then, the CFA pull-out failure model is developed, proposed and compared by FEM.

The analytical model presented small deviation from FEM model, therefore it can be a good approach for straight CFA pull-out studies instead of launching FEM which is time consuming. Moreover, it has also confirmed that improving epoxy mechanical and adhesion properties, in particular debonding energy, G_{2c}, and the epoxy tensile modulus, E_E, always followed by toughness, should increase the CFA pull-out resistance. Applying the improvements found in COOH-MWCNT toughened epoxy to the pull-out model already confirmed an order of magnitude of 16% increasing of Debonding Force, as presented in section 6.3. However, it is important to mention that for a complete amour anchoring assessment, other parameters like EF geometry and capstan effect due to the helicoidally organized tensile armors should be added to the system.

The tests with the MWCNTs filled toughened epoxy showed improvement of mechanical and adhesion properties, such as epoxy's tensile and compressive modulus and the debonding toughness of the CFA-epoxy system, particularly for the epoxy with 1.0 wt.% COOH-MWCNT. The strengths remained mostly unchanged and there was no significant decrease of strain especially with the functionalized nanotubes. In the other hand, composite samples with non-functionalized MWCNTs or with 0.5wt.% did not present any noticeable improvement for any CNT type or surface treatment.

The epoxy toughened with 1.0 wt.% NH_2-MWCNT also confirmed the increase of tensile modulus, nevertheless with important loss of strain. This behavior could be either due to -NH_2 functionalization or its high aspect ratio, if compared to the other MWCNTs studied.

Performing additional surface treatment of non-covalent functionalization with 50 wt.% $C_3H_6N_6$ on COOH-MWCNT epoxy confirmed an increase of UTS without losing strain, although it did not influence the tensile modulus. For the other carbon nanotubes, however, the treatment did not show much efficiency according to EDX and XPS analysis.

SEM analysis showed some CNT clusters even in the composite samples that showed the best performance, although matrices had relative good homogeneity in CNTs

dispersion. Both three roll milling and ultrasonication demonstrated similar performance for dispersing nanotubes.

TEM analysis confirmed substantial difference of morphology and number of walls between carbon nanotubes from *Nanocyl*® and *TimesNano*®. This last parameter was the most likely reason that MWCNT from *Nanocyl*® overly increased the epoxy viscosity and made its dispersion even more difficult. As mentioned in section 6.2.3, it had probably lower density due to the lower number of walls, therefore needed a higher volume fraction to reach the desired weight fraction. Note that, in this case, a composite having a higher volume fraction of reinforcement did not improve the mechanical properties because it brought also hard dispersion and probably more clusters and CNT-epoxy interface defects.

Therefore, the MWCNTs toughened composite for improving the anchoring of composite tensile armors of flexible risers confirmed a good potential for increasing the anchoring resistance of the system. And the same information has been proven by the developed model. Nevertheless, since there are several variables inherent to the material option and the composite processing, additional tests and parameters like CNTs type, dispersion, concentration and treatment, cure protocols and epoxy family shall be deeply assessed.

Chapter 8 – Way forward

8.1. CFA-EPOXY COMPOSITE ANCHORING MECHANISM

The proposed Pull-out model developed in this work confirmed the importance of having a high-performance epoxy in terms of mechanical and adhesion properties. However, there are some parameters that should be applied to enable it being used for commercial anchoring systems for flexible risers.

Applying and adjusting the model to more complex EF anchoring geometries, considering capstan effect and transverse load from CFA due to the helicoidally organized tensile armors are examples that could be taken into account. Another variable that might be considered for future works is the potential residual stresses due to epoxy shrinking at the curing step.

And finally, the study and implementation of fatigue and ageing fatigue to the Pull-out model is also very important to characterize the CFA anchoring system.

8.2. MWCNT TOUGHENED EPOXY

Toughening epoxy with CNTs has demonstrated a promising solution for improving mechanical properties of CFA anchoring system, but with many challenges. It is evident the need of performing exhaustive researches with many linked parameters.

Improvement of CNT dispersion, for instance, is a very important matter that could be meticulously investigated. Combining Nano particles mixing methods, developing a new one or varying their set ups are some examples that could be assessed.

Other studies like testing different epoxies with different CNTs, other options of functionalization or even developing toughened epoxies with hybrid fillers such as SiC-MWCNTs, as presented in section 2.2.4.3, may help reaching greater improvements to CFA anchoring. Nevertheless, viscosity remains a parameter that shall not be neglected.

From the riser application point of view, considering the severe conditions of the annulus fluid in contact with the anchoring system, the ageing is also a concerning topic. Therefore, comparative exposure tests could be performed with a neat and CNT toughened epoxy to evaluate which one guarantees better chemical stability.

8.3. STRUCTURE HEALTH MONITORING (SHM)

The CFA-Epoxy anchoring system toughened with MWCNTs can provide other benefits than mechanical improvement. Another field of study that may be encouraged to research is SHM since this is an important subject sought by flexible riser suppliers and clients.

As presented in section 2.2.4.3, introducing MWCNTs to epoxy matrix can increase electrical conductivity, making it a semi-conductor. And, depending on CNT type, the percolation can be reached with small amounts of the Nano particle [104], similar to concentrations studied in this work.

RAGHAVAN *et al.* [105] already proved the feasibility of having a SHM in a CNT toughened material by using its electrical conductivity. In the case of anchoring system, it could monitor the adhesion integrity between CFA and epoxy and eventual matrix crack propagation.

References

[1] S. Mazumdar, "What Will Drive Composites Growth in 2015?," Composites Manufacturing, 2015.

[2] A. Lambert, A.-T. Do, A. Felix-Henry and F. Grosjean, "Qualification of Unbonded Dynamic Flexible Riser With Carbon Fibre Composite Armors," in *OMAE2012-83130*, 2012.

[3] M. F. Ashby, Materials Selection in Mechanical Design, 4a Edição ed., Oxford, UK: Elsevier, 2011.

[4] API - American Petroleum Institute, "Specification for Unbonded Flexible Pipe," 2009.

[5] A. L. Anh-Tuan Do, "Qualification of Unbonded Dynamic Flexible Riser with Carbon Fibre Composite Armours," in *Offshore Technology Conference*, Houston, Texas, USA, 2012.

[6] G. B. A. T. D. Didier Hanonge, "Carbon Fiber Armors Applied to Presalt Flexible Pipe Developments," in *Offshore Technology Conference*, Houston, Texas, USA, 2013.

[7] A. F. B. Bueno, "Avaliação das armaduras de tração de riser flexível durante ensaios axiais de tração e fadiga," Porto Alegre, 2010.

[8] Genesis Oil and Gas, [Online]. Available: www.genesisoilandgas.com. [Accessed 7 August 2015].

[9] G. C. Campello, "Metodologia de projeto para o sistema de ancoragem de conectores de dutos flexíveis e proposição de nova tecnologia," Rio de Janeiro, 2014.

[10] DNV - Det Norske Veritas , "Submarine Pipeline Systems," 2012.

[11] Offshore Energy Today, "Free seminar on flexible risers in Norway - Offshore energy today," [Online]. Available: http://www.offshoreenergytoday.com/free-seminar-on-flexible-risers-in-norway/. [Accessed 7 August 2015].

[12] X. Li, J. Wan, X. Du and H. Xiao, "Structure analysis of flexible pipe end fitting seal system," in *OMAE2015-41718*, 2015.

[13] D. FRASER, "Flexible Steel Pipe Applications," in *Fourth International Conference On Composite Materials For Offshore Operations*, Houston, USA, 2005.

[14] API - American Petroleum Institute, "Recommended Practice for Flexible Pipe," 2014.

[15] API - American Petroleum Institute , "Specification for Flexible Pipe Ancillary Equipment," 2013.

[16] K. Stuckey, "Powering the invasion," *Professional engineering,* vol. 27, pp. 72-74, 2014.

[17] [Online]. Available: http://www.offshorerisertechnology.com/overview.html. [Accessed 15 12 2015].

[18] Technip Group, "Flexible Pipes," 2015. [Online]. Available: http://www.technip.com/sites/default/files/technip/fields/publications/attachments/flexible_pipe_july_2015_web.pdf. [Accessed 15 12 2015].

[19] DNV - Det Norske Veritas, "Composite Components," 2013.

[20] A. Salimi, L. Yu, N. Nemati-Raad and M. D. Kalman, "A combined numerical and experimental approach to verify composite tensile armor bend back method during pipe termination," in *OMAE2015-41984*, 2015.

[21] A. K. KULSHRESHTHA and C. VASILE, Handbook of Polymer Blends and Composites, vol. 2, Shawbury, UK: Rapra Technology, 2002.

[22] G. C. Campello and M. C. De Almeida, "End fitting for a flexible riser and method of assembly". Patent US20120211975 A1, 23 August 2012.

[23] E. BUON and H. BERTON, "End-Fitting for Flexible Pipe". Patent US 6,923,477 B2, 2005.

[24] J. BELCHER, "High Temperature End-Fitting". Patent US 6,592,153 B1, 2003.

[25] R. F. Gibson, Principles of Composite Material Mechanics, Detroit, Michigan: McGraw-Hill, 1994.

[26] R. M. Jones, Mechanics of Composite Materials, 2nd ed., Blacksburg, Virginia: Taylor & Francis, Inc., 1998.

[27] A. Kelly, "Composites for 1990s," Philosophical Transactions of the Royal Society of London, 1987, pp. 409-423.

[28] D. HULL, An Introduction to Composite Materials, Cambridge, UK: Press Sindicate of the University of Cambridge, 1995.

[29] L. SPERLING, Introduction to Physical Polymer Science, 4th ed., Pennsylvania, USA: Wiley-Interscience, 2006.

[30] C. S. S. T. E. M. S. E. A. Raju Thomas, Micro- and Nanostructured Epoxy/Rubber Blends, Wiley-VCH Verlag GmbH & Co. KGaA., 2014.

[31] M. Mandhakini, A. Chandramohan, K. Jayanthi and M. Alagar, "Carbon black reinforced C8 ether linked bismaleimide toughened electrically conducting epoxy nanocomposites," *Elsevier - Materials and Design,* vol. 64, pp. 706-713, 2014.

[32] Z. SUN, S. SHI, X. HU, X. GUO, J. CHEN and H. CHEN, "Short-aramid-fiber toughening of epoxy adhesive joint between carbon fiber composites and metal substrates with different surface morphology," *Composites Part B,* no. 77, pp. 38-45, 2015.

[33] A. M. Schrand and T. B. Tolle, "Carbon nanotube and epoxy composites for military applications," in *Carbon Nanotechnology*, L. Dai, Ed., Dayton, USA, Liming Dai, 2006, pp. 633-675.

[34] D. DILLARD and A. POCIUS, Adhesion Science and Engineering - The mechanics of adhesion, vol. 1, Elsevier, 2002.

[35] T. d. C. SILVA, "Determinação do fator momento limite em juntas coladas simples usando método óptico," Universidade Federal Fluminense - UFF, Niterói-RJ, 2015.

[36] Y. YUAN and T. R. LEE, "Contact Angle and Wetting Properties," *Surface Science Techniques,* vol. 51, pp. 3-34, 2013.

[37] A. BAKER, L. ROSE and R. JONES, Advances in bonded composite repair of metallic aircraft structure, vol. 1, Elsevier, 2002.

[38] L. T. DRZAL and P. J. HERRERA-FRANCO, "Measurement methods for fiber-matrix adhesion in composite materials," in *Adhesion Science and Engineering*, vol. 1, Yucatán, México, Elsevier, 2002, pp. 616-660.

[39] H. COX, "The Elasticity and Strength of Paper and Other Fibrous Materials," *British Journal of Applied Physics,* vol. 3, pp. 72-79, 1952.

[40] R. KHRISTENSEN and F. WAALS, "Effective Stiffness of Randomly Oriented Fibre Composites," *Journal of Composite Materials,* vol. 6, pp. 518-532, 1972.

[41] P. R. THAKRE, "Processing and characterization of carbon nanotubes reinforced epoxy resin based based multi-functional composites," 2009.

[42] C. RIEW, "Rubber Chem.," *Technol.,* vol. 2, no. 54, 1981.

[43] L. L. Sobrinho, V. M. Calado and F. L. Bastian, "Effects of rubber addition to an epoxy resin and its fiber glass-reinforced composite," *Polymer composites,* 2012.

[44] K. HSIEH and J. HAN, "Graft Interpretating Polymer of Polyurethane and Epoxy.II. Tougnhening Mechanism," *Journal of Polymer Science Part B: Polymer Physics,* vol. 28, no. 6, March 2003.

[45] J. A. JOHNSTON, "Adhesivesmag - Tougnhening epoxy adhesives," 2013. [Online]. Available: http://www.adhesivesmag.com/articles/92072-toughening-epoxy-adhesives. [Accessed 17 January 2016].

[46] D. F. Saldanha, C. Canto, L. F. da Silva, R. J. Carbas and F. J. Chaves, "Mechanical characterization of a high elongation and high toughness epoxy adhesive," *Elsevier - International Journal of Adhesion & Adhesives ,* vol. 47, pp. 91-98, 2013.

[47] S. RAMA and S. RAI, "Mechanical and Fractrographic Studies on Fly ash-filled Hydroxyl-terminated Polyurethane-toughened Epoxy Composites," *Journal of Composite Materials,* vol. 43, no. 26, pp. 3231-3238, December 2009.

[48] M. YASAEE, I. BOND, R. TRASK and E. GREENHALGH, "Mode I interfacial toughening through discontinuous interleaves for damage suppression and control," *Composites Part A,* vol. 43, pp. 198-207, 2012.

[49] T. Kishore and R. KIRAN, "Impact response in glass-epoxy system with and without perforated PTFE-bearing material at the mid-thickness," *Composite interfaces,* vol. 13, no. 7, pp. 633-646, 2006.

[50] M. S. Sohn and X. Z. Hu, "Mode II delamination toughness of carbon-fibre/epoxy composites with chopped kevlar fibre reinforcement," *Elsevier,* vol. 52, pp. 439-448, 1994.

[51] S. SHI, Z. SUN, X. HU and H. CHEN, "Carbon-fiber and aluminum-honeycomb sandwich composites with and without Kevlar-fiber interfacial toughening," *Composite Part A ,* vol. 67, pp. 102-110, 2014.

[52] N. E. ZANDER, "Epoxy Nano-Reinforced Composite Systems," Phoenix, USA, 2008.

[53] A. N. S. Alamry, B. G. Prusty, M. R. Mada and S. Bandyopadhyay, "Improved crack resistance and fracture toughness using MWCNT modified epoxy for delaminated composite structures," *Elsevier - Procedia Materials Science,* vol. 3, pp. 805-810, 2014.

[54] D. LI, X. ZHANG, G. SUI, D. WU and J. LIANG, "Toughness improvement of epoxy by incorporating carbon nanotubes into the resin," *Journal of Materials Science Letters,* vol. 22, no. 11, pp. 791-793, 2003.

[55] G. Y. Byrne M.T., "Recent advances in research on carbon nanotube-polymer composites," *Advanced Materials,* vol. 22, no. 15, pp. 1672-1688, 2010.

[56] C. W. T. M. Ashraful Alama, "Surface amination of carbon nanoparticles for modification ofepoxy resins: plasma-treatment vs. wet-chemistry approach," *European Polymer Journal,* vol. 87, pp. 422-448, 2017.

[57] H. X. W. Y. Lifei Chen, "Functionalization Methods of Carbon Nanotubes and its Applications," Intech, Shanghai, China, 2011.

[58] C. KINGSTON, R. ZEPP, A. ANDRADY, D. BOVERHOF, R. FEHIR, D. HAWKINS, J. ROBERTS, P. SAYRE, B. SHELTON, Y. SULTAN, V. VEJINS and W. WOHLLEBEN, "Release characteristics of selected carbon nanotube polymer composites," *Carbon,* no. 68, pp. 33-57, 2014.

[59] G. H. J. J. K. P. J. C. K. H. J. R. S. H. H. Jaemin Chaa, "Improvement of modulus, strength and fracture toughness of CNT/Epoxy nanocomposites through the functionalization of carbonnanotubes," *Composites Part B,* vol. 129, pp. 169-179, 2017.

[60] M. Zamanian, M. Mortezaei, B. Salehnia and J. E. Jam, "Fracture toughness of epoxy polymer modified with nanosilica particles: Particle size effect," *Elsevier - Engineering Fracture Mechanics,* vol. 97, pp. 193-206, 2013.

[61] X. JIA, G. LI, B. LIU, Y. LUO, G. YANG and X. YANG, "Multiscale reinforcement and interfacial strengthening on epoxy-based composites by silica nanoparticle-multiwalled carbon nanotube complex," *Composites: Part A,* no. 48, pp. 101-109, 2013.

[62] B. HARRIS, Engineering Composite Materials, London: The Institute of Materials, 1999.

[63] J. DAVIS, "ARALL — from development to a commercial material," *Progress in Advanced Materials and Processing,* pp. 41-49, 1985.

[64] D. A. HOPKINS and C. C. CHAMIS, "A Unique Set of Micromechanics Equations for High Temperature Metal Matrix Composites," *Testing Technology of Metal Matrix Composites ,* vol. 964, pp. 159-176, 1988.

[65] A. KELLY and W. TYSON, "Tensile Properties of Fiber Reinforced Metals: Copper/Tungsten and Copper/Molybdenum," *Journal of the Mechanical and Physics of Solids,* vol. 13, pp. 329-350, 1965.

[66] C. SMITH, "Some New Types of Orthotropic Plates Laminated of Orthotropic Material," *Journal of Applied Mechanics,* vol. 20, pp. 286-288, 1953.

[67] K. PISTER and S. DONG, "Elastic Bending of Layered Plates," *Journal of Engineering Mechanics Division,* vol. 85, pp. 1-10, 1959.

[68] J. WHITNEY, Structural Analysis of Laminated Plates, Lancaster, PA: Technomic Publishing Co, 1987.

[69] C. S. Rao, "Analysis of tapered laminated composite tubes under tension," The University of Texas at Arlington, Arlington, Texas, USA, 2007.

[70] S. W. Tsai, "Strength & Life of Composites," Aero & Astro, Stanford U, San Francisco, California, USA, 2008.

[71] A. SHUKLA, Practical Fracture Mechanics in Design, 2nd ed., Kingston, USA: Marcel Dekker, 2005.

[72] J. IPIÑA, Mecánica de Fractura, Librería y Editorial Alsina, 2004.

[73] M. JANSSEN, J. ZUIDEMA and R. J. H. WANHILL, Fracture Mechanics, 2nd ed., Spon Press - Taylor & Francis Group, 2002.

[74] G. IRWIN, "Fracture Dynamics," in *Fracturing of Metals*, Cleveland, American Society of Metals, 1948.

[75] E. OROWAN, "Fracture strength of solids," in *Report on Progress in Physics*, vol. 12, London, Physical Society of London, 1949.

[76] T. R. STROHAECKER, "Mecânica da Fratura," Porto Alegre.

[77] P. CHUA and M. PIGGOTT, "The glass fibre-polymer interface. I. Theoretical considerations for single fibre pull-out tests," *Composite Science Technology,* vol. 22, pp. 33-42, 1985.

[78] K. KATHIRESAN, "Three-Dimensional Linear Elastic Fracture Mechanics by a Displacement Hybrid Finite Element Model," 1976.

[79] M. WESTIN and R. RIBEIRO, "Método dos elementos finitos na simulação de tensão e elasticidade em placas," Belo Horizonte.

[80] R. KREGTING, "Cohesive zone models towards a robust implementation of irreversible behaviour," 2005.

[81] H. KHORAMISHAD, M. HAMZENEJAD and R. ASHOFTEH, "Characterizing cohesive zone model using a mized-mode direct method," *Engineering Fracture Mechanics,* vol. 153, pp. 175-189, 2016.

[82] E. RYBICKI and K. M.F., "A finite element calculation of stress intensity factors by a modified crack closure integral," *Fracture Mechanics,* vol. 9, p. 931–938, 1977.

[83] R. KRUEGER, "Virtual crack closure technique: History, approach, and applications," *Applied Mechanics Review,* vol. 57, no. 2, pp. 109-143, 2004.

[84] I. RAJU, "Calculation of strain-energy release rates with higher order and singular finite elements," *Engineering Fracture Mechanics,* vol. 28, p. 251–274, 1987.

[85] R. BARSOUM, "On the use of isoparametric finite elements in linear fracture mechanics," *Int. J. Numer. Methods Eng.,* vol. 10, p. 25–37, 1976.

[86] J. K. Wells and P. W. R. Beaumont, Debonding and pull-out processes in fibrous composites, Cambridge, 1984.

[87] R. Borrelli, F. Caputo, A. Riccio, F. Scaramuzzino and A. Sellitto, "Cohesive Zone Material Model in ANSYS: a Sensitivity Analysis on a DCB Test Cast," in *EnginSoft International Conference - CAE Technologies for Industry*, Verona, 2011.

[88] N. Dronamraju, J. Solass and J. Hildebrand, "Studies of fiber-matrix debonding," *Frontiers of Structural and Civil Engineering,* vol. 9(4), p. 448–456, 2015.

[89] N. SAKAKIBARA, "Finite Element Method in Fracture Mechanics," Austin, USA, 2008.

[90] F. V. ANTUNES, N. RILO, J. M. FERREIRA and C. M. BRANCO, "Análise linear elástica por elementos finitos 3D de um corpo com fenda," *Revista Internacional de Métodos Numéricos para Cálculo y Diseño en Ingeniería,* vol. 17, no. 3, pp. 317-333, 2001.

[91] ASTM - American Society for Testing and Materials, "Standard Test Method for Tensile Properties of Plastics".

[92] ASTM - American Society for Testing and Materials, "Standard Test Method for Compressive Properties of Rigid Plastics".

[93] I. -. I. O. f. Standardization, "ISO 13586 - Plastics - Determination of fracture toughness (GIC and KIC) - Linear elastic fracture mechanics (LEFM) approach," 2000.

[94] ASTM - American Society for Testing and Materials, "Standard Test Method for Linear-Elastic Plane-Strain Fracture Toughness KIc of Metallic Materials".

[95] ASTM - American Society for Testing and Materials, "ASTM D5868 - Standard Test Method for Lap Shear Adhesion for Fiber Reinforced Plastic (FRP) Bonding," 2014.

[96] ASTM - American Society for Testing and Materials, "D6671/D6671M - Standard Test Method for Mixed Mode I-Mode II Interlaminar Fracture Toughness of Unidirectional Fiber Reinforced Polymer Matrix Composites," 2013.

[97] A. Costache, "Anchoring FRP Composite Armor in Flexible Offshore Riser Systems," Technical University of Denmark, Kgs. Lyngby, Denmark, 2015.

[98] M. R. Piggot, “Debonding and friction at Fibre-Polymer Interfaces. I: Criteria for failure and sliding,” *Composite Science and Technology,* vol. 30, pp. 295-306, July 1987.

[99] Y. Y. Jia, W. Yan and H.-Y. Liu, "Numerical study on carbon fibre pullout using a cohesive zone model," in *18th International Conference on Composite Materials*, Sydney, Australia, 2011.

[100] M. R. Piggot, Load Bearing Fibre Composites, Ontario, Canada, 2016.

[101] C. C. O. C. X. EL-MAZRY, "A new kinetic model for predicting polyamide 6-6 hydrolysis and its mechanical embrittlement," *Polymer Degradation and Stability, Elsevier,* vol. 97, pp. 1049-1059, 2012.

[102] M. d. SALINAS-RUIZ, A. A. SKORDOS and I. K. PARTRIDGE, "Rubber toughened epoxy loaded with carbon nanotubes: structure – property relationships," *Journal of Materials Science,* vol. 45, no. 10, pp. 2633-2639, May 2010.

[103] A. ALLAOUI and N. EL BOUNIA, "How carbon nanotubes affect the cure kinetics and glass transition temperature of their epoxy composites? – A review," *eXPRESS Polymer Letters,* vol. 3, no. 9, p. 588–594, 2009.

[104] G. V. V. S. L. D. P. DEROMBISEA, "Degradation of Technora aramid fibres in alkaline and neutral environments," *Polymer Degradation and Stability,* vol. 94, no. 10, pp. 1615-1620, 2009.

[105] A. -. A. S. f. T. a. Materials, "Standard Test Method for Strength Properties of Adhesives in Shear by Tension Loading of Single-Lap-Joint Laminated Assemblies," 2014.

[106] E. F. A. Ch. Laurent, "The weigth and density of carbon nanotubes versus the number of walls and diameter," *Carbon,* vol. 48, no. 10, pp. 2994-2996, 2010.

[107] X. X. P. M. S. E. K. C. B. N. M. Y. Z. Xiaomei Zeng, "Characteristics of the electrical percolation in carbon nanotubes/polymer nanocomposites," Singapore, 2011.

[108] S. S. K. C. T. D. D. B. S. W. B. L. W. Ajay Raghavan, "Structural Health Monitoring using Carbon Nanotube (CNT) Enhanced Composites," Massachusetts Institute of Technology, Metis Design Corporation, Cambridge, 2009.

[109] H. Zhou and S. Xu, "A new method to prepare rubber toughened epoxy with high modulus and high impact strength," *Elsevier - Materials Letters,* vol. 121, pp. 238-240, 2014.

[110] L. Zhai, G. Ling, J. Li and Y. Wang, "The effect of nanoparticles on the adhesion of epoxy adhesive," *Elsevier - Materials Letters,* vol. 60, pp. 3031-3033, 2006.

[111] F. N. Tüzün and M. S. Tunalioglu, "The effect of finely-divided fillers on the adhesion strengths of epoxy-based adhesives," *Elsevier - Composite Structures,* vol. 121, pp. 296-303, 2015.

[112] R. Thomas, D. Yumei, H. Yuelong, Y. Le, P. Moldenaers, Y. Weimin, T. Czigany and S. Thomas, "Miscibility, morphology, thermal, and mechanical properties of a DGEBA based epoxy resin toughened with a liquid rubber," *Elsevier - Polymer ,* vol. 49, pp. 278-294, 2008.

[113] A. Salehi-Khojin, J. J. Stone and W.-H. Zhong, "Improvement of interfacial adhesion between UHMWPE fiber and epoxy matrix using functionalized graphitic nanofibers," *Journal of Composite Materials,* vol. 41, no. 10, 2007.

[114] W. Liu, J. Kong, W. E. Toh, R. Zhou, G. Ding, S. Huang, Y. Dong and X. Lu, "Toughening of epoxies by covalent anchoring triazole-functionalized stacked-cup carbon nanofibers," *Elsevier - Composites Science and Technology,* vol. 85, pp. 1-9, 2013.

[115] Q.-H. Le, H.-C. Kuan, J.-B. Dai, I. Zaman, L. Luong and J. Ma, "Structure-property relations of 55nm particle-toughened epoxy," *Elsevier - Polymer ,* vol. 51, pp. 4867-4879, 2010.

[116] V. Joudon, G. Portemont, F. Lauro and B. Bennani, "Experimental procedure to characterize the mode I dynamic fracture toughness of advanced epoxy resins," *Elsevier - Engineering Fracture Mechanics,* vol. 126, pp. 166-177, 2014.

[117] M. Fan, J. Liu, X. Li, J. Cheng and J. Zhang, "Curing behaviours and properties of an extrinsic toughened epoxy/anhydride system and an intrinsic toughened epoxy/ahnydride system," *Elsevier - Thermochimica Acta,* vol. 554, pp. 39-47, 2013.

[118] M. A. Boyle, C. J. Martin and J. D. Neuner, "Epoxy Resins".

[119] ASTM - American Society for Testing and Materials, "Standard Test Method for Strength Properties of Double Lap Shear Adhesive Joints by Tension Loading," 1996.

[120] D. ROYLANCE, "Introduction to Composite Materials," Massachusetts, USA, 2000.

[121] A. JONES, C. WATKINS, S. WHITE and N. SOTTOS, "Self-healing thermoplastic-toughened epoxy," *Polymer,* no. 74, pp. 254-261, July 2015.

[122] G. MANSOUR and D. TZETZIS, "Nanomechanical Characterization of Hybrid Multiwall Carbon Nanotube and Fumed Silica Epoxy Nanocomposites," *Polymer-Plastics Technology and Engineering,* no. 52, p. 1054–1062, 2013.

[123] Technip, "Petrobras awards Technip two contracts for ultra-deep water fields," 2014. [Online]. Available: http://www.typepad.com/services/trackback/6a00d8341c4fbe53ef019b045b1140970d. [Accessed Agosto 2015].

[124] M. ZAMANIAN, M. MORTEZAEI, B. SALEHNIA and J. JAM, "Fracture toughness of epoxy polymer modified with nanosilica particles: Particle size effect," *Engineering Fracture Mechanics,* vol. 97, pp. 193-206, 2013.

[125] S. WANG, "Delamination Crack Growth in Unidirectional Fiber-Reinforced Composite under Static and Cyclic Loading," in *Composite Materials: Testing and Design*, vol. 674, Philadelphia, USA, American Society for Testing and Materials, 1979, pp. 642-663.

[126] T. O'BRIEN, "Characterization of Delamination Onset and Growth in a Composite Laminate," in *Damage in Composite Materials*, vol. 775, Philadelphia, USA, American Society for Testing and Materials, 1982, pp. 140-167.

[127] H. S. TEIJIN - Human Chemistry, "Twaron – a unique combination of properties," [Online]. Available: http://www.teijinaramid.com/wp-content/uploads/2011/09/Properties-of-Twaron-leaflet.pdf. [Accessed 12 2015].

[128] R. P. MATTEDI, A.-T. DO, F. L. BASTIAN and D. B. J. HE, "Study of MWCNTs filled toughened epoxy for anchoring composite tensile armours inside the End fitting of Flexible riser," in *21st International Conference on Composite Materials*, Xi'an, China, 2017.

Annex 1 – Epoxy samples

Tensile samples: Neat epoxy.

Tensile samples: MWCNTs toughened epoxy.

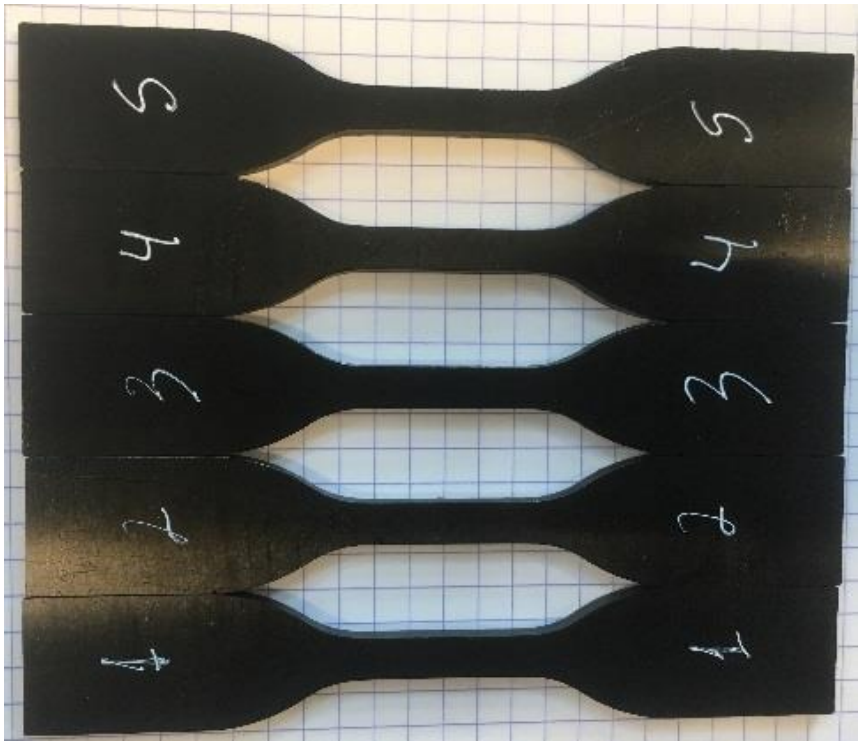

Compressive samples: Neat epoxy.

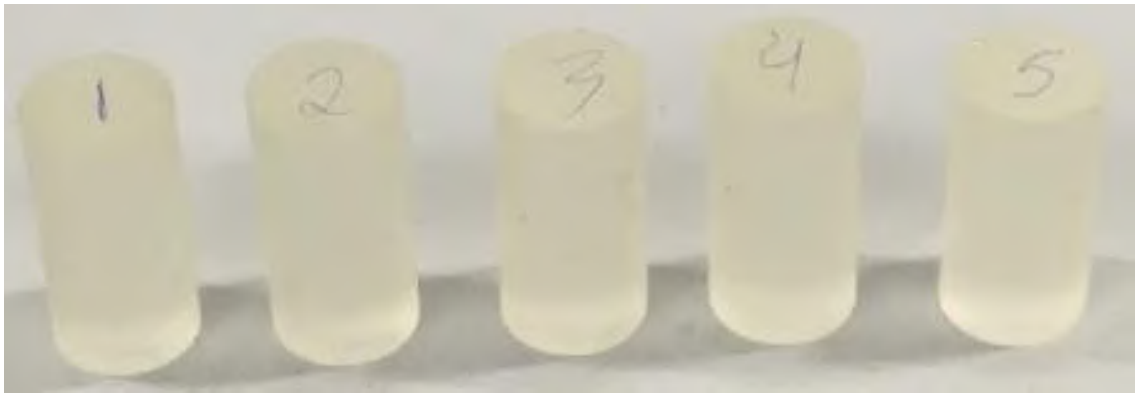

Compressive samples: MWCNTs toughened epoxy.

K_{1c} samples: Neat epoxy.

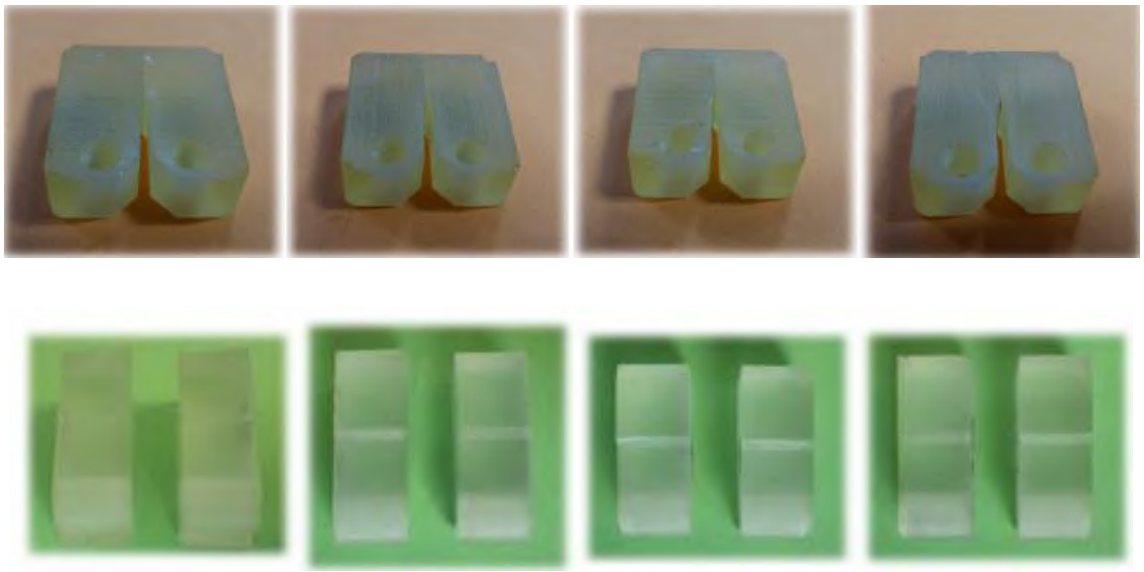

K_{1c} samples: MWCNTs toughened epoxy.

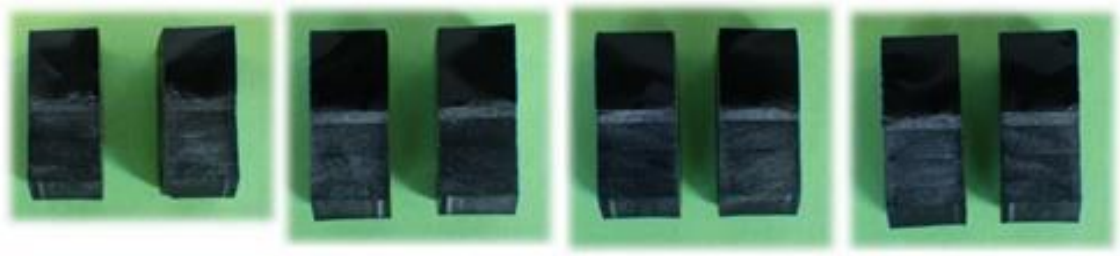

Annex 2 – CFA-epoxy samples

Lap shear samples:

Double cantilever beam samples: Neat epoxy.

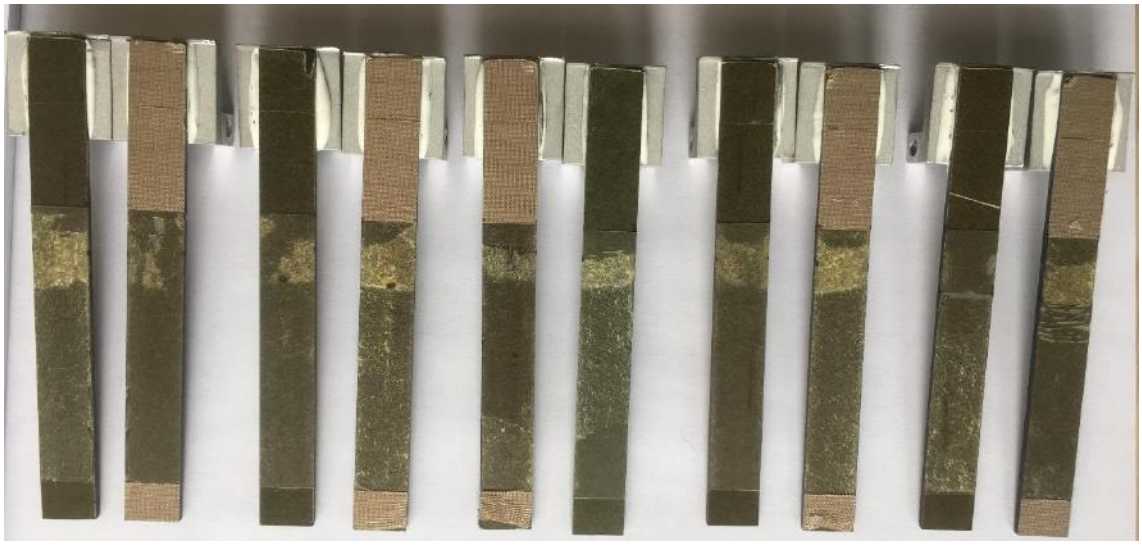

Double cantilever beam samples: MWCNTs toughened epoxy.

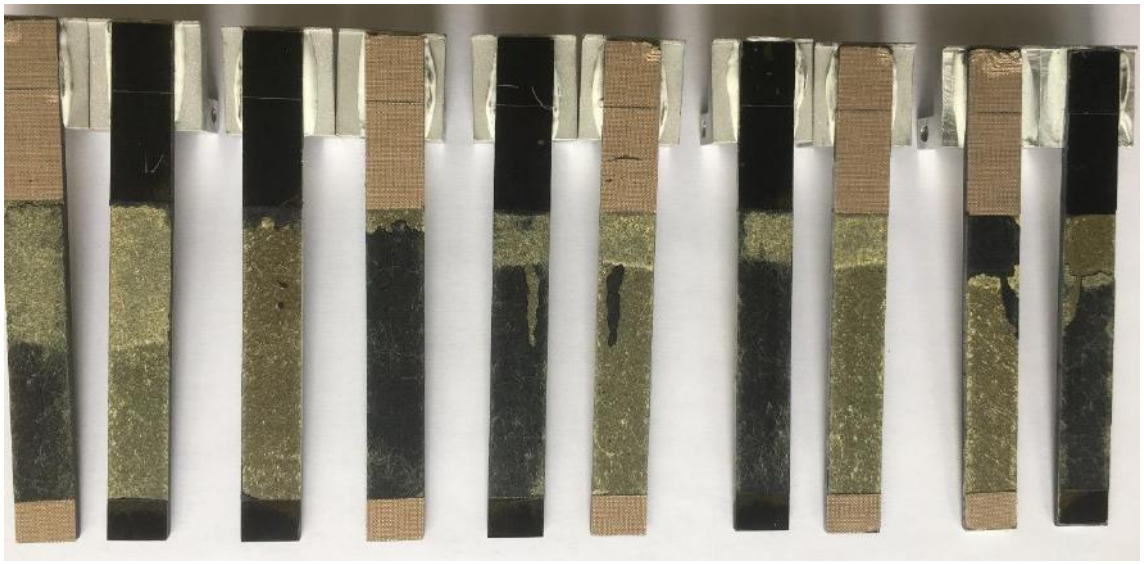

Annex 3 – FEM results sheet

FEM sheet of CFA pull-out force Fd (Force reaction maximum) vs debonding energy G_c for anchoring length $L = 20mm$ epoxy total thickness $t_E = 5.2mm$ ($Epoxy\_thick = 1.5mm$).

Name	P5 - XYPlane.Epoxy_thick	P6 - XYPlane.L	P7 - XYPlane.CFA_thick	P8 - XYPlane.L_CFA	P16 - Maximum Equivalent Tangential Contact Stress	P17 - Critical Fracture Energy for Tangential Slip	P18 - Artificial Damping Coefficient	P19 - Critical Mode II Energy-Release Rate	P15 - Force Reaction Maximum Y Axis
Units	mm	mm	mm	mm	MPa	J m^-2	s	J m^-2	N
DP 0 (Current)	1.5	20	1.1	40	50.27	80	0.005	80	7236.075
DP 1	1.5	20	1.1	40	43.54	60	0.005	60	6241.702
DP 2	1.5	20	1.1	40	35.55	40	0.005	40	4818.337
DP 3	1.5	20	1.1	40	25.14	20	0.005	20	3489.372
DP 9	1.5	20	1.1	40	22.2	15.6	0.005	15.6	3118.693
DP 10	1.5	20	1.1	40	17.775	10	0.005	10	2372.043
DP 11	1.5	20	1.1	40	12.565	5	0.005	5	1799.072
DP 12	1.5	20	1.1	40	7.95	2	0.005	2	1131.563
DP 13	1.5	20	1.1	40	5.62059	1	0.005	1	841.7269
DP 23	1.5	20	1.1	40	50.27	80	0.01	80	7375.912
DP 24	1.5	20	1.1	40	43.54	60	0.01	60	5985.222
DP 25	1.5	20	1.1	40	35.55	40	0.01	40	5236.113
DP 26	1.5	20	1.1	40	25.14	20	0.01	20	3747.587

DP 27	1.5	20	1.1	40	22.2	15.6	0.01	15.6	3163.568
DP 28	1.5	20	1.1	40	17.775	10	0.01	10	2716.94
DP 29	1.5	20	1.1	40	12.565	5	0.01	5	1915.316
DP 30	1.5	20	1.1	40	7.95	2	0.01	2	1198.877
DP 31	1.5	20	1.1	40	5.62059	1	0.01	1	916.7339
DP 43	1.5	20	1.1	40	53.325	90	0.005	90	7716.477
DP 44	1.5	20	1.1	40	58.95	110	0.005	110	7798.153
DP 45	1.5	20	1.1	40	53.325	90	0.01	90	7143.615
DP 46	1.5	20	1.1	40	58.95	110	0.01	110	8408.118

FEM sheet of CFA pull-out force Fd (Force reaction maximum) vs epoxy tensile modulus E_E for anchoring length $L = 20mm$ epoxy total thickness $t_E = 5.2mm$ ($Epoxy\_thick = 1.5mm$).

Name	P5 - XYPlane.Epoxy_thick	P6 - XYPlane.L	P7 - XYPlane.CFA_thick	P8 - XYPlane.L_CFA	P18 - Artificial Damping Coefficient	P19 - Tensile_Modulus	P20 - Maximum Equivalent Tangential Contact Stress	P15 - Force Reaction Maximum Y Axis
Units	mm	mm	mm	mm	s	MPa	MPa	N
DP 0 (Current)	1.5	20	1.1	40	0.005	2000	5.2	1206.683
DP 1	1.5	20	1.1	40	0.005	3000	6.63	1426.989
DP 2	1.5	20	1.1	40	0.005	4000	7.935	1571.925
DP 3	1.5	20	1.1	40	0.005	5000	9.16	1764.702
DP 9	1.5	20	1.1	40	0.005	6000	10.337	1744.572
DP 10	1.5	20	1.1	40	0.005	7000	11.47	1873.955
DP 11	1.5	20	1.1	40	0.005	8000	12.565	1799.072

DP 23	1.5	20	1.1	40	0.01	2000	5.2	1265.013
DP 24	1.5	20	1.1	40	0.01	3000	6.63	1465.192
DP 25	1.5	20	1.1	40	0.01	4000	7.935	1614.96
DP 26	1.5	20	1.1	40	0.01	5000	9.16	1756.113
DP 27	1.5	20	1.1	40	0.01	6000	10.337	1898.624
DP 28	1.5	20	1.1	40	0.01	7000	11.47	1789.658
DP 29	1.5	20	1.1	40	0.01	8000	12.565	1912.658
DP 35	1.5	20	1.1	40	0.005	500	2.420655	656.0184
DP 36	1.5	20	1.1	40	0.005	1000	3.51151	895.2971
DP 37	1.5	20	1.1	40	0.01	500	2.420655	672.4451
DP 38	1.5	20	1.1	40	0.01	1000	3.51151	912.4505

FEM sheet of CFA pull-out force Fd (Force reaction maximum) vs debonding energy G_c for anchoring length $L = 200mm$ epoxy total thickness $t_E = 75mm$ ($Epoxy\_thick = 33.9mm$).

Name	P5 - XYPlane.Epoxy_thick	P6 - XYPlane.L	P7 - XYPlane.CFA_thick	P8 - XYPlane.L_CFA	P16 - Maximum Equivalent Tangential Contact Stress	P17 - Critical Fracture Energy for Tangential Slip	P18 - Artificial Damping Coefficient	P19 - Critical Mode II Energy-Release Rate	P15 - Force Reaction Maximum Y Axis
Units	mm	mm	mm	mm	MPa	J m^-2	s	J m^-2	N
DP 22	33.9	200	1.1	400	12.758	10	0.005	10	0
DP 23	33.9	200	1.1	400	145.472	1300	0.005	1300	66798.02
DP 24	33.9	200	1.1	400	133.813	1100	0.005	1100	63838.79

DP 25	33.9	200	1.1	400	121.039	900	0.005	900	62767.56
DP 26	33.9	200	1.1	400	106.747	700	0.005	700	56149.1
DP 27	33.9	200	1.1	400	90.217	500	0.005	500	0
DP 28	33.9	200	1.1	400	63.793	250	0.005	250	0
DP 29	33.9	200	1.1	400	40.346	100	0.005	100	0
DP 30	33.9	200	1.1	400	28.527	50	0.005	50	0